DYNAMICS OF TURBULENT PREMIXED FLAMES IN ACOUSTIC FIELDS

A Dissertation
Presented to
The Academic Faculty

By

Santosh Hemchandra

In Partial Fulfillment
of the Requirements for the Degree
Doctor of Philosophy in
Aerospace Engineering

Georgia Institute of Technology

August 2009

DYNAMICS OF TURBULENT PREMIXED FLAMES IN ACOUSTIC FIELDS

Approved by:

Dr. Tim Lieuwen, Advisor
Associate Professor
School of Aerospace Engineering
Georgia Institute of Technology

Dr. Ben T. Zinn
Regents Professor, David S. Lewis Chair
School of Aerospace Engineering
Georgia Institute of Technology

Dr. Suresh Menon
Professor
School of Aerospace Engineering
Georgia Institute of Technology

Dr. Vigor Yang
Professor, Department Chairman,
School of Aerospace Engineering
Georgia Institute of Technology

Dr. Norbert Peters
Professor, Head of department
Institut für Technische Verbrennung
RWTH Aachen University, Aachen
Germany

To the giants on whose shoulders we stand

Acknowledgements

I would like to first and foremost acknowledge with extreme gratitude, the consideration, mentoring and guidance of my advisor Dr. Tim Lieuwen in many ways, academic and otherwise in helping me perform the present work. The guidance and mentoring of Dr. R.I. Sujith who nurtured a disciplined approach towards research during my undergraduate years at IIT Madras are gratefully acknowledged. I thank Dr. P. Sriram and Dr. S. R. Chakravarthy at IIT madras for their motivative support and guidance to do aerospace engineering. The support and intellectually stimulating discussions with Drs. Bala Varatharajan, Venkat Tangirala, Florian Pintgen and others at GE GRC over the course of an internship are gratefully acknowledged. The invaluable mentorship and intellectual stimulation from discussions with Drs. Preetham, Santosh Shanbhogue, Mohan Bobba, Venkata Nori and Satish Undapalli throughout the course of my tenure at Georgia tech. are gratefully acknowledged. I thank Dr. Rajesh Rajaram for the many discussions on many topics (over Starbucks coffee) that have directly and indirectly influenced the present work. I thank Shreekrishna and Donghyuk Shin for their useful criticism and proof reading of portions of this work. The encouragement and patience with my idiosyncrasies of Yash, Arun, Sai, Nischint, Nandita, Neelakantan, Jackie, Susheel, Prabakar, Chiluwata and Andrew and other members of the combustion lab who are too numerous to be mentioned here are gratefully acknowledged. The patience and affection that I have received from Priyanka (my wife), Aparna (my sister), Satish Mohan and Rashmi (my uncle and aunt) at every stage of the work cannot be adequately thanked. Finally, none of this work was possible without the blessings and support of my parents and parents-in-law. This work is in many ways a product of their efforts as well.

Contents

ACKNOWLEDGEMENTS ..... **I**

LIST OF FIGURES ..... **V**

NOMENCLATURE ..... **VIII**

SUMMARY ..... **X**

CHAPTER 1 INTRODUCTION **1**

1.1 Turbulent Combustion 2

1.2 Combustion instability – flame response modeling 10

CHAPTER 2 FLAME FRONT TRACKING – G-EQUATION **19**

2.1 G-equation Formulation 20

CHAPTER 3 NUMERICAL FORMULATION **24**

3.1 Theoretical considerations 27

3.2 Numerical Formulation 32

3.3 Local Level-set method 38

3.4 Velocity field model 40

CHAPTER 4 FLAME SURFACE KINEMATICS – ANALYTICAL FORMULATION **46**

4.1 Theoretical Formulation 47

4.2 Slope correlations 52

4.3 Local Consumption speed 55

CHAPTER 5 FLAME SURFACE KINEMATICS - RESULTS 66

5.1 Correlation analysis 70

5.2 Local consumption speed 78

5.3 Implications for modeling 81

CHAPTER 6 FORCED FLAME RESPONSE – THEORETICAL FORMULATION 89

6.1 Theoretical formulation 90

6.2 Flame response modeling 100

CHAPTER 7 FORCED FLAME RESPONSE - RESULTS 109

7.1 Flame response characteristics 109

7.2 Response modeling 120

CHAPTER 8 CONCLUSION AND RECOMMENDATIONS 126

8.1 Flame kinematics – unforced flame 126

8.2 Forced response – Heat release transfer function 127

8.3 Recommendations for future work 128

APPENDIX A GRID CONVERGENCE 131

APPENDIX B NON-LOCAL SLOPE CORRELATION FUNCTIONS 134

APPENDIX C UNFORCED FLAME FORMULATION 138

APPENDIX D FORCED FLAME FORMULATION 141

APPENDIX E TURBULENCE CORRECTION – STROUHAL NUMBER DEPENDENCE 154

APPENDIX F TURBULENCE CORRELATION FUNCTIONS 159

REFERENCES 164

List of Figures

Figure 1-1: Schematic representation of turbulent flames: Conical Bunsen flame (left) centerbody stabilized flame (right) 4

Figure 1-2: Schematic of driving and damping processes. 11

Figure 2-1: Instantaneous snapshot of a wrinkled laminar flamelet (schematic) as a boundary between products and reactants. Also shown schematically are the local normal vector to the flame surface and the laminar propagation speed. 20

Figure 3-1: a) Typical signed distance function. Also shows a cut plane at z=0. b) The corresponding zero level-set. 30

Figure 3-2: Schematic of the computational domain showing the location of the flame attachment flame. Also shown are the attachment plane location h_a and lateral extent of the flame r_o 33

Figure 3-3: Typical zero level-set of the initial G field used in the present computations: nominally 2D flame. The mean flow direction is along the z-axis. The black segment in the above shows the segment of the zero level-set that behaves as the flame holder. Flame holding location is a z = 0.06 m. 36

Figure 3-4: Comparison between the longitudinal correlation function of the generated turbulence field (symbols) and the corresponding theoretical targets (solid curves) for three nominal integral length scales. M=201, u'/s_L = 0.75. 43

Figure 4-1: Schematic of investigated geometry – one half bluff-body flame stabilized on a prismatic flame holder. Shown are two – possible co-ordinate systems, burner fixed (x-y-z) and flame-fixed (s-y-n). The y-axis is directed perpendicularly into the page. 47

Figure 4-2: Schematic representation of the turbulent flame showing (a) the reference surface and (b) a schematic representation of the surface patch used to define consumption speed. 55

Figure 5-1: Schematic of investigated geometry. Bluff-body flame stabilized on a prismatic flame holder (one half only shown). Also shown are two possible co-ordinate systems for analysis, burner fixed (x-y-z) and flame-fixed (s-y-n). The y-axis is directed perpendicularly into the page. 67

Figure 5-2: Typical snapshot of the instantaneous flame surface (a) u'/s_L = 0.75, (b) u'/s_L = 2.25 and (c) u'/s_L = 3.75. $\gamma \sim 4^o$. Notice that flame surface winkling increases with increasing distance from the flame-holder resulting in pocket formation. 68

Figure 5-3: Instantaneous snapshots of a vertical section through the flame surface at three successive time instants separated by an interval τ=2.2 (u'/s_L = 3.75. $\gamma \sim 4^o$). The arrows labeled 1 and 2 tracks the evolution of pockets of type 1 and 2 respectively. 69

Figure 5-4: Variation of the non-local slope correlation with spatial separation along the *s*-direction at different time intervals as derived using linear Non-local theory at four different spatial locations s = (a) 5 (b) 10 (c) 15 (d) 50. $\gamma \sim 4^o$). Also shown is the envelope of the maximum correlations at each value of time interval (black curve) for all cases. 71

Figure 5-5: Peak correlation envelopes of the local and non-local slope correlations with the correlation envelope of the velocity fluctuations. Flame angle γ~4^o. 72

Figure 5-6: Local burning area correlation at different values of time interval τ at arbitrary locations on the flame surface as shown below each individual result. Turbulence intensities, (a)-(b) u'/s_L =3.75, (c)-(d) u'/s_L =2.25 and (e)-(f) u'/s_L =0.75. Also shown is the envelope of peak correlation values for each of the cases (a) and (b) where u'/s_L =3.75 (solid curve *sans* symbols).Flame angle, γ~4^o for all cases. 74

Figure 5-7: Envelope of local area fluctuations at different reference points u'/s_L =3.75, flame angle, γ~4^o. Also shown for reference is the velocity correlation envelope. 75

Figure 5-8: Envelope of local area fluctuations at three different turbulence intensities at a distance of a) s=15 and b) s=20 from the flameholder. Flame angle, γ~4^o. Also shown for reference is the velocity correlation envelope. 76

Figure 5-9: Spatial variation of local consumption speed (a) normalized by s_L and (b) normalized by $S_{T,LC}^{Lin}$,at three different turbulence intensities (solid curves) given by the value of u'/s_L . Flame angle, $\gamma \sim 4^o$. Also shown are the corresponding predictions from linear kinematic theory in each case (broken curves). The horizontal blue line in (a) is the prediction from the theory of Aldredge for u'/s_L =0.75. 78

Figure 5-10: Comparison between present computations and the prediction from the local consumption speed model of Lipatnikov and Chomiak (u'/s_L =0.75, γ~4^o). Also shown is the prediction from the linear theory (broken curve) developed in the present work..... 84

Figure 6-1: Schematic of investigated geometry - axis-symmetric bluff-body stabilized flame. 90

Figure 6-2: Instantaneous image of flame contour and vorticity distribution. Flow is from bottom to top. Image courtesy, Shanbhogue et al [58] (reproduced with permission). 91

Figure 6-3: Schematic of the investigated geometry showing the ensemble averaged flame surface. 100

Figure 7-1: Variation of total transfer function magnitude and phase with Strouhal number for typical values of *K*= (a)-(b) 0, (c)-(d) 1.0 and (e)-(f) 3.0. Also shown for reference in each case is the corresponding laminar transfer function. Flame angle γ=45^o. 112

Figure 7-2: Variation of the leading order turbulence correction term with Strouhal number (a) magnitude and (b) phase. Flame angle, $\gamma = 45^o$ and flame length, Λ=1. 115

Figure 7-3: Schematic showing the influence of the wavelength of coherent forcing relative to the turbulent scales on burning area destruction. The solid curves on the left show schematically the resultant wrinkling if there were no kinematic restoration. The broken curves show schematically, the base-line coherent wrinkling. The small arrows show the direction of flame surface propagation. 116

Figure 7-5: Variation of the (a) Magnitude and (b) phase relative to laminar response of the leading order turbulence correction for different flame angles γ, K = 1.0, Λ = 1. 117

Figure 7-4: Variation of leading order turbulence correction magnitude for K = 0. Flame angle, γ=45^o, and flame length, Λ=1. The vertical line shows the characteristic St_2 value beyond which coherent flame wrinkling wavelength becomes comparable to turbulence length scales. 119

Figure 7-6: a) Variation of local consumption and displacement speeds from the non-local model and b) schematic showing the reference area on the unforced mean surface used to define $f_c(r)$, ε_T = 0.05, γ= 45^o and Λ=1. 121

Figure 7-7: Variation of normalized local consumption/displacement speeds from the theory of Lipatnikov and Chomiak. Turbulent mixing time T=50, S_o/s_L =0.13, γ= 45^o and flame length, Λ=1. 123

Figure 7-8: Comparison of transfer function magnitude and phase from the two modeling approaches and the theoretical analysis (a)-(b) K = 0.3, (c)-(d) K = 0.5, (e)-(f) K = 1.5, ε_T =0.05 and γ= 45^o 124

Figure A-1: Variation of ensemble averaged local burning area increase with flame surface location (on the nominal flame surface). Flame angle γ ~ 4^o. The broken curve shows the linear result. 132

Figure A-2: Relative change in $\Delta A_L/A_{L,ref}$ over two successive grid refinements as a percentage of $\Delta A_L/A_{L,ref}$ at Δx=0.05. Note that in the second case, the relative change is less than 10% for a major portion of the flame surface considered. 133

Figure F-1: Schematic of vector system used to evaluate space time correlation functions between points 1 and 2 separated by distance s. Co-ordinate axes for reference only. No assumptions have been made about the underlying co-ordinate system representation of the vectors. 159

Nomenclature

G	Level-set function
s_L	Laminar flame speed
γ	Nominal flame angle with respect to z-axis (both 2D and axis-symmetric cases)
U_o	Mean flow velocity (constant)
$S_{T,LC}$	Local consumption speed
u'	Root mean squared turbulence velocity fluctuation
ε_T	u'/U_o , Normalized turbulent fluctuation velocity
A_L	Local burning area
R_{22}	Spatio-temporal correlation of velocity fluctuations normal to the nominal flame surface (2D-flame).
$R^{NL}_{\xi'\xi'}$	Non-local spatio-temporal slope correlation function
$R^{L}_{\xi'\xi'}$	Spatio-temporal slope correlation form local kinematic response theory
R_A	Estimate of spatio-temporal local burning area correlation
L_{11}	Longitudinal integral length scale
ω	Angluar forcing frequency
u_c	Phase velocity of coherent disturbances
K	U_o/u_c , ratio of mean flow velocity to phase speed of disturbances.
St_2	$\omega L_f/\left(U_o \cos^2\gamma\right)$, L_f is the height of the nominal flame
F	Total flame transfer function at the forcing frequency.
F_L	Laminar base-line of the total flame transfer function
F_T	Leading order turbulence correction $O\left(\varepsilon_T^2\right)$
$\tilde{F}$	Modeled flame transfer function at the forcing frequency
R	Combustor outer radius
Λ	L_f/L_{11}, L_f is the height of the nominal flame
f_c	Normalized local consumption speed (by s_L) in the axis-symmetric analysis
f_T	Normalized local displacement speed (by s_L) in the axis-symmetric

analysis

Modifiers

$\widetilde{\zeta}$	Modeled ensemble average
$\langle \zeta \rangle$	Ensemble averaging
$\hat{\zeta}$	Fourier Transform

Summary

This thesis describes computational and theoretical studies of fundamental physical processes that influence the heat-release response of turbulent premixed flames to acoustic forcing. Attached turbulent flames, as found in many practical devices, have a non-zero mean velocity component tangential to the turbulent flame brush. Hence, flame surface wrinkles generated at a given location travel along the flame sheet while being continuously modified by local flow velocity disturbances, thereby, causing the flame sheet to respond in a non-local manner to upstream turbulence fluctuations. The correlation length and time scales of these flame sheet motions are significantly different from those of the upstream turbulence fluctuations. These correlation lengths and times increase with turbulence intensity (i.e. u'/s_L), due to the influence of kinematic restoration. This non-local nature of flame sheet wrinkling (called 'non-locality') results in a spatially varying distribution of local consumption speed (i.e. local mass burning rate) even when the upstream flow statistics are isotropic and stationary.

Non-locality and kinematic restoration result in coupling between the responses of the flame surface to coherent acoustic forcing and random turbulent fluctuations respectively, thereby, causing the coherent ensemble averaged component of the global heat-release fluctuation to be different in magnitude and phase from its nominal (laminar) value even in the limit of small coherent forcing amplitudes (i.e. linear forcing limit). An expression for this correction, derived from an asymptotic analysis to leading order in u'/s_L, shows that its magnitude decreases with increasing forcing frequency because kinematic restoration limits flame surface wrinkling amplitudes. Predictions of ensemble averaged

heat release response from a different, generalized modeling approach using local consumption and displacement speed distributions from unforced analysis shows good agreement with the exact asymptotic result at low frequencies.

Chapter 1

Introduction

Low emissions combustion systems for land-based gas turbines, future aircraft engines, industrial heaters and boilers etc. rely on lean premixed combustion processes. These systems are exceptionally prone to combustion instabilities [1-3] that are caused due to coupling between the unsteady combustion process and the natural acoustic modes of the combustion chamber, resulting in self-excited oscillations. Such oscillations may have a detrimental effect on system performance, emissions and system hardware. A fundamental problem associated with understanding and predicting this phenomenon is a description of the interaction of harmonic velocity disturbances with a turbulent, premixed flame.

Past work in modeling flame response to acoustic perturbations has been confined to the modeling of premixed flames in laminar flows. However, practical combustion devices feature highly turbulent flows characterized upon which a coherent unsteady forcing component may be superposed when combustion instability occurs. Therefore, any modeling approach must incorporate the random spatio-temporal nature of the velocity field within its analytical framework. Further, the recent work of Santosh et al [4] has shown that the inherently non-linear nature of flame surface motions cause the ensemble averaged heat release response to be different from that predicted from laminar models. The rest of the discussion in this chapter is organized into two sections, the first section titled “Turbulent combustion” discusses aspects of this vast field of study that are pertinent to the various theoretical and numerical analyses performed in this work. The

next section titled “Combustion instability – flame response modeling” begins with a brief description of the general analysis approach to understanding the phenomenon of combustion instability. Next, the problem of heat release response modeling is introduced and recent advances in the field are reviewed.

1.1 Turbulent Combustion

Turbulent combustion is a vast field of research that aims to understand the characteristics of turbulent reacting flows. The reader is referred to the books of Peters [5] and Poinsot and Veynante [6] in order to appreciate the many issues that arise in understanding various turbulent reacting flow situations. Concepts from this body of knowledge concerning turbulent combustion of flows featuring uniformly premixed reactants that are pertinent to the analyses presented in this work will be reviewed in this section. Turbulent combustion of premixed reactants are characterized by different regimes based on a) the value of u'/s_L, i.e. the magnitude fluctuating turbulent velocity component relative to the laminar flame speed s_L and b) the value of l/δ where, l is some characteristic length scale of turbulence and δ is the characteristic laminar flame thickness [5, 7].

Turbulent combustion in many practical devices occurs in the limit where $\eta/\delta \gg 1$, where, η is the Kolmogorov length scale of the upstream turbulence. This means that the length and time scales associated with reaction-diffusion are much smaller than those of the turbulent motions of the upstream reactant flow. As such, these turbulence fluctuations cause the flame surface to distort and wrinkle, while leaving the internal structure of the flame front largely unaffected. This regime of turbulent premixed

combustion is described as the “corrugated flamelet” regime. All chemical and thermo-diffusive processes are confined to a region that is of the order of a laminar flame thickness.

In view of the above facts, turbulent premixed flames in the corrugated flamelet regime can be conceptualized as an ensemble of thin laminar ‘flamelets’ embedded in the upstream turbulent flow of premixed reactants each of which define instantaneously, the boundary between unburnt reactants and burnt products. The instantaneous propagation velocity of flamelets is given by the local laminar flame speed, s_L, modified by local flame stretch and curvature (eg. see ref. [8]).

When the turbulent length scales become comparable to overall laminar flame thickness $\eta/\delta \sim 1$, turbulent eddies now enter the preheat zone causing an enhancement of heat and species transfer between the reaction zone and the unburnt reactants. Thus, the flame structure in the preheat zone is disturbed from the laminar baseline by turbulence while the reaction zone still retains its laminar structure. This regime of turbulent combustion is known as the “Thin reaction zones” regime. With increasing turbulence intensity, local extinction of chemical reactions can occur due to intense straining of the flamelets by turbulent eddies. This results in the formation of “holes” on the flame surface. As such, this regime of combustion is called the “Broken reaction zones” regime. The instantaneous propagation velocity of the individual instantaneous flamelets will be modified from its laminar value due to the increased rate of diffusion of heat and reacting species through the preheat zone due to turbulent mixing (Peters [5]). However, as will be discussed later in forthcoming chapters, the present work assumes

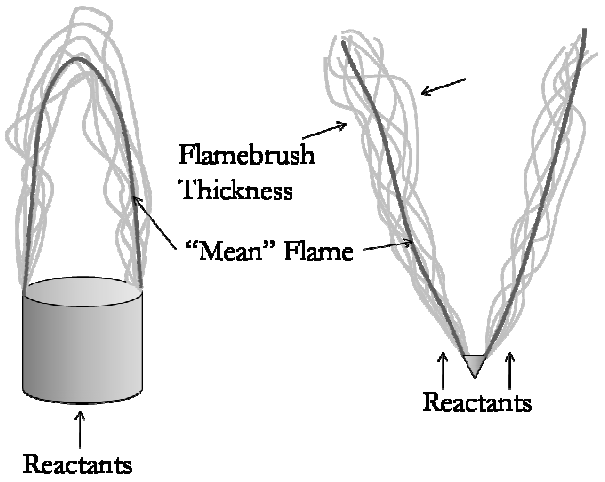

Figure 1-1: Schematic representation of turbulent flames: Conical Bunsen flame (left) centerbody stabilized flame (right)

the "corrugated flamelet" regime of turbulent combustion. Next, the key concept of "turbulent" flame speed will be introduced and discussed.

Figure 1-1 schematically shows the essential details of two canonical flame configurations i.e. the turbulent Bunsen flame and the turbulent bluff-body stabilized flame. As discussed above, these flames can be conceptualized as an ensemble of thin flamelets. Hence, it is possible to define the ensemble averaged shape of the flame rigorously as the first moment of the functional probability distribution function (PDF) over the entire sample space of laminar flamelets [9]. In the absence of coherent velocity fluctuations, this ensemble averaged flame shape simply becomes the time averaged mean flame shape as shown schematically in fig. 1-1. In practice however, the mean flame surface is usually defined to be the 0.5 contour of the ensemble averaged progress variable field ($\overline{c}$) [6].

Next, due to random flame surface wrinkling introduced by turbulent fluctuations, the above ensemble of flamelets occupies a finite volume of space. This volume is known as the "flame-brush" and is characterized by its thickness about the ensemble averaged

flame surface (shown schematically in fig. 1-1). It is well known now that for attached flames such as the above, the flame brush thickness increases with increasing distance from the flame attachment location. Due to the stochastic nature of flame surface wrinkling, the boundary of the flame brush and hence flame brush thickness is hard to characterize. Hence, the flame brush thickness is most rigorously defined as the second moment of the flame surface PDF about the previously defined ensemble averaged flame surface [9]. In many practical situations, the flame brush thickness is estimated to be the length of the included segment along the local normal to the ensemble averaged flame surface between an inner ($\overline{c}_i$) and outer ($\overline{c}_o$) contour of the ensemble averaged progress variable field. The choice of these inner and outer cutoffs is arbitrary.

A fundamental closure problem in the computation of turbulent reacting flows is developing a closure model for the average reaction rate (sub-grid reaction rate in the context of Large Eddy Simulations (LES)) (see ref. [6] for a detailed discussion). This closure problem is distinct from the closure problems associated with turbulent stresses and transport terms. A large class of closure models for the reaction rate term in computations is based on the flamelet concept described above [6]. A class of these models, known as "flame speed closure" models, is based on the idea of modeling the average reaction rate term from consideration of the augmentation of the spatial distribution of mass burning rate and rate of propagation of the ensemble averaged flame surface by turbulence fluctuations. A key concept involved in such a description in many of these models is the turbulent flame speed.

Turbulent flame speed has been the subject of intense research for the past several decades since the pioneering work of Damkohler [10] in the forties. A whole variety of

modeling approaches and experimental measurements of this quantity may be found in literature. A brief review of aspects relevant to the current work will be discussed below. Comprehensive reviews of current 'state of the art' from the standpoint of modeling and experiments may be found in the reviews of Lipatnikov and Chomiak [11] and more recently Driscoll [12].

It is possible to discern three different types of flame speed definitions from the literature as follows [12].

$$S_{T,GC} = \text{Global consumption speed} = \frac{\dot{m}}{\rho A_{ref}}$$

$$S_{T,LC} = \text{Local consumption speed} = s_L \int_{-\infty}^{\infty} \Sigma d\eta$$

$$S_{T,LD} = \text{Local displacement speed} = \left(\vec{V}_{flame} - \vec{V}_{gas} \right) \bullet \vec{n}_{LE}$$

Each of these definitions is useful in describing different scenarios as will briefly be discussed next. See ref. [12] for a more detailed discussion.

The global consumption speed, $S_{T,GC}$, as defined above, is a measure of the overall ensemble averaged mass burning rate $\dot{m}$ of the flame. The reference area A_{ref} is most often taken to be the area of the ensemble averaged flame surface. Hence, this quantity is well defined for flames with topologically compact mean surfaces such as Bunsen flames (see fig. 1). This definition of $S_{T,GC}$ is useful in situations that do not require knowledge of the spatial variation of mass burning rate.

The local consumption speed $S_{T,LC}$ overcomes this difficulty as it is defined in terms of the local flame surface density Σ [13]. The integration path as defined by Bray and Cant [14] is along the direction of the local normal to the $\overline{c} = 0.5$ contour. Thus, $S_{T,LC}$ is a

function of the spatial location on the $\overline{c} = 0.5$ contour and is a measure of the local mass burning rate. Flame speed models based on this definition may directly be used in approaches that develop closure models for the reaction rate term (eg. Zimont [15]).

The third of the above definitions describes the net propagation velocity of the ensemble averaged flame surface relative to the upstream reactant flow. A typical choice for the definition of $\vec{V}_{flame}$ is the ensemble averaged flow velocity at points just upstream of the ensemble averaged flame surface conditioned on being in reactants. The normal vector is the vector in the direction normal to the ensemble averaged flame surface. This would therefore be the definition for the flame speed model in the level-set method developed by Peters and co-workers [5]. Recently, this approach has been extended to the framework of LES by Pitsch and co-workers [16-18]. The principal idea in both frameworks involves tracking the location of the unsteady dynamics of the flame using a level-set approach. The large difference between turbulent length scales and flame thickness makes it is impractical to resolve all features of flame surface wrinkling in most applications. Hence, the influence of the unresolved sub-filter scale flame surface features on the dynamics of resolved features is modeled using a turbulent flame speed. This turbulent flame speed models the effective propagation velocity of the resolved flame surface due to unresolved/sub-filter scale wrinkling. Hence this speed is best described by a displacement speed. Peters derived an expression for the turbulent displacement speed assuming a balance between flame area destruction due to kinematic restoration and flame surface area production due to turbulent fluctuations [5]. Heuristic modeling assumptions were introduced to estimate the magnitude of the above terms in

an equation for the flame surface density. In general the displacement and consumption speeds are not the same, as has been shown in the experiments of Cheng and Shepherd [19] and Lawn and Schefer [20].

Most analyses for modeling turbulent consumption speeds and displacement speed are based on heuristic assumptions concerning the kinematic/dynamic nature of the response of a flame front to perturbations in the upstream reacting flow. Many of these models are developed from such analyses applied to the canonical case of a freely propagating flat flame into a turbulent flow of fresh reactants. However, realizing such a flame in experiments is hard as some degree of flow divergence is always required to stabilize the flame in practice [12]. It is found that in addition to the nature of the reactants and turbulence intensity, local consumption and displacement speeds show a dependence on the geometry of the flame as well as the mechanism of flame surface attachment, i.e. the flame appears to "remember" the fact that it is attached downstream of the attachment point. One of the central goals of the present work is to elucidate the physical mechanism that leads to the occurrence of this "memory" effect.

The memory effect occurs because attached turbulent flames have a mean velocity in the direction along which there is flame brush growth. The presence of a mean tangential velocity along the flame brush causes wrinkles generated at a given spatial location to move downstream along the flame brush during which time they are continuously modified by local velocity fluctuations and kinematic restoration (Boyer and Quinard [21]). Thus, flame surface perturbations show non-local characteristics, i.e. the net flame surface perturbation at a given location depends on the flame surface perturbations at upstream locations from earlier times, causing the memory effect.

In this work, an asymptotic expansion in turbulence intensity and excitation amplitude is performed to determine the ensemble averaged flame surface shape and heat release up to linear order in forcing amplitude and second order in turbulence intensity. This analysis is performed for a nominally two-dimensional flame stabilized on a prismatic centerbody. The effect of flame stretch on s_L is neglected. Complimentary computations of the G-equation are performed in order to determine the flame surface and heat-release response dynamics in the fully non-linear limit. The role of tangential advection of flame surface wrinkles along the flame brush in causing the flame surface response to the upstream flow perturbations to become non local is explicitly shown from a correlation analysis of local flame surface slope and burning area. The primary role played by flame propagation (also called kinematic restoration) in determining the characteristics of flame surface motions is also described.

Further, this flame surface response non-locality results in a spatial variation of local consumption speed. The results show that this variation can be divided into three regions depending on the influence of kinematic restoration. An explicit model for the variation of local consumption speed in the linear limit is derived and is shown to match the predicted spatial variation of local consumption speed in the near-field of the flame holder. A model for spatially varying local consumption speed due to Lipatnikov and Chomiak[11] based on the model of Zimont[15] presents a different analysis. Their analysis is based on a turbulent diffusion hypothesis applied to the governing equation for the mean progress variable. This model will also be reviewed in the light of the present results in chapter 5 of this work. The next section presents an outline of the fundamental

issues in modeling combustion instabilities in combustors with turbulent premixed flames.

1.2 Combustion instability – flame response modeling

As discussed at the beginning of this introduction, combustors in lean premixed combustion systems feature a large number of acoustic modes which can potentially couple with unsteady heat release process in the system resulting in large amplitude fluctuations in pressure and flow velocity. This phenomenon is known as combustion instability. Combustion instabilities in gas turbine combustors can result in high levels of pollutant emission and sometime damage to engine hardware from structural failures, fatigue etc. Therefore, it is essential that operating conditions at which these instabilities occur are identified during the combustor design stage itself. Hence, accurate and reliable techniques for the prediction of combustion instabilities are required.

Measurements of oscillating pressure amplitudes in gas turbine combustors have revealed that limit-cycle amplitudes are in general small compared to the mean combustor operating pressure (Dowling[22]). As such, they can be described by a linear wave equation for the acoustic pressure p in the combustor with a source term accounting for unsteady heat release as follows,

$$\frac{\partial^2 p}{\partial t^2} - c^2 \frac{\partial^2 p}{\partial x^2} = (\gamma - 1)\frac{\partial q}{\partial t} \tag{1.1}$$

where, q is the heat release rate in the combustor. Effects of temperature gradient and mean flow have been neglected in the above. The rate of growth of the amplitude of these pressure fluctuations, indeed whether they even grow at all is governed by the relative phase between pressure oscillation and the driving mechanism, i.e. unsteady heat release rate. The final limit-cycle amplitude of these perturbations is governed by damping processes in the combustor as well as non-linearity in the unsteady heat release. Thus, denoting the amplitude of the perturbation causing heat release rate to change byε, the typical variation of driving processes (H(ε)) and damping processes (D(ε)) with ε is presented schematically in fig. 1-2. At small values of ε, H(ε) > D(ε) resulting in the growth of perturbations. Eventually, damping processes increase non-linearly with ε resulting eventually in the achievement of a limit cycle at $\varepsilon = \varepsilon_{LC}$. The initial growth rate of instabilities is given by the slope of the H(ε) curve as $\varepsilon \rightarrow 0$. This initial growth rate in the context of the response of heat release rate perturbations to coherent acoustic forcing at low forcing amplitudes (Linear heat release response) is the subject of the present work. Specifically, this allows for the determination the instability characteristics of

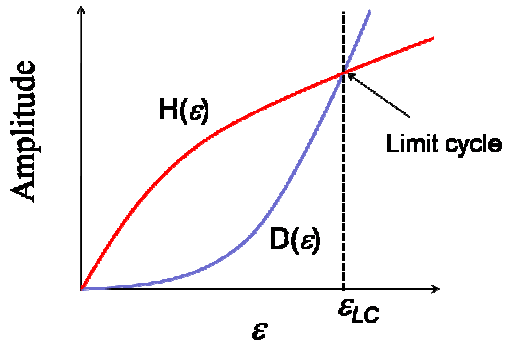

Figure 1-2: Schematic of driving and damping processes.

various acoustic modes of the system from an eigensystem analysis of eq. (1.1) (ref. McManus et al [23]).

The key problem in the modeling of combustion instabilities in lean premixed (LPM) systems is the modeling of the flame's heat-release response to imposed fluctuations in velocity, upstream equivalence ratio etc (McManus et al [23]). The magnitude and phase of these oscillations are determined by the underlying physical mechanisms that cause the flame's heat release rate to oscillate. Ducruix et al [24] discuss the most common mechanisms that can result in these heat release oscillations. There has been a large amount of research dedicated to modeling the heat release rate response of premixed flames to externally imposed perturbations[2]. The most significant of these will now be reviewed below.

In most cases of low to moderate frequency instabilities, the typical length scale of the flame zone (L) is small compared to the acoustic wavelength (λ), i.e. λ / L >> 1. Thus, the classical approach to this problem is to model the heat release rate fluctuation using the so-called 'n-τ' model. This concept was first introduced in the context of combustion instability studies in liquid-fueled rocket engines. Past investigations of interactions of premixed flames with pressure perturbations have shown that the resulting heat release fluctuations are significant at frequencies that are much higher than those associated with combustion instabilities in gas-turbine combustors (McIntosh [25]). Hence, the primary mechanism causing the heat release oscillations are due to coherent fluctuations in flow velocity only. Thus, the n-τ model in the context of lean premixed

gas turbine combustion instability analysis can be used to relate the unsteady heat release rate, $\dot{q}(t)$, to the acoustic velocity at the flame, $u'(t)$, as follows,

$$\dot{q}(t) = n u'(t-\tau) \tag{1.2}$$

Where, n is an interaction index and τ is a time lag. Thus, the above prescription implicitly assumes that the flame is compact relative to the acoustic oscillation length scales in the system. From eq. (1.2), the problem has now been reduced to determining values for n and τ for a given acoustic mode/combustor.

Fleifil et al [26] derived an expression for the unsteady burning area response of a ducted premixed flame stabilized in a flow with a parabolic mean flow profile. A kinematic equation for the flame surface derived from the G-equation (Sethian [27]) that explicitly tracks the spatial location of the flame front was used. This was used to determine the transfer function between global burning area fluctuations at the forcing frequency and the acoustic forcing. From this, models for n and τ were determined from the gain and phase respectively of this transfer function.

Ducruix et al. [28] applied the above procedure to a conical flame stabilized on a tube subjected to spatially uniform velocity perturbations. The theoretically predicted transfer function was compared with experimental measurements. Good agreement was obtained at low excitation frequencies. However at moderate frequencies, the experimentally determined transfer function gain was found to have non-monotonic frequency dependence while the theoretical result showed a monotonic decrease. The theoretically predicted phase was found to saturate while the experimental measurements showed a monotonically increasing phase.

Schuller et al. [29] recovered these moderate frequency trends using a velocity field that has a convective nature. Convection of vortices shed at the burner lip, caused by velocity forcing, results in flow velocity perturbations having a convected characteristic. The characteristic convective velocity was chosen to be equal to the mean flow velocity in their analysis. Numerical solutions of the non-linear (high excitation amplitude) limit were performed by solving the G-equation. The computed and measured transfer function gain and phase were in agreement.

Preetham et al. [30] generalized the analysis of Schuller et al. [29] to allow for general vortex convection speeds. It was shown that the presence of spatial flow non-uniformity results in the net flame surface perturbations being the superposition of a wave generated due to flame attachment and a locally generated wave due to spatial non-uniformity in the perturbation velocity field. This is again the result of the non-local nature of the flame surface response as described earlier. Thus, the heat release response transfer function was decomposed into separate contributions due to the attachment and the locally generated waves. The successive constructive/destructive interference between the two contributions results in the non-monotonic behavior of the transfer function as was observed in the experiments of Ducruix et al [28] and Schuller et al [29].

All the above analyses of flame transfer function assume that the velocity field is laminar and that flame surface motions are deterministic. As discussed earlier, both assumptions are not true in the context of turbulent premixed flames. It has become clear with advances in laser diagnostics, that combustion at turbulence levels similar to those in lean premixed gas turbine combustors, occurs in the flamelet regime (Driscoll [12]). Thus, a fundamental problem of developing a model for the ensemble averaged unsteady

heat-release response of a turbulent premixed flame to perturbations in the combustor flow-field needs to be addressed. The flow-field perturbations take the form of coherent pressure or flow velocity perturbations superposed on the random turbulence background.

Lipatnikov and Sathiah [31], made the first attempt at developing a reduced order model for turbulent premixed flame response. They applied the above kinematic modeling approach analogously to the unperturbed mean turbulent flame surface. The constant laminar flame speed was replaced with a displacement speed model that increases along the flame surface (Lipatnikov and Chomiak [11]). This displacement speed model aims to capture the effect of fine scale wrinkling introduced by the turbulence in a heuristic fashion. The transfer function obtained was compared with transfer function obtained for a flame with constant displacement speed and in the Intermediate Steady Propagating (ISP) limit [15]. The main observation is that the heat release response magnitude reduces with increasing magnitude of displacement speed values along the flame front. An increase in turbulent burning velocity will cause the coherent component of the oscillating flame surface area to decrease. Recently, the same authors have extended the above model to capture the effect of axially convected velocity disturbances as well [32].

Santosh et al [4] performed computations of forced Bunsen flame response in a randomly varying background flow using the full G-equation. The random background was spectrally band-limited and isotropic. The random velocity fluctuations were advected at the mean flow velocity using Taylor's hypothesis. The ensemble averaged flame response was compared with the laminar response of an equivalent flame that had the same unforced flame height as the forced turbulent flame. This is equivalent to the

analysis of Sathiah and Lipatnikov in the sense that a generalized laminar formulation has been used with an augmented 'turbulent' burning velocity to determine the heat release response of the turbulent flame. It was shown that the computed ensemble averaged response magnitude of the turbulent flame was lesser than the magnitude predicted by the "turbulence corrected" laminar model. Thus it was suggested that the kinematics of flame wrinkling generated due to turbulence fluctuations and coherent forcing are coupled resulting in a change in the net ensemble averaged heat release response. This coupling occurs because of the inherent non-linear nature of flame surface response to velocity fluctuations.

There are two processes that cause the flame surface response to become non-linear. The first is the fact that the flame surface wrinkles in response to the local flow velocity perturbations. Second flame surface propagation along the local normal direction causes the formation of discontinuous corners on the flame surface even if the initial flame shape was wrinkled in a smooth and continuous manner. Both these processes result in kinematic coupling. The explicit form of these coupling terms will be determined from an asymptotic analysis presented in the first part of chapter 6 of this thesis for an axis-symmetric flame stabilized on a round center body.

Next, recognizing that the nominal flame shape (i.e. flame shape if the flow were unforced and laminar) upon which the asymptotic analysis in chapter 6 is based upon is difficult to determine in practical situations. A modeling methodology which is a generalization of past modeling approaches [31-33] based on the ensemble averaged flame surface dynamics is proposed in terms of models for local displacement and consumption speeds. This modeling approach is then used to predict the transfer function

of the flame for the presently considered configuration using two different flame speed models. The first of these is a local consumption/displacement speed model for an unforced turbulent flame derived from the asymptotic analysis. This model accounts for non-local flame response but not kinematic coupling. The second model is the local consumption speed model of Lipatnikov and Chomiak [11]. This is done in order to compare predictions from their model with the exact asymptotic result developed in this work.

The remainder of this thesis is organized as follows. Chapter 2 provides relevant theoretical details about the G-equation that is central to all the analysis performed in this work. This is followed by a description of the numerical formulation in chapter 3. The various simplifying assumptions made in this work are introduced and discussed as well. Chapter 4 presents details of the asymptotic analysis for the unforced, nominally two-dimensional flame stabilized on a prismatic center body. The results required to show the non-local nature of flame surface response are formulated in this chapter. Chapter 5 presents results from the analysis in chapter 4 together with results from computations in order to elucidate the non-local nature of flame surface response. Chapter 6 presents the theoretical formulation for the exact (to the extent of simplifying assumptions) leading order correction to the ensemble averaged flame response. The modeling methodology mentioned earlier is also formulated here. Chapter 7 discusses the influence of kinematic coupling on heat release response. It is shown that at high frequencies, the response gain increases in contrast with the corresponding laminar result. The implications of these characteristics on combustor stability are discussed. Comparison between results from the modeling approach and the exact asymptotic formulation are presented and discussed in

this chapter as well. Chapter 8 concludes this thesis with a summary of the principal results and provides recommendations for future work. In addition to the above chapters a set of appendices A-F present material that support the discussion in the main chapters.

Chapter 2

Flame front tracking – G-equation

Combustors in lean-premixed systems feature highly turbulent flows that are characterized by random spatio-temporal variations of flow properties over a wide range of length and time scales. As discussed in the previous chapter, turbulent premixed combustion can be divided into different regimes based on the relative difference between flow length and time scales and the characteristic length and time scales associated with the reaction-diffusion processes.

The analyses performed in this work assume the "corrugated flamelet" regime of turbulent combustion. In this regime the instantaneous flame surface can be treated as a thin boundary separating unburnt reactants and burnt gases. Also, this boundary propagates normal to itself at the local laminar flame speed (s_L) relative to the upstream reactant flow. The value of this flame speed is determined by the thermo-diffusive and chemical properties of the upstream reactant mixture. Hence, the spatio-temporal evolution of these flamelets can be tracked using the G-equation introduced initially by Markstein [34].

This chapter presents the theoretical derivation of the G-equation in the following section. The section that follows also discusses properties of this equation that are essential in the formulation of the theoretical/computational analyses in presented in forthcoming chapters. The derivation as presented is general and no assumption has been made concerning the laminar flame speed s_L at this stage save for the "corrugated flamelet" regime assumption as discussed above.

2.1 G-equation Formulation

Figure 2-1 schematically shows an instantaneous snapshot of a flamelet wrinkled by flow turbulence. Also shown is an arbitrary two dimensional co-ordinate system. The broken curve in fig. 2-1 is a schematic representation of the flame surface separating reactants and products. This surface can be represented as an iso-surface (level-set) of a three-dimensional function of spatial co-ordinates and time, $G(x, y, z, t)$. The value of G at points that do not lie on the flame surface are defined such that the function has negative values at points that are in the reactant flow field and positive values at points in the products. These values have no physical significance and maybe chosen arbitrarily as a consequence of the generalized scaling symmetry of the G-equation (Oberlack [9]), provided that the resulting function increases monotonically across the flame surface and is sufficiently differentiable at points that lie on the flame surface.

Next, it is assumed that some arbitrarily chosen level-set of $G(x, y, z, t)$ having the value G_o, i.e. the set of points (x, y, z) such that $G(x, y, z, t) = G_o$ tracks the location of the flame surface at all times. Therefore, the total derivative of G must vanish at all points

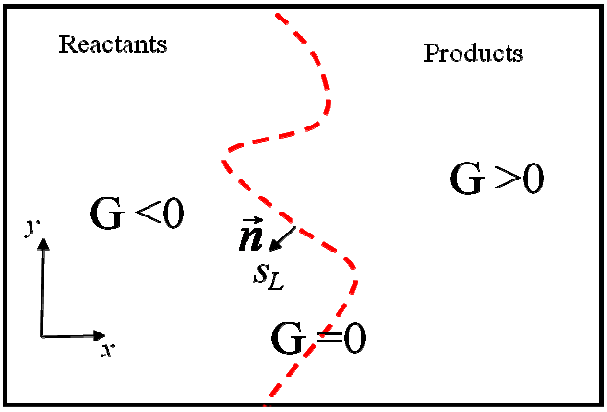

Figure 2-1: Instantaneous snapshot of a wrinkled laminar flamelet (schematic) as a boundary between products and reactants. Also shown schematically are the local normal vector to the flame surface and the laminar propagation speed.

that are members of this level-set (and hence lie on the flame surface) as follows,

$$\left.\frac{dG}{dt}\right|_{(x(t),y(t),t)} = 0 \tag{2.1}$$

Expanding the LHS of the above equation using partial derivatives yields the following for each point that lies on the flame surface,

$$\frac{\partial G}{\partial t} + \vec{u}_{flame} \bullet \nabla G = 0 \tag{2.2}$$

Note that eq. (2.2) is just the Eulerian equivalent of the Lagrangian form in eq. (2.1). Thus, flame surface motions are tracked in an *implicit* manner, i.e. as the iso-surface $G(x, y, z, t) = G_o$.

The advection velocity, $\vec{u}_{flame}$ is the instantaneous velocity of the flame surface corresponding to the points at which eq. (2.2) is defined. This velocity is the resultant of the flow velocity in the current reference frame just upstream of the flame surface, $\vec{u}$ and the laminar burning velocity, $s_L\vec{n}$, which therefore can be written as: $\vec{u}_{flame} = \vec{u} + s_L\vec{n}$. Using this result in eq. (2.2) yields after a little rearrangement,[1]

$$\frac{\partial G}{\partial t} + \vec{u} \cdot \nabla G - s_L \left|\nabla G\right| = 0 \tag{2.3}$$

The above equation is valid in general at high turbulence intensities when the flame is highly wrinkled and forms pockets provided local extinction re-ignition events that cause holes to form on the flame surface, do not occur. The effect of diffusion and chemical

---

[1]Since the flame is a contour of G(x,y), the local normal to the flame surface pointing into reactants can be expressed as $\vec{n} = -\nabla G / \left|\nabla G\right|$. This has been used to derive eq. (2.3).

reaction processes that occur on scales comparable to the laminar flame thickness are captured by the specification of the dependencies of the flame speed s_L on a combination of parameters, viz.- local flame-front geometry and flow properties such as flame front curvature and stretch (ref. Law and Sung[9]) and local upstream equivalence ratio.

Conventionally, the zero level-set, i.e the set of points where $G(x, y, z, t) = 0$ is chosen to represent the flame surface. Further, since it is not possible to rationally define a flame speed for points that do not lie on the flame surface, eq. (2.3) is strictly well-defined only at the *flame surface*. Therefore it cannot be used to study the statistical nature of G using traditional averaging techniques (*e.g.* Reynolds averaging for the Navier-Stokes equation). Indeed, the values of G have no physical significance and hence, an analysis of the statistics of G in general to obtain insight into the statistics of flame surface motions is problematic, eg. it is not assured in general that the zero contour of a Reynolds averaged G field would coincide with the location of the flame on an average since flame surface motions are tracked in an *implicit* manner. This is because the Reynolds averaged G-equation does not possess the necessary generalized scaling symmetry that front tracking equations such as eq. (2.3) must have (ref. Oberlack *et al*[9]). Hence, in the theoretical analyses presented in forthcoming chapters, an equation that *explicitly* solves for the location of the instantaneous flame surface relative to an appropriately chosen co-ordinate system will be derived from eq. (2.3). This equation is now a 2-D field equation that can be analyzed using standard averaging techniques. The drawback of this approach is that only flame fronts that can be represented as single valued curves in some co-ordinate can be analyzed. This restricts the validity of the analyses to the limit of low intensity large scale turbulence. At higher turbulence intensities, a computational

approach to solving eq. (2.3) must be adopted. The details of this computational approach adopted in the present work are described in the next chapter.

Chapter 3

Numerical Formulation

The instantaneous flame surface becomes highly wrinkled at high turbulence intensities. It is also possible that pockets of reactants/products might separate from the flame surface at these turbulence intensity values resulting in the flame surface becoming multiply connected. Further, kinematic restoration, i.e. the propagation of the flame surface sheet into the reactants along the direction local normal to the flame surface, causes the formation of corners on the flame surface. This is a non-linear process whose effect cannot be completely captured by theoretical approaches as will be seen in the forthcoming chapters. Hence, the *G*-equation must be solved numerically in order to fully capture the effect of kinematic non-linearities and pocket formation on flame surface motions and quantities that depend on its characteristics. This chapter describes the various numerical schemes that have been employed in this thesis to solve the *G*-equation computationally.

The principal assumptions that are made in the present numerical analysis (as well as the forthcoming theoretical analyses) are as follows,

1. Corrugated flamelet combustion regime. i.e. the flame is a thin boundary separating products and reactants with an instantaneous propagation velocity equal to the laminar flame speed.

2. The effect of flame stretch and curvature on the laminar flame speed is neglected.

3. The effect of gas expansion at the flame surface on the upstream flow field is neglected.

4. The mean flow is a parallel steady flow along the z-axis. The value of the mean transverse velocity component due to the presence of the flame-holder is assumed to be small when compared to the axial component.

5. The flame is assumed to be attached to the flame holder at every time instant.

6. The upstream turbulence fluctuations are stationary and isotropic. These fluctuations propagate along with the mean flow (Taylor's hypothesis).

The implications of the above assumptions are discussed below.

Assumption 1 allows for a G-equation formalism to capture flame surface motions. Assumption 2 and 3 are made mainly in order to simplify theoretical analysis of flame surface motions that will be presented later. Thus, in order to be able to understand the present numerical results using the insights obtained from theoretical analyses, these assumptions are retained in the present numerical formulation as well.

Next, the solution of eq. (2.3) requires specification of the turbulent velocity field. Therefore, in general, eq. (2.3) must be solved simultaneously with the governing equations for the flow-field in the regions upstream and downstream of the flame surface together with appropriate jump conditions relating changes in flow properties across the flame surface. This entails solving the non-linear Navier-Stokes equations subject to time varying boundary conditions at an unsteady boundary. It is not possible to derive a closed form analytical solution in general. Hence in the interest of analytical tractability, the temperature jump across the flame surface is ignored (i.e. assumption 3. Consequently,

the alteration of the upstream reactant flow-field at the flame surface due to the temperature jump is ignored and the upstream flow-field can be specified without solving the flow equations. These results are rigourously valid in situations where the burnt to unburnt gas temperature ratio (T_b/T_u) is close to unity e.g. vitiated flows. The substantially reduced complexity of the approach facilitates an understanding of the impact of flame surface motions on the local consumption speed etc. This approach has also been shown to give good agreement with experiments that measure the heat release response of a laminar flame to acoustic forcing in many instances (e.g. Ducruix et al [35]). Further, Preetham et al [30] have argued that the qualitative dynamics of the flame are captured as long as the excitation amplitudes are lesser than the value for which parametric instabilities occur, e. g. for $T_b/T_u > 3$, $u'/s_L > 4$ (Bychkov [36]). However, to facilitate a theoretical understanding of the impact of velocity fluctuations on flame surface motions which in turn govern averaged properties such as local consumption speed, assumption 3 will be retained. Thus, the results developed in this work do not account for the influence of flame front instabilities eg. the Darrieus-Landau instability. The underlying laminar flame speed is constant in this analysis and assumption 5 implies that the results of the present work are valid only for attached flames.

Thus, the temperature jump across the flame surface is neglected and the flow-field upstream and downstream of the flame surface is assumed to be incompressible. Turbulent velocity fluctuations perturbing the flame are specified by using a time varying three dimensional field of random numbers that is divergence free (i.e. satisfies mass conservation) isotropic and stationary. These velocity fluctuations are advected along the mean flow in accordance with Taylor's hypothesis (assumption 6).

The rest of this chapter is organized as follows. The next section titled 'Theoretical considerations' presents a brief overview of the theoretical background of the level-set method that is used to solve the *G*-equation. Next, the section titled 'Numerical schemes' presents the various numerical schemes and algorithms used to solve the level-set equation and the associated auxillary equations. A brief overview of the local level-set method that affords considerable reduction in computation time is presented in the section titled 'Local level-set method'. Details of turbulence generation are described in the final section titled 'Velocity field model'.

3.1 Theoretical considerations

This section discusses mathematical properties of the G-equation that are pertinent to the construction of numerical solution schemes. The various techniques involved in solving this equation have over the past three decades come to be called the level-set method. As introduced in chapter 2, the flame surface is represented implicitly by an iso-surface of a function $G(x,y,z,t)$ of one higher dimension than the flame surface in time. A different nomenclature for an isosurface is a 'level-set' defined formally, as follows,

$$\Gamma\left(G = G_o\right) = \left\{\left(x, y, z\right) : G\left(x, y, z\right) = G_o\right\} \tag{3.1}$$

Thus, it is clear from the above that a level-set corresponding to G_o essentially represents the iso-surface $G(x,y,z,t)=G_o$. Typically, the zero level-set (i.e. $G_o=0$) of this function is chosen to represent the flame surface. This choice, made in this work as well however, is arbitrary. The governing equation that describes the temporal evolution of the level-sets of G is called the G-equation (alternatively 'level-set' equation) was introduced in chapter 2 (eq. (2.3) in chapter 2) and is repeated here for convenience,

$$\frac{\partial G}{\partial t} + \vec{u}\left(\vec{x},t\right).\nabla G = s_L \left|\nabla G\right| \tag{3.2}$$

The above equation can be rewritten in the following form as a non-linear advection equation[2].

$$\frac{\partial G}{\partial t} + \left(\vec{u}\left(\vec{x},t\right) - s_L \frac{\nabla G}{\left|\nabla G\right|} \right).\nabla G = 0 \tag{3.3}$$

The term within the parentheses in the second term on the LHS represents the non-linear advection velocity. Equation (3.3) is valid even when the flame surface forms pockets (and hence becomes multiply connected) as the function G(*x*,*y*,*z*,*t*) is still well defined for such surfaces. The level-set method is an "Eulerian" front tracking method because the front's location is tracked by solving a field equation in a fixed region of space.

The aim of the level-set method is to determine the time evolution of the zero level-set (i.e. flame surface) of *G* using eq. (3.3). The values of *G* in space and time have no physical significance and are indeed of little interest beyond their utility in constructing methods to explicitly find the zero level-set, i.e. determine explicitly the set of points $\Gamma\left(G = G_o\right)$. Further, the evolution of the zero level-set is independent of the evolution of any other level-set. This is a consequence of the *generalized scaling symmetry property* of eq. (3.3). A symmetry is a transformation G^*=*F*(G) which leaves eq. (3.3) formally unchanged. The generalized scaling symmetry can be stated in terms of a bijective transformation function *F* as follows (Oberlack *et al*[9]).

---

[2] To see this write $s_L \left|\nabla G\right|$ as $s_L \left(\nabla G \bullet \nabla G\right) / \left|\nabla G\right|$ and substitute in eq. (3.2).

$$G^* = F(G) \quad \text{such that} \quad \frac{dF}{dG} > 0 \tag{3.4}$$

Note that the above transforms eq. (3.3) to an identical equation in terms of G^*. The implication of eq. (3.4) is that the transformation simply reassigns the zero level-set to a different value in terms of G^* but does not change its shape. Since, the choice of zero level-set is itself arbitrary in the first place, the same statement holds for any level-set G_o, whence, it follows that the evolution of the level-sets of G governed by eq. (3.3) are independent of each other.

Thus, in theory the values of G at points that don't lie on the zero level-set can be chosen somewhat arbitrarily provided they satisfy the aforementioned generalized scaling symmetry property. However, since, eq. (3.3) is a non-linear advection equation, it is possible that gradients in the G-field can steepen into discontinuities (especially near the zero level-set) as the solution evolves in time causing numerical oscillations. This might result in the possible corruption of the shape of the zero level-set. Therefore, in practice it is advantageous to choose the function G to always be a Signed Distance Function (SDF) from the flame surface, defined as follows,

$$\begin{aligned} G(x,y,z) &= \begin{cases} d(x,y,z) & (x,y,z) \in \text{Products} \\ -d(x,y,z) & (x,y,z) \in \text{Reactants} \end{cases} \\ d(x,y,z) &= \min_{(x',y',z') \in \Gamma(G=0)} \sqrt{(x-x')^2 + (y-y')^2 + (z-z')^2} \end{aligned} \tag{3.5}$$

Clearly, the above ensures that G has the value zero on the flame surface. SDFs are continuous and differentiable everywhere even when the flame shape is multiply connected. In addition, the magnitude of the slope of these functions is unity everywhere, i.e. $|\nabla G| = 1$ at all points. Figure 3-1a illustrates a typical SDF in two dimensions for a

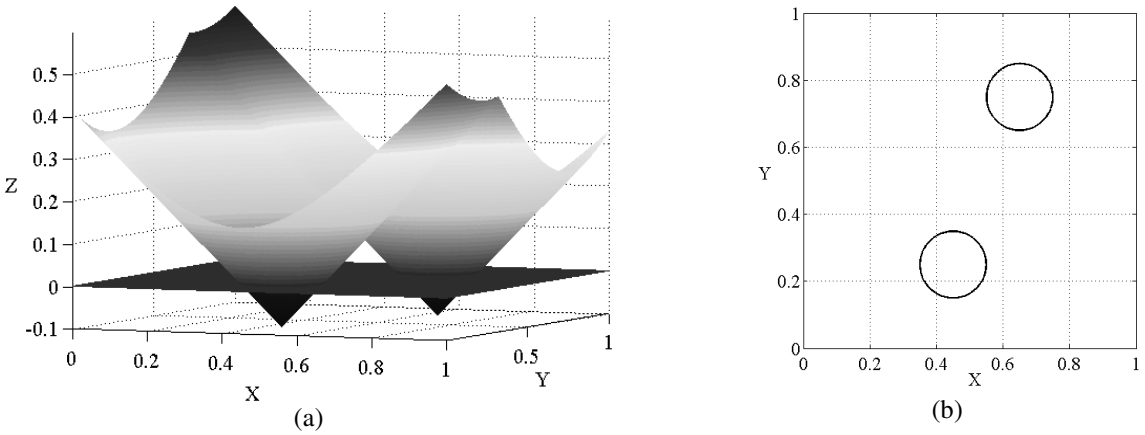

Figure 3-1: a) Typical signed distance function. Also shows a cut plane at z=0. b) The corresponding zero level-set.

zero-level set that consists of two circles (see Figure 3-1b). Notice that the SDF is continuous and smooth even though the underlying zero level-set is multiply connected. As an aside, note that the choices made for G in chapter 2 are not exact distance functions in the sense of eq. (3.5) but do represent continuous and differentiable distance functions in some sense.

Next, the flame speed s_L, is undefined everywhere except on the zero level-set. In a practical computation using the current framework the zero level-set location is implicitly known albeit in a discrete sense, i.e. the set of points on the zero-level set might not always correspond to grid

nodes. Thus, the flame speed at all points in the domain is assumed to be the same as s_L. While this choice has no physical significance (and does not influence the evolution of the zero level-set), it ensures that the flame speed at the *flame surface* is correctly specified.

As the solution evolves in time, the different level-sets of G must propagate at a constant velocity relative to each other in the direction along the local normal in order to maintain the overall distance function character of the G-field. This however, is not

assured in general because of inherent spatial and temporal variations in the flow velocity, $\vec{u}$. Hence the *G*-field is periodically *reset* during the course of the computation to be a signed distance function from the new location of the zero level-set at that time. This must be done in a manner as to not disturb the location of the zero level-set. This operation is known as 'redistancing' or 'reinitialization'. The most popular procedure for doing this is the PDE based reinitialization technique described briefly below (Sussman et al[37]).

The following equation is solved to steady state periodically during the course of computation to reset the G-field to a signed distance function,

$$\frac{\partial G}{\partial \tau} + S\left(G^0\right)\left(\left|\nabla G\right| - 1\right) = 0 \tag{3.6}$$

Where, G^0 is the *G*-field before reinitialization and τ is a pseudo-time variable with no relationship to the time level of the computation. The function, $S\left(G^0\right)$ is defined as follows,

$$S\left(G^0\right) = \begin{cases} 1 & G^0 > 0 \\ 0 & G^0 = 0 \\ -1 & G^0 < 0 \end{cases} \tag{3.7}$$

It is clear that the steady state of the above equation yields $\left|\nabla G\right| = 1$. Once this has been accomplished, the computation of the zero level-set evolution using eq. (3.3) is resumed. Reinitialization may be conceptualized as an application of a transformation on the *G*-field that satisfies the generalized scaling symmetry property (eq. (3.4)) mentioned earlier with the zero-level-set being an identity of this transformation. Hence, its subsequent

evolution must remain unaffected. The details of numerical implementation will be described next.

3.2 Numerical Formulation

All computations in this work were performed on a cuboidal domain oriented along the x, y and z axes as shown in fig. 3-2. All dimensions/lengths have been normalized using the integral length scale of the turbulence in the following sections. The extent of the domain in the z direction was determined from the sum of the offset of the flame holding location from the base of the domain (h_a = 10) and the nominal height of the flame (i.e. without turbulence or acoustic forcing). In practice the nominal height of the flame attached to a prismatic or axis-symmetric centerbody is imposed, either by the flame meeting with the sides of the combustor in the case of confined flames or due to extinction cause by diffusion of reactant from the premixed stream into the surroundings in the case of open flames. Since the flow field is being prescribed rather than being solved for in this work, this nominal height in the present framework is technically infinite. However, this was chosen to be 15 times an arbitrarily chosen lateral extent for the flame of r_o = 3.3 from the central axis of the domain. This yields a nominal flame angle $\gamma \sim 4^o$. The domain was discretized using a uniform structured grid with constant grid spacing along the x, y, and z directions. The number of points along the x and y directions was chosen to be 201. From considerations of memory requirements and speed as also resolution of fine scale features of the flame wrinkling, the grid spacing was chosen to be Δx = 0.1 (see Appendix A). The spatial extent along the z- direction was chosen so as to be able to capture the features of flame surface dynamics for a distance of

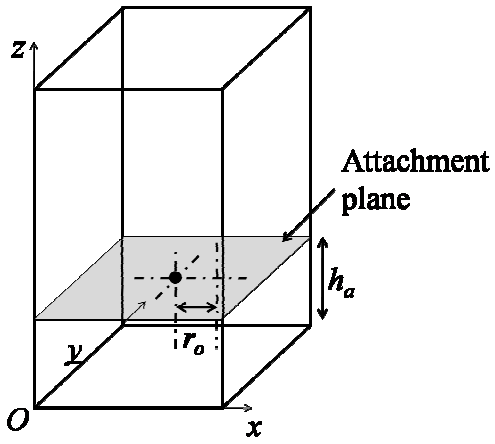

Figure 3-2: Schematic of the computational domain showing the location of the flame attachment flame. Also shown are the attachment plane location h_a and lateral extent of the flame r_o.

s~55 from the flame holder along the nominal flame surface. The numerical schemes used to solve eq. (3.3) and eq. (3.6) are described next.

Equation (3.3) is solved using the semi-Lagrangian CIR (Courant-Isaacson-Rees) scheme. Denoting the advection velocity by $\vec{u}_{flame}$, eq. (3.3) can be written as follows,

$$\frac{\partial G}{\partial t} + \vec{u}_{flame}.\nabla G = 0 \tag{3.8}$$

Given the solution at time-level *n* the CIR scheme updates the solution at time-level *n*+1 by extrapolating the solution to this time level along the characteristics of eq. (3.8) as follows,

$$G\left(\vec{x}_{ijk}, t^{n+1}\right) = G\left(\vec{x}_{ijk} - \vec{u}^{n}_{flame}\Delta t, t^{n}\right) \tag{3.9}$$

Where, the vector $\vec{x}_{ijk} = \left(x_i, y_j, z_k\right)$ represents the co-ordinates of grid point (*i*, *j*, *k*). Equation (3.9) represents a linearized explicit scheme because the advection velocity is evaluated using the values of *G* at the current time level, *n*. The above scheme is first order in space and time and stable for any Δt. However, in order to avoid excessive

degradation of the solution due to numerical diffusion Δt must be $O(\Delta x)$. In all the computations that were performed in this study Δt was set to equal $0.1\,\Delta x$.

Significant improvement in solution quality can be obtained by extending the above scheme to one that is second-order accurate in time and space using the Back and Forth Error Correction algorithm (BFECC) (Dupont and Liu [38]). This algorithm is as follows,

1. Solve eq. (3.8) forward in time using the first order scheme in eq. (3.9). Let this solution G^*.
2. With G^* as the initial value at time $t+\Delta t$, solve eq. (3.8) *backward* in time using the same CIR scheme. This involves solving the time reversed form of eq. (3.8) (obtained by replacing t by $-t$ in eq.(3.8)) forward in time through one time step with G^* as the initial value. Let this solution be G^{**}.
3. Finally, solve eq.(3.8) forward in time using the scheme in eq. (3.9) using $G^n - (G^{**}-G^n)/2$ as initial data to obtain the solution G^{n+1} at time level $n+1$.

The above BFECC algorithm is very easy to implement. The CIR scheme together with BFECC has been shown to have significantly lower numerical diffusion when compared to similar and higher order counterparts. A heuristic argument to explain why the above procedure might yield higher order and better accuracy is as follows. The difference between G** and G from steps 1-2 estimates twice the error accrued from using the CIR scheme over a time step at time level n. In step 3, the initial data is offset by an amount equal to this error before propagation to the next time level. Now, the error introduced is compensated for by the initial offset yielding a more accurate value for the solution at the next time level. This procedure may be applied to any odd order scheme to obtain one order higher level of accuracy. The derivatives of G in the advection velocity

(see eq. (3.3)) were determined using the method described in (Dupont and Liu [38]). This is described for the case of the *x*-component below. The other components are similarly evaluated.

1. One sided differences $G^{+}_{x,i} = \left(G_{i+1,j,k} - G_{i,j,k}\right)\big/\Delta x$ and $G^{-}_{x,i} = \left(G_{i,j,k} - G_{i-1,j,k}\right)\big/\Delta x$ are determined.
2. If $G^{+}_{x,i} G^{-}_{x,i} > 0$, then $G_{x,i} = \left(G^{+}_{x,i} + G^{-}_{x,i}\right)\big/2$.
3. If $G^{+}_{x,i} G^{-}_{x,i} < 0$, then $G_{x,i} = \text{maxmod}\left(G^{+}_{x,i}, G^{-}_{x,i}\right)$ where,

$$\text{maxmod}\left(a,b\right) = \begin{cases} a & |a| > |b| \\ b & otherwise \end{cases}.$$

The above ensures better accuracy in determining components of the local normal when two segments of the flame surface are about to merge just before pocket formation).

Equation (3.6) can also be rewritten as an inhomogeneous non-linear advection equation as follows,

$$\frac{\partial G}{\partial \tau} + \left\{ S\left(G^{0}\right)\left(\frac{\nabla G}{|\nabla G|}\right)\right\} \bullet \nabla G = S\left(G^{0}\right) \tag{3.10}$$

The above equation can be solved using a low cost explicit first order upwind scheme. The derivatives required to determine the advection velocity (term in braces on the LHS of eq. (3.10)) are determined in the same way as described for the level-set advection. Note that in the ideal case, the reinitialization scheme must not move the location of the zero-level set. However, due to the effect of numerical diffusion cause by discretization, this scheme will displace the zero level-set by small amounts of $O\left(\Delta x\right)$. The reasons for this is because the characteristics of eq. (3.10) (and hence eq. (3.6)) propagate function

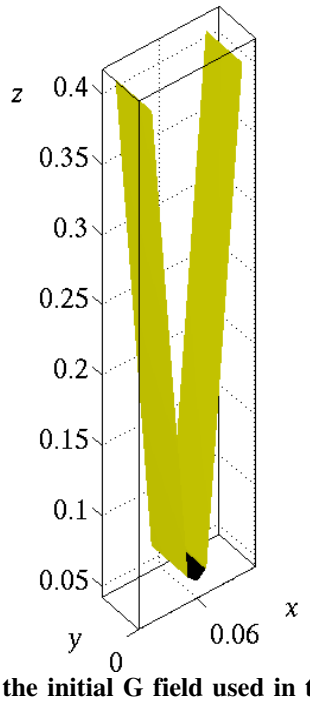

Figure 3-3: Typical zero level-set of the initial G field used in the present computations: nominally 2D flame. The mean flow direction is along the z-axis. The black segment in the above shows the segment of the zero level-set that behaves as the flame holder. Flame holding location is a z = 0.06 m.

values along the orthogonal trajectories of the level-sets of the G field, away from the zero level-set. Evaluation of derivatives in keeping with this underlying nature of of eq. (3.10) requires that these be evaluated without using function

values on either side of the zero level-set. However, this is not possible in numerical computations such as those performed in this work since it is not assured that the zero-level set always passed through grid points. Several fixes have been proposed to reduce the error due to this problem e.g. Russo and Smereka [39], Sussman and Fatemi [40] and Dupont and Liu [38]. The latter fix has been used in this work due to the simplicity of implementation. Accordingly, the level set is updated by the reinitialization scheme only at grid points where the absolute value of the difference of G^0 values between the grid point and any of its 26 neighbours is greater than $1.1\Delta x$. This ensures that the diffusion errors introduced due to incorrect finite differencing in the vicinity of the zero level-set

are introduced only when absolutely necessary. A pseudo-time step ($\Delta\tau$) of $0.3\Delta x$ was used in this work. Further, the maximum number of reinitialization operations per level-set advection time step was limited to 10 for all the results obtained in this work.

Two sets of computations were performed. First, the response of a nominally two-dimensional flame stabilized on a prismatic centerbody aligned along the *y*-direction, to only turbulence fluctuations and second, the response of a nominally axis-symmetric centerbody stabilized flame

to coherent forcing. These will be identified to as the two-dimensional and axis-symmetric cases henceforth for the sake of brevity. Figures 3-3a and 3-3b show the details of the zero level-sets for typical initial values for the *G*-field employed in the two dimensional and axis-symmetric computations respectively. The flame holder itself is an integral part of the zero level-set (shown as black). Note that the prescribed flow field approach adopted in this study does not resolve the details of the boundary layer and recirculation zone behind the flame holder. Hence in order to attach the flame, the segment of the zero level-set corresponding to the flameholder must be left untouched by the computations, i.e. neither advection nor reinitialization must be performed in a band of grid points around the flame holder, thereby ensuring that the flame will stay attached. This can be very easily achieved by a simple extension of the localization procedure proposed by Peng et al [41]. A brief discussion of the local level-set method is presented next.

3.3 Local Level-set method

This approach is also known as the banded level-set approach. As discussed earlier, the evolution of the zero level-set of the level-set function G is independent of the evolution of other level-sets. Therefore, it is sufficient to perform level-set advection and reinitialization in a small band of grid points that surround the zero-level set, thereby resulting in significant reductions in computation time. This band of grid points is constructed before every advection step and evolves in time so as to always contain the zero level-set. Since computations are performed only within a small neighbourhood of the zero level-set, this method is called the 'Local' level-set method. The complete details of the algorithm are described in Peng et al [41]. The basic features of this algorithm will be described here.

This algorithm works only if G is defined to be a signed distance function from the zero level-set following eq. (3.5). Let the set of grid points that discretize the domain be denoted by *D*. A band of grid points called the "Advection tube" around the zero level-set is defined as follows,

$$T = \left\{ (i,j,k) : \left| G(i,j,k) \right| \le \beta, \forall (i,j,k) \in \Omega \subseteq D, \beta > 0 \right\} \tag{3.11}$$

Where, Ω is any subset of grid points that completely contains the zero level-set (see eq. (3.1)). The parameter β defines the thickness (in terms of number of grid points) of the advection tube around the zero level-set. Next, a second tube band the "Reinitialization tube" that contains the above tube is defined as follows,

$$\begin{aligned} N &= \left\{ (i+l, j+m, k+n) : \forall (i,j,k) \in T \text{ and } (l,m,n) \in H \times (H \times H) \right\} \\ H &= \{-h, -h+1, \ldots, h-1, h\} \subset Z : h > 0 \, and \, h \in Z \end{aligned} \tag{3.12}$$

The parameter h is called the "Tube halo" parameter. The set Z in the above is the set of integers. Thus, the steps in the local-level set algorithm are as follows,

1. For specified parameters β and h form the reinitialization tube N, identify the set of points that belong to tube T.
2. Perform level-set advection using appropriate numerical schemes at all points in T.
3. Perform the reinitialization at all points in N to restore the values of the G field at these points to be a signed distance function from the zero-level set.
4. Set $\Omega = N$ and revert to step 1.

Step 3 ensures that the tube N moves with the zero level-set as the computation progresses. Step 4 is a variation on the algorithm of Peng et al[41] to improve computation speed. The tube construction in step 1 needs a '*mask*' value associated with every grid point that is used to prevent points from being included in tubes T or N multiple times (see Peng et al [41] for details). This mask value is used as follows. Once a grid point has been included in T its mask value is set to equal 1. Further, when a point is included in N but not in T its mask value is set to 2. Thus, the value of the point's mask variable is checked for these two states before including it in tube N. The mask values of all points are initialized arbitrarily to zero at the start of the computation. Clearly, it is possible to extend the algorithm by defining a third mask state (say 3) which overrides the conditions in eqs. (3.11) and (3.12) to eliminate arbitrarily shaped sets of grid points from the mesh from being included in N. This means neither computations of level-set advection nor reinitialization happens at these points. As such, in this work, a band of points surrounding the flame holder were masked out of the computational domain with

the result that the zero-level set at these points was unaffected by the flow velocity fluctuations and flame propagation; thus, simulating flame attachment. Another way to conceptualize this procedure is to think of it as redefining the computational domain D for the problem as being all grid points points except those in the neighbourhood of the flame holder.

Finally, the values for the localization parameters β and h were chosen to be $5.0\Delta x$ and 1 respectively. These choices were based on the requirement that there always be at least one complete stencil of the CIR scheme around the zero level-set in the tube. All the above procedures were implemented as a general 3D level-set tracking infrastructure called LSGEN3D. The implementation was developed in a multithreaded manner using OPENMP in order to take advantage of the currently new generation of multi-core shared memory computers. Next, the details of velocity field specification and turbulence generation will be discussed.

3.4 Velocity field model

Consistent with the assumptions made in the previous chapter, the velocity field in the current computations in prescribed rather than solved for. This is done for two reasons. Firstly, the aim is to compare the numerical solution with the linear theoretical solutions in order to study the effect of non-linearity on the non-local nature of the flame response. Secondly, physical processes controlling the flame response are independent of how the turbulence field was generated. Hence the computationally cheaper approach of specifying the velocity field has been adopted so that a larger parametric space could be explored.

The velocity field for the two-dimensional simulations was composed of spatially isotropic turbulence fluctuations superposed on a mean flow velocity along the positive z-direction. The turbulence fluctuations are advected along with the mean flow in accordance with Taylor's hypothesis. A 1-D linear advection equation for each turbulence component was solved using a simple standard first order backward difference scheme at all grid points. The advection velocity along the z direction was chosen to be the same as the mean flow. Inflow conditions were prescribed at z=0 for all three velocity components. The advection time step was chosen to equal the grid spacing (since the advection velocity is unity) to eliminate numerical diffusion errors. Spatial isotropy together with Taylor's hypothesis implies that spatial correlations of the turbulence fluctuations do not change with time, i.e. the turbulence fluctuations are statistically stationary. This is true when turbulence decay time-scales are much larger than a flow convection time over a nominal flame height.

Inflow conditions are generated as a series of cubical M^3 boxes i.e. with 'M' grid points on each side. to correspond to the number of points in an x-y (inflow) plane of the computational domain. These inflow velocity fluctuations are pre-computed and stored as a series of x-y planes ordered by the value of the z co-ordinate using the following algorithm,

1. Generate three M^3 boxes of normally distributed random numbers with unit variance. M is the number of points used to discretize one side of the box.
2. Denote these boxes as U, V and W respectively. Transform these boxes to frequency space by taking a 3D FFT (zero padding is used in each direction) to

obtain corresponding $\tilde{U}\left(\vec{k}\right), \tilde{V}\left(\vec{k}\right)$ and $\tilde{W}\left(\vec{k}\right)$ fields in wave number space; $\vec{k} = \left(k_x, k_y, k_z\right)$ represents the wave-vector.

3. **Divergence removal**:

   a. Evaluate the projection of $\tilde{U}\left(\vec{k}\right), \tilde{V}\left(\vec{k}\right)$ and $\tilde{W}\left(\vec{k}\right)$ at every FFT point onto the corresponding wave-vector, i.e. compute $P\left(\vec{k}\right) = k_x \tilde{U}\left(\vec{k}\right) + k_y \tilde{V}\left(\vec{k}\right) + k_z \tilde{W}\left(\vec{k}\right)$.

   b. Remove the corresponding components of the projection from $\tilde{U}\left(\vec{k}\right)$, $\tilde{V}\left(\vec{k}\right)$ and $\tilde{W}\left(\vec{k}\right)$ repectively, i.e. $\tilde{U}_d\left(\vec{k}\right) = \tilde{U}\left(\vec{k}\right) - P\left(\vec{k}\right)\left(k_x \middle/ \left|\vec{k}\right|\right)$ and similarly for the other two components to obtain divergence free velocity fields $\tilde{U}_d\left(\vec{k}\right)$, $\tilde{V}_d\left(\vec{k}\right)$ and $\tilde{W}_d\left(\vec{k}\right)$.

4. **Spectral rescaling**: Rescale the energy in each shell of radius k and width Δk in the above divergence free velocity fields to correspond to a specified energy spectrum $E(k)$. This is done by evaluating the total kinetic energy in the shell, $\tilde{E}_k$ and scaling the velocity fields $\tilde{U}_d\left(\vec{k}\right)$, $\tilde{V}_d\left(\vec{k}\right)$ and $\tilde{W}_d\left(\vec{k}\right)$ at each contributing FFT point to the k-shell by $E\left(k\right)\Delta k / E_k$, where $E\left(k\right)$ is the energy spectrum of the turbulence derived from the longitudinal spatial correlation function and considerations of spatial isotropy (Pope[42]).

5. **Spectral inversion:** The scaled velocity fields $\tilde{U}_d\left(\vec{k}\right)$, $\tilde{V}_d\left(\vec{k}\right)$ and $\tilde{W}_d\left(\vec{k}\right)$ are converted back to physical space using the inverse FFT.

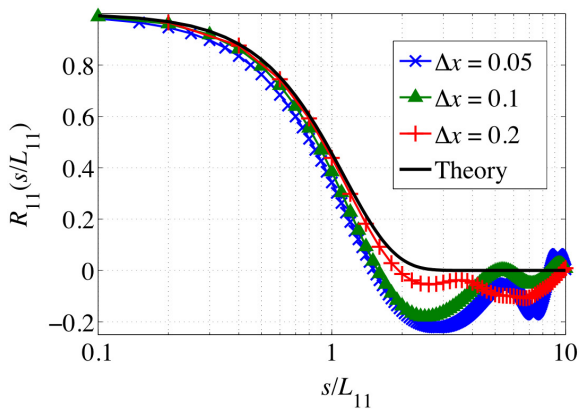

Figure 3-4: Comparison between the longitudinal correlation function of the generated turbulence field (symbols) and the corresponding theoretical targets (solid curves) for three nominal integral length scales. *M*=201, u'/s_L = 0.75.

Care must be taken in steps 3-4 to ensure that the conjugate symmetry property of the FFT is not violated by appropriately reflecting wave-vector components so that the inverse FFT in step 5 yields a purely real result. The longitudinal spatial correlation function was chosen to be the following.

$$R_{11}(s) = e^{-\left(\frac{\pi}{4}\right)\frac{s^2}{L_{11}^2}} \tag{3.13}$$

Where, L_{11} is the longitudinal integral length scale and s is the spatial separation between the two points for which the correlation is sought. The above correlation function is representative of that of low intensity large scale turbulence (Hinze[43]). Such correlation functions have been used in the prior analyses of local consumption speed of freely propagating flame flames of Aldredge and Aldredge and Williams[44]. Assuming spatial isotropy, the energy spectrum function corresponding to the above correlation function in dimensional form is given by,

$$E(k) = \frac{4L_{11}}{\pi^3} u'^2_{rms} (kL_{11})^4 e^{-\frac{(kL_{11})^2}{\pi}} \tag{3.14}$$

Figure 3-4 plots a typical result for the ensemble averaged estimate of R_{11} determined from the generated data for each of the three grid sizes. The number of grid points along the box (M) was chosen to be equal to 201. Three different values of grid spacing corresponding to Δx = 0.2, 0.1 and 0.05 were used. The solid curve corresponds to the exact theoretical result from (eq. (3.13)). Note that the agreement between the theoretical and generated correlation at large values of spatial separation degrades progressively as grid spacing decreases. The reason for this is because the number of sampling points has been maintained at 201 across different grid sizes. Thus, the resolution in frequency space decreases resulting in the above deviation. Therefore, for all numerical data that will be presented henceforth, the *effective* value of L_{11} was taken to be the the area under the generated R_{11} curve upto the value of s/L_{11} at which it crosses the horizontal axis for the first time. For the Δx = 0.1 case, this effective value was determined as $0.85L_{11}$. Turbulence inflow conditions were generated using the above algorithm for three turbulence intensities corresponding to u'/s_L = 0.75. 2.25 and 3.75. This concludes the discussion of the algorithms/numerical schemes adopted in this study. It will be shown in forthcoming chapters that useful insight into the characteristics of flame surface motions can be obtained from analysis of local burning area fluctuations. The numerical procedure adopted to determine this quantity in the present work will be described next.

The local burning area at any point on the flame surface can be determined as follows. Consider a point (s, y, 0) on the nominal flame surface. It is possible to define a rectangular tube whose axis is perpendicular to the nominal flame surface, having cross-sectional dimensions Δs and Δy. Now, if the signed distances of any point in the domain from the sides of this tube are given by d_1, d_2, d_3 and d_4, the area of the patch of the flame

surface included within the tube is given by the following, volume integral over some set of points (denoted by *V*) that contain the flame surface patch,

$$A_L(s,y,0,t) = \int_V dV(s,y,0)\left\{H(\pm d_1)H(\pm d_2)H(\pm d_3)H(\pm d_4)\right\}\delta\left(G(s,y,0,t)\right)\left|\nabla G\right| \tag{3.15}$$

where, $H(\bullet)$ is the Heaviside function and $\delta(\bullet)$ is the Dirac-delta function. The signs of the arguments of $H(\bullet)$ are chosen such that the value of this term is unity for all points that lie within the sub-volume of *V* included within the tube. In the present work the above integral is evaluated numerically to first order in grid size (Δx) using numerical approximations for the Heaviside function (Osher and Fedkiw [37]) and the delta function (Smereka [45]). Note, that when defined in this manner, it is not necessary for the point at which the integral in eq. (3.15) is defined to be a lattice point on the computational grid.

The discussion of results obtained from computations described in this chapter will be deferred to later chapters. Insight into the nature of these results can be obtained from a theoretical linearized analysis in terms of turbulence intensity. This theoretical analysis will be presented in the next chapter.

Chapter 4

Flame surface kinematics – Analytical formulation

The goal of this chapter is to describes a perturbation analysis of the G-equation in order to understand, the characteristics of flame surface motions using the technique of asymptotic expansions. The analysis developed here shows that flame surface motions have a non-local dependence on the turbulent velocity field. In other words, the characteristics of flame surface wrinkling at any spatial location depend on velocity fluctuations interacting with the flame surface at other spatial locations on the flame surface as well. This is because of the presence of a mean tangential velocity along the flame brush in the case of attached flames. Space–time correlation functions of flame surface slope fluctuations that will be used to show this point in the next chapter are derived here. Next, the concept of local consumption speed is discussed. A closed form expression for local consumption speed to leading order in turbulence intensity is derived from the present theoretical analysis. Kinematic processes that cause spatial variation in the value of the local consumption speed with increasing distance from the flame holder are discussed.

The rest of this chapter is organized as follows. The section titled "Theoretical formulation" derives a kinematic governing equation for the flame surface shape from the G-equation (eq. (2.3)). This equation is then solved using the technique of asymptotic expansions to for a nominally two-dimensional V-flame stabilized on a prismatic center-body to determine the characteristics of flame response to leading order. Space-time correlation functions of flame surface slope are derived in the next section titled "Slope

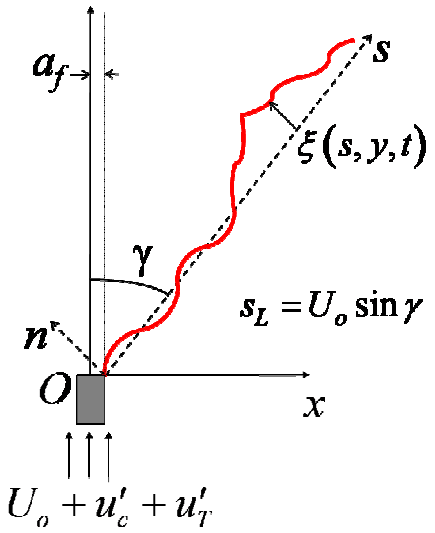

Figure 4-1: Schematic of investigated geometry – one half bluff-body flame stabilized on a prismatic flame holder. Shown are two – possible co-ordinate systems, burner fixed (*x*-*y*-*z*) and flame-fixed (*s*-*y*-*n*). The *y*-axis is directed perpendicularly into the page.

correlations". The section titled "Local consumption speed" presents a closed form expression for the local consumption speed derived from the asymptotic analysis.

4.1 Theoretical Formulation

The investigated geometry is a V-flame stabilized on a prismatic flame-holder, as illustrated schematically in fig. 4-1. The flame is stabilized in an upstream flow of mean velocity U_o superposed with turbulence fluctuations of root mean square (RMS) value u_T'. The flame-holder is assumed to have a width a_f. The principal simplifying assumptions made in this analysis were discussed in the previous chapter.

Figure 4-1 also shows two possible co-ordinate systems for analyzing the flame surface response.

1. The *s*-*y*-*n* system, attached to the nominal flame surface, i.e. the flame surface shape in the absence of turbulence. This will hereafter be referred to as the "flame-fixed" system.

2. The *x-y-z* system, referred to as the bluff-body fixed system henceforth.

The flame surface position in the flame-fixed system is denoted by $\xi(s, y, t)$ (see fig. 4-1). The G-equation (eq.(2.3)) can be written in the flame-fixed co-ordinate system as,

$$\frac{\partial G}{\partial t} + u_s \frac{\partial G}{\partial s} + u_n \frac{\partial G}{\partial n} + v \frac{\partial G}{\partial y} = s_L \sqrt{\left(\frac{\partial G}{\partial s}\right)^2 + \left(\frac{\partial G}{\partial n}\right)^2 + \left(\frac{\partial G}{\partial y}\right)^2} \tag{4.1}$$

Where, u_s, u_n and v denote components along the *s*, *n* and *y* directions respectively. It is possible to define a function that satisfies the properties for *G* as follows,

$$G(s, y, n, t) = n - \xi(s, y, t) \tag{4.2}$$

The above form for *G* assumes that the flame surface can be expressed as a single valued function of the spatial co-ordinates. This is only true at low turbulence intensities. Inserting eq. (4.2) into eq. (4.1) yields an equation for the flame surface shape $\xi(s, y, t)$ as follows,

$$\frac{\partial \xi}{\partial t} + u_s \frac{\partial \xi}{\partial s} + v \frac{\partial \xi}{\partial y} - u_n = -s_L \sqrt{1 + \left(\frac{\partial \xi}{\partial s}\right)^2 + \left(\frac{\partial \xi}{\partial y}\right)^2} \tag{4.3}$$

Equation (4.3) can be rewritten in terms of the following non-dimensional parameters: $s^* = s/L_{11}$, $\xi^* = \xi/L_{11}$, $(u_s^*, v^*, u_n^*) = (u_s, v, u_n)/U_o$ where, L_{11} is the longitudinal integral length scale of the flow perturbations. Together with the constant laminar flame speed assumption (assumption 2), this non-dimensionalization scheme yields the following[3],

[3] Note from fig. 4-1 and assumption 2 it follows that, $s_L/U_o = \sin\gamma$.

$$\frac{\partial \xi}{\partial t} + u_s \frac{\partial \xi}{\partial s} + v \frac{\partial \xi}{\partial y} - u_n = -\sin\gamma \sqrt{1 + \left(\frac{\partial \xi}{\partial s}\right)^2 + \left(\frac{\partial \xi}{\partial y}\right)^2} \tag{4.4}$$

The asterisks have been omitted for notational convenience. All equations will be presented in terms of non-dimensional quantities hereafter unless otherwise specified. The nominal angle the flame makes with the upstream mean flow direction specifies the laminar flame speed s_L (see fig. 4-1). Thus, assuming spatially isotropic and stationary turbulence fluctuations, the normalized velocity field may now be written as follows,

$$\begin{aligned} u_s(s, y, \xi, t) &= \cos\gamma + \varepsilon_T f_s(s, y, \xi, t) \\ u_n(x, y, \zeta, t) &= \sin\gamma + \varepsilon_T f_n(s, y, \xi, t) \\ v(x, y, \zeta, t) &= \varepsilon_T f_v(s, y, \xi, t) \end{aligned} \tag{4.5}$$

Where, ε_T is the root mean squared turbulence velocity (u') normalized by the mean velocity U_o. The functions f_s etc. in the above are random shape functions of their arguments with zero mean and unity variance (in a point-wise sense) and reflect the spatio-temporal structure of the turbulence fluctuations. The constant terms in the above represent the components of the mean velocity normalized by U_o along the respective co-ordinate axes. Next, $\xi(s, y, t)$ can be written as a series expansion in terms of ε_T as follows,

$$\xi(s, y, t) = \xi_o(s, y) + \varepsilon_T \xi_{1t}(x, y, t) + \varepsilon_T^2 \xi_{2t}(x, y, t) + O(\varepsilon_T^3) \tag{4.6}$$

The first term on the RHS of the above represents the shape of the flame in the absence of turbulence fluctuations, i.e. the nominal flame shape. Using the above in eq. (4.4) together with eq. (4.5) yields the following system of equations,

$$\xi_o(s, y, t) = 0 \tag{4.7}$$

$$\frac{\partial \xi_{1t}}{\partial t} + \cos\gamma \frac{\partial \xi_{1t}}{\partial s} = f_n\left(s, y, 0, t\right) \tag{4.8}$$

$$\frac{\partial \xi_{2t}}{\partial t} + \cos\gamma \frac{\partial \xi_{2t}}{\partial s} = -f_v\left(s, y, 0, t\right)\frac{\partial \xi_{1t}}{\partial y} - f_s\left(s, y, 0, t\right)\frac{\partial \xi_{1t}}{\partial s} + \xi_{1t}\left(s, y, t\right) f_{n,n}\left(s, y, 0, t\right) - \frac{\sin\gamma}{2}\left(\left(\frac{\partial \xi_{1t}}{\partial s}\right)^2 + \left(\frac{\partial \xi_{1t}}{\partial y}\right)^2\right) \tag{4.9}$$

Since the flame is attached to the flame-holder at all times (assumption 3) we have from the expansion in eq. (4.6), the following system of boundary conditions,

$$\xi_i\left(0, t\right) = 0 \tag{4.10}$$

Where, the LHS represents the coefficients in the expansion in eq. (4.6). The solutions to eqs. (4.8)-(4.10) yield the shape of the flame up to $O\left(\varepsilon_T^2\right)$. Before proceeding to solve the above equations, several general conclusions on the nature of flame surface motions may be drawn from their basic form. Consider first eq. (4.8). The source term on the RHS of this equation is given by the component of turbulence fluctuations along the direction normal to the flame surface. This means that flame surface wrinkling arises due to velocity perturbations along the direction locally *normal* to the flame surface. Further, the LHS of the equation has the form of a 1-D advection equation defined along the nominal-flame surface. The advection velocity is given by the mean tangential flow velocity component along the flame surface. Consequently, flame surface perturbations generated at any location advect downstream along the flame surface. Therefore, the *net* flame surface perturbation at any given point is a superposition of flame surface perturbations from points upstream at previous times, in addition to those generated locally by flow perturbations. Hence, it is clear that the net response of the flame surface at any point is non-local in nature i.e. it depends on the velocity perturbations at all points "upstream" of

the given point as can be seen from the solution of eq. (4.8) together with the boundary condition in eq. (4.10) as follows,

$$\xi_{1t}(s,y,t)=\frac{1}{\cos\gamma}\int_0^s d\eta_1\ f_n\left(\eta_1,y,0,t-\frac{(s-\eta_1)}{\cos\gamma}\right) \tag{4.11}$$

This phenomenon will henceforth be referred to as 'non-locality'. It is important to note that non-local response is seen only along the directions with non-zero mean velocity.

The second order contribution to the flame surface shape is given by eq. (4.9). Clearly, this equation has the same advection equation type form as eq. (4.8). Also, the source terms on the RHS can be seen to depend on the solution at lower orders. Hence, it is clear that the solution at the second order has a non-local dependence on the velocity field as well. Thus, reasoning inductively it is clear that contributions at all higher orders and hence, the total flame response, have a non-local dependence on the velocity field as well.

Differentiating eq. (4.11) *w. r. t. s* yields,

$$\frac{\partial\xi_{1t}}{\partial s}(s,y,t)=\frac{1}{\cos\gamma}f_n(s,y,0,t)-\frac{1}{\cos^2\gamma}\int_0^s d\eta_1\ \left.\frac{\partial f_n(\eta_1,y,0,\tau)}{\partial\tau}\right|_{\tau=t-\frac{(s-\eta_1)}{\cos\gamma}} \tag{4.12}$$

The first term on the RHS of the above represents the contribution to the flame surface slope due to the local turbulent velocity fluctuation. The second term represents the contribution due to non-locality on the flame surface slope. It will be shown in the forthcoming section that local burning area fluctuations (and hence local consumption speed) are a function of local flame surface slope fluctuations. Hence, eq. (4.12) suggests that local burning area fluctuations must be correlated over space and time due to non-locality. Evaluation of the space time correlation of local burning area from the leading

order flame response theory derived previously is not possible because this requires knowledge of higher order correlations (greater than second order) of the turbulence field. However, since the local burning area is a function of local flame surface slope, the correlation time and length scales of the flame surface slope are the same as the correlation length and time scales of local burning area fluctuations. Therefore, the space-time correlation functions for flame surface slope will be derived next.

4.2 Slope correlations

The correlation function of the leading order flame surface slope along the *s*-direction can be written as follows,

$$R^{NL}_{\xi'\xi'}\left(s,\sigma_s,\sigma_y,\tau\right)=\frac{\left\langle\left(\partial\xi_{1t}/\partial s\right)\big|_{s,y,t}\left(\partial\xi_{1t}/\partial s\right)\big|_{s+\sigma_s,y+\sigma_y,t+\tau}\right\rangle}{\left\langle\left(\partial\xi_{1t}/\partial s\right)^2\right\rangle^{1/2}\Big|_{s,y,t}\left\langle\left(\partial\xi_{1t}/\partial s\right)^2\right\rangle^{1/2}\Big|_{s+\sigma_s,y+\sigma_y,t}} \tag{4.13}$$

Where, the argument *s* on the LHS is the distance of the flame surface location (along the *s*-axis) of the point of interest from the flame holder. The above can be evaluated in terms of the transverse velocity correlation function (R_{22}) using the solution for the leading order flame surface slope. Thus, the superscript '*NL*' in $R^{NL}_{\xi'\xi'}$ denotes the fact that the above correlation is evaluated using the full non-local linear theory. The explicit expression for the above in terms of R_{22} is given in appendix B. $R^{NL}_{\xi'\xi'}$ depends on *s*, i.e. the distance of the reference point of the correlation from the flame-holder. Therefore $R^{NL}_{\xi'\xi'}$ is not spatially stationary *even though* the turbulent fluctuations are both isotropic and

stationary. The above correlation function will be referred to as the "*Non-local*" slope correlation.

It will also be useful to derive an equivalent correlation function of the flame surface slope that describes flame response when non-locality effects are neglected. This was done by neglecting the advection term in the kinematic equation for the linear contribution to the flame surface wrinkling (eq. (4.8) from chapter 2) yields the following,

$$\frac{\partial \xi_{1t}^{L}}{\partial t} = f_n\left(s, y, 0, t\right) \tag{4.14}$$

where, the superscript '*L*' represents a local response solution. The above equation implies that the local flame surface perturbation is purely a function of the local turbulent velocity fluctuations[4]. The attachment boundary condition is a spatial boundary condition that cannot be enforced in this case. This implies that the flame attachment mechanism cannot influence flame surface motions at locations away from the flame holder. This is an important difference between the local and non-local response cases and will be discussed later in the context of local consumption speed. For the present, eq. (4.14) yields the following expression for the local flame surface slope in terms of the Fourier transform w. r. t. *s, y* and *t* (denoted by $\hat{f}_n$),

$$\frac{\partial \xi_{1t}^{L}\left(s, y, t\right)}{\partial s} = \int_{-\infty}^{\infty} dk_s dk_y d\omega \left(\frac{k_s}{\omega}\right) \hat{f}_n\left(k_s, k_y, 0, t\right) e^{-i\left(k_s s + k_y y + \omega t\right)} \tag{4.15}$$

[4] Equation (4.14) is identical to the kinematic equation used in the analysis of Aldredge [46].

Since the turbulence field is assumed to be spatially isotropic and stationary in time, the equivalent local correlation function for the flame surface slope from the above local theory can be determined in terms of R_{22}, using the Wiener-Khinchin theorem, as the following (see appendix B for details),

$$R^{L}_{\xi'\xi'}\left(\sigma_s,\sigma_y,\tau\right)=\frac{\int_{-\infty}^{\infty}d\tau'\,|\tau'|\left.\frac{\partial^2 R_{22}\left(\sigma'_s,\sigma'_y,\tau''\right)}{\partial\sigma'^2_s}\right|_{\sigma'_s=\sigma_s,\sigma'_y=\sigma_y,\tau''=\tau'+\tau}}{\int_{-\infty}^{\infty}d\tau'\,|\tau'|\left.\frac{\partial^2 R_{22}\left(\sigma'_s,\sigma'_y,\tau'\right)}{\partial\sigma'^2_s}\right|_{\sigma'_s=0,\sigma'_y=0,\tau''=\tau'}} \qquad (4.16)$$

The above will be referred to as the "*Local*" slope correlation function in the discussion presented below. The above expression is independent of the origin of the correlation due to the absence of wrinkle advection i.e. non-locality. It must be noted that the correlation length scale of velocity fluctuations along the flame surface is the same for eqs. (4.13) and (4.16). The key difference is the absence of non-locality effects in the latter.

The local heat release rate is a function of the ensemble averaged increase in local burning area due to flame surface wrinkling. This increase in burning rate is quantified using the concept of consumption speed. In the next section, this concept will first be defined in general and then an explicit expression for the consumption speed for the current flame configuration will be derived.

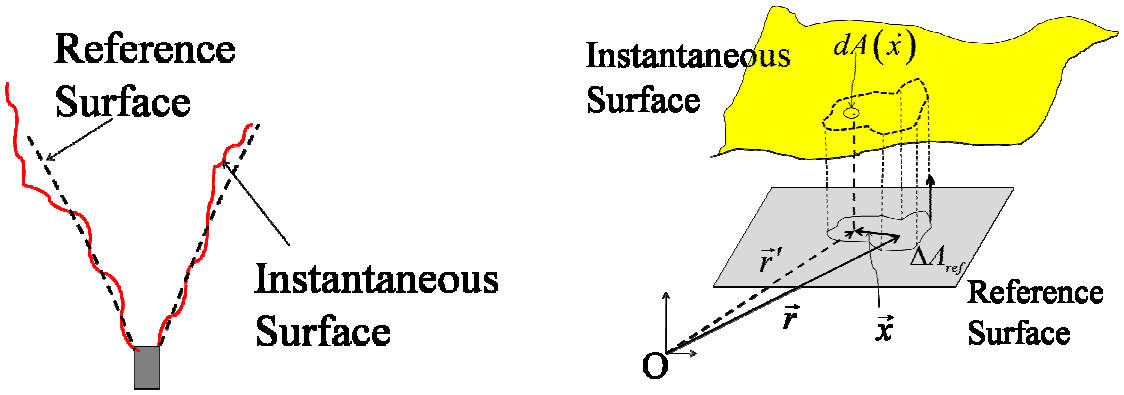

(a) **(b)**

Figure 4-2: Schematic representation of the turbulent flame showing (a) the reference surface and (b) a schematic representation of the surface patch used to define consumption speed.

4.3 Local Consumption speed

As discussed in chapter 1, it is possible to associate with the ensemble of flamelets comprising the turbulent flame brush, a reference surface[5] (e.g. 0.5 mean progress variable contour etc.). Figure 4-2(a) schematically shows such a surface together with an instantaneous snapshot of the flame surface. Consider a patch ΔA_{ref} on this reference surface whose location in space is given by the position vector $\vec{r}$ of some arbitrarily chosen point within this patch, relative to some appropriately chosen origin (see the schematic in fig. 4-2(b)). Any point in this patch can now be referenced by its position vector $\vec{x}$ relative to $\vec{r}$. Thus, the patch ΔA_{ref} may then be defined as the set with these position vectors $\vec{x}$, as individual elements. The overall

contribution to the net ensemble averaged heat release rate of the flame from ΔA_{ref} is given by the following integral (dimensional form, see also Figure 4-2(b)),

---

[5] This surface may be defined using the progress variable or by some other averaging technique in practice. However, the *definition* of consumption speed does not depend on how this surface is defined.

$$\left\langle q\left(\Delta A_{\text{ref}}\right)\right\rangle = \int_{\vec{x}\in\Delta A_{\text{ref}}} \left\langle dA\left(\vec{x}\right)\rho h_R s_L\right\rangle \tag{4.17}$$

Where, ρ and h_R denote the upstream unburnt gas density and the heat of reaction of the unburnt mixture respectively. The angle brackets in the above (and hereafter) denote the ensemble averaging operation. The consumption speed associated with the patch ΔA_{ref} is defined as the following,

$$\left\langle q\left(\Delta A_{\text{ref}}\right)\right\rangle = S_{T,C}\left(\Delta A_{\text{ref}}\right) \int_{\vec{x}\in\Delta A_{\text{ref}}} dA_{\text{ref}}\left(\vec{x}\right)\rho h_R \tag{4.18}$$

Thus, eqs. (4.17) and (4.18) yield,

$$S_{T,C}\left(\Delta A_{\text{ref}}\right) = \frac{\int_{\vec{x}\in\Delta A_{\text{ref}}} \left\langle dA\left(\vec{x}\right)\rho h_R s_L\right\rangle}{\int_{\vec{x}\in\Delta A_{\text{ref}}} dA_{\text{ref}}\left(\vec{x}\right)\rho h_R} \tag{4.19}$$

Now, if ΔA_{ref} is taken to be the entire area of the reference flame surface (i.e. $\Delta A_{\text{ref}} \equiv A_{\text{ref}}$), the above expression becomes the definition of the "Global" consumption speed of the flame as follows,

$$S_{T,GC}\left(A_{\text{ref}}\right) = \frac{\int_{\vec{x}\in A_{\text{ref}}} \left\langle dA\left(\vec{x}\right)\rho h_R s_L\right\rangle}{\int_{\vec{x}\in A_{\text{ref}}} dA_{\text{ref}}\left(\vec{x}\right)\rho h_R} \tag{4.20}$$

Hence, it is clear from the above expression that global consumption speed describes the overall mass burning rate of the flame. Further, a "local" consumption speed as the following limit of the definition in eq. (4.19).

$$S_{T,LC}\left(\vec{r}\right)=\lim_{|\Delta A_{\text{ref}}|\to 0}\frac{\int_{\vec{x}\in\Delta A_{\text{ref}}}\left\langle dA\left(\vec{x}\right)\rho h_R s_L\right\rangle}{\int_{\vec{x}\in\Delta A_{\text{ref}}} dA_{\text{ref}}\left(\vec{x}\right)\rho h_R} \tag{4.21}$$

Where, the notation, $\left|\Delta A_{\text{ref}}\right|$ denotes the area of the patch. Clearly, the above is a quantity that is defined at every point of the reference flame surface and may be interpreted as the local heat release rate normalized by the flow rate of net reactant enthalpy per unit volume through the reference area. Thus, the quantitative value of the local consumption speed depends on the choice of this reference surface as well as the flow features and thermo-chemical properties of the reactant mixture.

All of the above definitions are valid in general for turbulent premixed flames or partially premixed flames. The latter occur when there are spatio-temporal variations in the upstream unburnt gas equivalence ratio. However, the present work limits itself to the perfectly premixed case. As such, assuming that the perfectly premixed reactants, constant flame speed and that there are no density variations in the upstream flow, the local consumption speed from eq. (4.21) can be written as,

$$\frac{S_{T,LC}\left(\vec{r}\right)}{s_L}=\lim_{|\Delta A_{\text{ref}}|\to 0}\frac{\int_{\vec{x}\in\Delta A_{\text{ref}}}\left\langle dA\left(\vec{x}\right)\right\rangle}{\left|\Delta A_{\text{ref}}\right|} \tag{4.22}$$

Now, returning to the analysis in the present work the reference area is chosen to be a patch for a with dimensions Δs and Δy along *s*- and *y*- directions respectively centered around the point (*s*, *y*) on the nominal flame surface. The integral in the numerator of the above is taken to be the flame surface area included within a rectangular tube whose cross-section is the reference area and with the axis perpendicular to the nominal flame

surface. Assuming a single valued flame surface, the above expression can be written as the following,

$$\frac{S_{T,LC}(s,y)}{s_L} = \lim_{\substack{\Delta s\to 0\\ \Delta y\to 0}} \frac{1}{\Delta s \Delta y} \int_{y-\frac{\Delta y}{2}}^{y+\frac{\Delta y}{2}} \int_{s-\frac{\Delta s}{2}}^{s+\frac{\Delta s}{2}} ds dy \left\langle \sqrt{1+\left(\frac{\partial \xi}{\partial s}\right)^2 + \left(\frac{\partial \xi}{\partial y}\right)^2} \right\rangle \tag{4.23}$$

The above limit yields an expression for $S_{T,LC}$ as,

$$\frac{S_{T,LC}(s,y)}{s_L} = \left\langle \sqrt{1+\left(\frac{\partial \xi}{\partial s}\right)^2 + \left(\frac{\partial \xi}{\partial y}\right)^2} \right\rangle \tag{4.24}$$

This expression is valid in general as long as the flame surface is not multi-valued in the *s-y-n* co-ordinate system. Further, using the expansion (eq. (4.6)) in the above yields,

$$\frac{S_{T,LC}(s,y)}{s_L} = 1 + \frac{1}{2}\left\{ \left\langle \left(\frac{\partial \xi_{1t}}{\partial s}\right)^2 \right\rangle + \left\langle \left(\frac{\partial \xi_{1t}}{\partial y}\right)^2 \right\rangle \right\} \varepsilon_T^2 + O\left(\varepsilon_T^3\right) \tag{4.25}$$

Thus, in order to determine the leading order spatial variation of local consumption speed, it is enough to evaluate the mean squared flame surface slope by ensemble averaging eq. (4.12). The final results are presented in terms of the correlation function of velocity fluctuations, $R_{22}(\sigma_s, \sigma_y, \tau)$ as (see appendix C for details):

$$\left\langle \left(\frac{\partial \xi_{1t}}{\partial s}\right)^2 \right\rangle = \frac{1}{\cos^2\gamma} \left[\begin{array}{l} 1 - \dfrac{1}{\cos^2\gamma} \displaystyle\int_{-s}^{s} d\sigma_s \left(s - |\sigma_s|\right) \left. \dfrac{\partial^2 R_{22}(\sigma_s, \sigma_y, \tau)}{\partial \tau^2} \right|_{\sigma_y = 0, \tau = \frac{\sigma_s}{\cos\gamma}} \\ + \dfrac{2}{\cos\gamma} \displaystyle\int_{0}^{s} d\sigma_s \left. \dfrac{\partial R_{22}(\sigma_s, \sigma_y, \tau)}{\partial \tau} \right|_{\sigma_y = 0, \tau = \frac{\sigma_s}{\cos\gamma}} \end{array} \right]$$

$$\left\langle \left(\frac{\partial \xi_{1t}}{\partial y}\right)^2 \right\rangle = -\frac{1}{\cos^2\gamma} \int_0^s \int_0^s d\sigma_1 d\sigma_2 \left. \frac{\partial^2 R_{22}(\sigma_s, \sigma_y, \tau)}{\partial \sigma_y^2} \right|_{\sigma_s = \sigma_1 - \sigma_2, \sigma_y = 0, \tau = \frac{\sigma_s}{\cos\gamma}} \tag{4.27}$$

Finally, since $\varepsilon_T = \left(u'/s_L\right)\sin\gamma$, eq. (4.25) together with the above expressions yields,

$$\frac{S_c(s)}{s_L} = 1+\frac{\tan^2\gamma}{2}\left\{\begin{array}{l} 1-\dfrac{1}{\cos^2\gamma}\displaystyle\int_{-s}^{s} d\sigma\,\left(s-|\sigma|\right)\frac{\partial^2 R_{22}\left(\sigma_s,\sigma_y,\tau\right)}{\partial\tau^2}\Bigg|_{\substack{\sigma_s=\sigma,\\ \sigma_y=0,\\ \tau=\frac{\sigma}{\cos\gamma}}} \\ +\dfrac{2}{\cos\gamma}\displaystyle\int_{0}^{s} d\sigma\,\frac{\partial R_{22}\left(\sigma_s,\sigma_y,\tau\right)}{\partial\tau}\Bigg|_{\substack{\sigma_s=\sigma,\\ \sigma_y=0,\\ \tau=\frac{\sigma}{\cos\gamma}}} \\ -\displaystyle\int_{0}^{s}\int_{0}^{s} d\sigma_1 d\sigma_2\,\frac{\partial R_{22}\left(\sigma_s,\sigma_y,\tau\right)}{\partial\sigma_y^2}\Bigg|_{\sigma_s=\sigma_1-\sigma_2,\sigma_y=0,\tau=\frac{\sigma_s}{\cos\gamma}} \end{array}\right\}\left(\frac{u'}{s_L}\right)^2 + O\left(\varepsilon_T^3\right) \tag{4.28}$$

The above expression shows that the leading order contribution to the consumption speed is completely characterized by the transverse correlation function, the turbulence intensity and the mean flow component tangential along the s-axis. Note that the above result is valid for any homogenous, isotropic and stationary turbulence field. Note also that eq. (4.28) is a function of spatial location (i.e *s* = distance from the flame-holder). The reasons for this are discussed below.

The net instantaneous flame surface slope at any point on the flame surface is a superposition between two wrinkling 'waves' (ref. Preetham et al. [30]). The first of these arises because of spatial variations in velocity fluctuation along the flame surface and the second is generated by flame attachment. This can be shown as follows. Differentiating eq. (4.8) w. r. t. *s* yields,

$$\frac{\partial}{\partial t}\left(\frac{\partial\xi_{1t}}{\partial s}\right)+\cos\gamma\frac{\partial}{\partial s}\left(\frac{\partial\xi_{1t}}{\partial s}\right)=\frac{\partial f_n\left(s,y,0,t\right)}{\partial s} \tag{4.29}$$

Assuming that the flame is always attached at the base, eq. (4.8) yields the following boundary condition,

$$\left.\frac{\partial \xi_{1t}}{\partial s}\right|_{s=0} = \frac{f_n\left(s=0, y, 0, t\right)}{\cos\gamma} \tag{4.30}$$

Thus, eqs. (4.29) and (4.30) yield the following solution.

$$\frac{\partial \xi_{1t}\left(s, y, 0, t\right)}{\partial s} = \frac{1}{\cos\gamma}\int_0^s ds' \left.\frac{\partial f_n\left(s'', y, 0, t'\right)}{\partial s''}\right|_{s''=s', t'=t-\frac{s-s'}{\cos\gamma}} + \frac{f_n\left(s=0, y, 0, t-\left(s/\cos\gamma\right)\right)}{\cos\gamma} \tag{4.31}$$

The above is an alternative way of decomposing flame surface slope. The first term on the RHS arises from spatial non-uniformities of the turbulence fluctuations and is just the particular integral of eq. (4.29). It has the above form because of the presence of a tangential advection term (second term on the LHS of eq.(4.29)) and includes all local and non-local components except for the contribution from the point at the flame holder. The second term arises due to the flame attachment boundary condition (eq. (4.30)) and is the homogeneous solution of eq. (4.31) and represents the non-local contribution due to the presence of flame attachment. Thus, the net mean squared slope (and hence the local consumption speed) is a resultant of the interference between the boundary wave and non-local flame surface perturbations due to velocity fluctuations. This means that the mode of flame attachment fundamentally influences the overall characteristics of the flame. A similar analysis can be performed for the derivative in the transverse direction by taking the derivative of eq. (4.8) *w. r. t. y* and proceeding as above.

It is useful to consider the prior analysis of local consumption speed for a freely propagating nominally flat flame (i.e. $U_o = s_L$) in an upstream turbulent flow of reactants

due to Aldredge [46]. The kinematic equation derived in this work is identical to eq. (4.14). An expression for the local consumption speed can be derived from eq. (4.14) as follows [46],

$$\frac{S_{T,LC}}{s_L} = 1 + \varepsilon_T^2 \int_{-\infty}^{\infty} d\sigma_s d\sigma_y d\tau \left\{ R_{22}\left(\sigma_s, \sigma_y, \tau\right) \int_{-\infty}^{\infty} dk_s dk_y d\omega \left(\frac{k_s^2 + k_y^2}{2\omega^2} \right) e^{-i\left(k_s\sigma_s + k_y\sigma_y + \omega\tau\right)} \right\} \tag{4.32}$$

Evaluating the inner integral as its principal value yields,

$$\frac{S_{T,LC}}{s_L} = 1 + \frac{1}{2}\left(\frac{u'}{s_L}\right)^2 \int_{-\infty}^{\infty} d\tau \, |\tau| \left\{ -\frac{\partial^2 R_{22}\left(\sigma_s, \sigma_y, \tau\right)}{\partial \sigma_s^2} - \frac{\partial^2 R_{22}\left(\sigma_s, \sigma_y, \tau\right)}{\partial \sigma_y^2} \right\} \Bigg|_{\sigma_s = \sigma_y = 0} \tag{4.33}$$

The expression in eq. (4.28) differs from the above result for a freely propagating flat flame in two ways. First, because of the absence of non-locality, eq. (4.14) does not have a tangential advection term. Second, there is no flame attachment in the case of a freely propagating flame. From the previous discussion on the effect of the attachment boundary condition, a change in the mode of flame attachment alone can cause the flame surface slope and hence local burning area at downstream locations to change. Hence, this causes the spatial distribution of consumption speed distribution to change even if the characteristics of the turbulence fluctuations themselves remain unchanged.

Next, to gain further insight into the quantitative nature of flame response to turbulence fluctuations from the present analysis, the space-time correlation function, $R_{22}\left(\sigma_s, \sigma_y, \tau\right)$, needs to be specified. This may be done in several ways such as, from DNS studies or from experimental data. However, as discussed in the previous

chapter, in the limit of low-intensity large length scale turbulence the spatial variation of the longitudinal spatial correlation function is Gaussian (Hinze [43]). Therefore, assuming mass conservation and Taylor's hypothesis together with the longitudinal spatial correlation function specified in the previous chapter (eq. (3.13)), the two-point *space-time* correlation of turbulent velocity fluctuations in the direction normal to the nominal flame surface is derived in Appendix E. Such two-point two-time correlation functions have been used in previous analyses of consumption speed (Aldredge and Williams [44]). Thus eq. (4.28) may be integrated using standard results (Gradshteyn and Rhyzik [47]) to yield,

$$\frac{S_{T,LC}(s)}{s_L} = 1 + 4\left\{\left(e^{-\frac{\pi}{4}s^2\tan^2\gamma} - 1\right) + \pi s\tan\gamma\,\Phi\left(\frac{s\sqrt{\pi}}{2}\tan\gamma\right) + \frac{\tan^2\gamma}{8}\right\}\left(\frac{u'}{s_L}\right)^2 \tag{4.34}$$

Where, the function $\Phi(\bullet)$ is the error function defined as below,

$$\Phi(x) = \frac{1}{\sqrt{\pi}}\int_0^x dx' e^{-x'^2} \tag{4.35}$$

Equation (4.34) represents a key result of the analysis presented in this section. To reitierate, even though the turbulent velocity field has been assumed to be *isotropic* and *stationary*, the local consumption speed varies *spatially* due to the influence of non-locality and the flame attachment boundary condition. Equation (4.34) can also be written in terms of a characteristic length scale over which turbulent eddies interact with the flame. This length scale can be determined as follows.

The assumption of Taylor's hypothesis implies that, the time taken for a turbulent eddy of length scale l to cross the flame surface is given by $l/(U_o\sin\gamma)$ (dimensional

form). The denominator is essentially the mean velocity component normal to the nominal flame surface. In this time interval the eddy interacts with the flame surface over a length equal to $s_{in,local} = U_o \cos\gamma \left(L_{11}/U_o \sin\gamma \right) = L_{11} \cot\gamma \Rightarrow \; s^*_{in,local} = \cot\gamma$. Thus the distance s can now be rescaled using $s^*_{in,local}$ as $s^* = s \tan\gamma$. Hence eq. (4.34) can be rewritten as,

$$\frac{S_{T,LC}\left(s^*,\gamma\right)}{s_L} = 1 + 4\left\{ e^{-\frac{\pi}{4}\left(s^*\right)^2} - 1 + \pi s^* \Phi\left(\frac{s^*\sqrt{\pi}}{2} \right) + \frac{\tan^2\gamma}{8} \right\} \left(\frac{u'}{s_L} \right)^2 \qquad (4.36)$$

Note that even after rescaling s by $s^*_{in,local}$, the last term still remains. This term represents the effect of the boundary condition as shown by the following analysis.

First note that $s^*=0 \Rightarrow s=0$. Further, at the flame-holder, the only contribution to the flame surface wrinkling comes from the boundary condition term in eq. (4.31) (second term on the RHS). Thus, from eq. (4.25), the local consumption speed at the attachment location is given by,

$$\frac{S_{T,LC}\left(s=0\right)}{s_L} = 1 + \frac{1}{2}\left\{ \left\langle \left(f_n\left(s=0,y,0,t\right)\right)^2 \right\rangle \right\} \frac{\varepsilon_T^2}{\cos^2\gamma} \qquad (4.37)$$

Which, for the present isotropic turbulent velocity field becomes,

$$\frac{S_{T,LC}\left(s=0\right)}{s_L} = 1 + \left\{ \frac{1}{2}\tan^2\gamma \right\} \left(\frac{u'}{s_L} \right)^2 \qquad (4.38)$$

The above result can be obtained from eq. (4.36) by setting $s^*=0$ as well proving the desired result. Note that the neither the assumption of isotropy or Taylor's hypothesis was invoked in the derivation of eq. (4.37) and as such is a general result within the purview

of the other assumptions of the present analysis. The term within braces in eq. (4.37) is simply the RMS turbulence velocity fluctuation velocity at the flame attachment location normalized by a mean flow velocity scale. When the attachment location is at a solid boundary such as a flame holder, this fluctuation velocity is very small due to viscous dissipation. Hence, the local consumption speed at the flame holding location reduces to the laminar flame speed. However, since the present analysis neglects dissipative effects on turbulent velocity fluctuations, the local consumption speed at the flame base is different from the laminar flame speed as can be seen from eq. (4.38).

Note that there is no scaling by which eq. (4.36) may be rendered independent of γ due to the impact that the mode of flame attachment has on flame surface motions downstream of the flame holder due to non-locality. Hence, comparisons between experimental measurements of local or global consumption speeds across flame configurations/combustor geometries must ensure that the flame attachment modes in addition to the statistical characteristics of the turbulent flow field are the same across these configurations.

Other limiting cases of eq. (4.34) as follows,

Small γ (Long flame limit):

$$\frac{S_{T,LC}(s)}{s_L} = 1 + 4\left\{\left(e^{-\frac{\pi}{4}(s\gamma)^2} - 1\right) + \pi(s\gamma)\Phi\left(\frac{(s\gamma)\sqrt{\pi}}{2}\right) + \frac{\gamma^2}{8}\right\}\left(\frac{u'}{s_L}\right)^2 \qquad (4.39)$$

For sufficiently small $s\gamma$ the above can be rewritten as,

$$\frac{S_{T,LC}(s)}{s_L} = 1 + \frac{\gamma^2}{2}\left\{8\pi s^2 + 1\right\}\left(\frac{u'}{s_L}\right)^2 \qquad (4.40)$$

Thus, the spatial dependence of local consumption speed is quadratic in nature close to the flameholder for long flames. This is true for general γ as well, as can be seen from the following,

Nearfield limit (s $\rightarrow$ 0):

$$\frac{S_{T,LC}(s)}{s_L} = 1 + \frac{\tan^2\gamma}{2}\left\{8\pi s^2 + 1\right\}\left(\frac{u'}{s_L}\right)^2 \tag{4.41}$$

All of the above results are valid only when the flame response is linear. Even with increasing u'/s_L, there is a small region near the flame holder where the flame surface motions are well described by linear flame kinematics. Also, the length of this region decreases as u'/s_L increases. This point among others will be shown in the next chapter that discusses the results developed in this chapter together with computational results. The effect of non-linearity due to flame propagation (Kinematic restoration) will be discussed in detail.

Chapter 5

Flame surface kinematics - Results

This chapter presents results from the theoretical/numerical analyses developed in the previous chapters. The discussion is organized into two sections. The first section discusses non-local characteristics of flame response through a qualitative description of flame surface slope and local burning area correlations. This is followed by a discussion of the spatial characteristics of local consumption speed. The various physical processes that result in the observed spatial variation are discussed in detail. The investigated geometry is shown again in fig. 5-1 for the reader's convenience. The integral length scale (L_{11}) is the only imposed length scale in the present analysis as the flow-field is prescribed rather than solved for. Further, due to Taylor's hypothesis, the characteristic interaction time scale of velocity fluctuations with the flame is given by L_{11}/U_o. Thus, in all computational results presented henceforth, lengths and times are normalized using the above integral length and interaction time scales respectively. The turbulence intensity (u') will be normalized by the laminar flame speed s_L. All computational results presented in this section were performed on a computational grid with grid size, Δx=0.1. Thus, an integral length scale of the generated turbulence fluctuations is resolved over 10 grid points. This was sufficient to ensure grid independence in the spatial distribution of local consumption speed estimated from the computations (see appendix A). The solution was evolved at a constant time step of 0.1 Δx. The nominal flame angle (γ, see fig. 5-1) was chosen to be 4^o for all computations. The initial level-set field was specified as described in chapter 3.

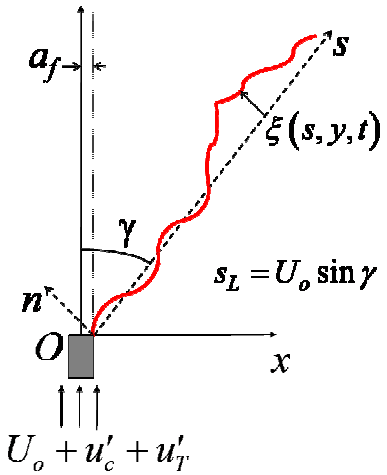

Figure 5-1: Schematic of investigated geometry. Bluff-body flame stabilized on a prismatic flame holder (one half only shown). Also shown are two possible co-ordinate systems for analysis, burner fixed (*x*-*y*-*z*) and flame-fixed (*s*-*y*-*n*). The *y*-axis is directed perpendicularly into the page.

Computational results were obtained at three values of u'/s_L = 0.75, 2.25 and 3.75. The initial conditions for the *G*-field and the turbulent velocity field were specified as described in chapter 4. Sampling time periods corresponding to 7 integral time scales for the u'/s_L = 0.75 and 2.25 cases and 2.2 integral time scales for the u'/s_L =3.75 case were used to sample the solution. For all the computational results presented next, only samples taken after the solution had progressed beyond a time corresponding to one flow-through time from the flame-holder to the exit plane (~fifty integral timescales) were considered in order to ignore the initial transient growth of the flame brush. This delay was sufficient for the time averaged value of the global mean area to reach a statistically stationary limit. All results from computations presented in the forthcoming sections were determined using 400 realizations of local burning area at each spatial location for u'/s_L = 0.75 and 2.25 cases and 1000 realizations for the u'/s_L = 3.75 case.

Figure 5-2a-c shows a typical snapshots of the computed instantaneous flame surface shapes at a normalized time *t*=294 for the three u'/s_L values. Figures 5-2a-b show that the

flame surfaces become more wrinkled with increasing distance from the flame holder in each case, even though, the fluctuating velocity field is isotropic and stationary. Also, the formation of pockets at large distances from the flame holder (z > 30 approx.) is clearly seen in all of the three cases. These can be pockets of reactants surrounded by products (type 1) or vice versa (type 2).

Figures 5-3a-c show the details of flame surface evolution in a vertical section through the flame surface at the mid-point of the flame holder at three time instants separated by a time interval corresponding to τ = 2.2 (u'/s_L =3.75). The arrows show regions of the flame that form pockets of each type. Consider first the evolution of the flame surface feature marked by the arrow labeled '1' in fig. 5-3a. Flame propagation

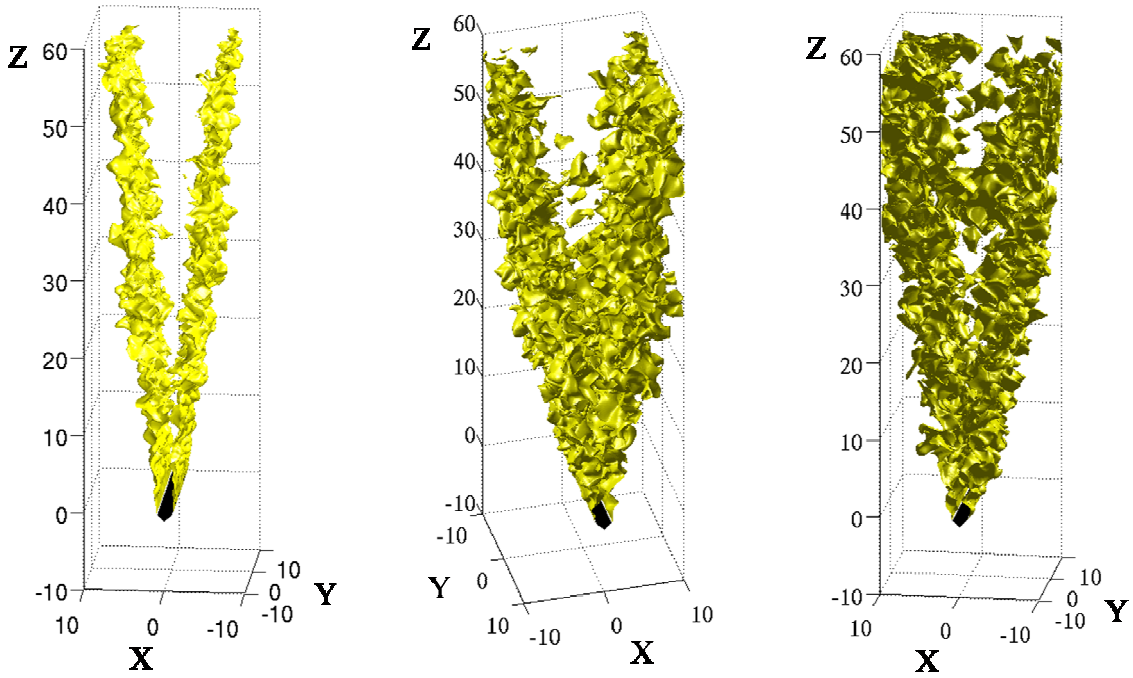

Figure 5-2: Typical snapshot of the instantaneous flame surface (a) u'/s_L = 0.75, (b) u'/s_L = 2.25 and (c) u'/s_L = 3.75. $\gamma \sim 4^o$. Notice that flame surface winkling increases with increasing distance from the flame-holder resulting in pocket formation.

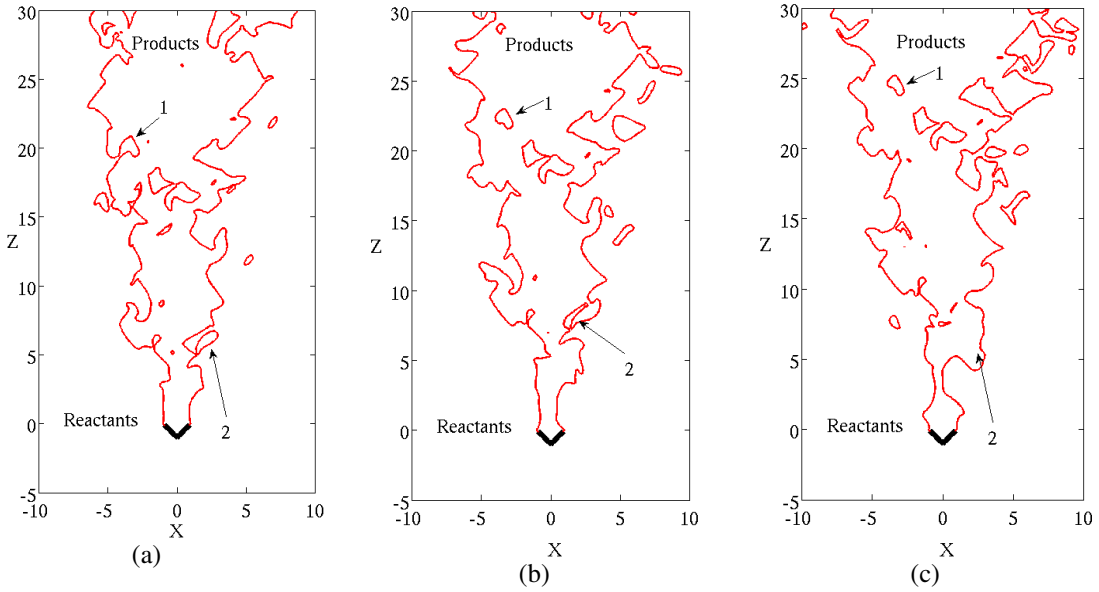

Figure 5-3: Instantaneous snapshots of a vertical section through the flame surface at three successive time instants separated by an interval τ=2.2 (u'/s_L = 3.75. γ ~ 4°). The arrows labeled 1 and 2 tracks the evolution of pockets of type 1 and 2 respectively.

causes a "pinch-off" of a pocket of reactants from the main flame surface as the flame develops. This pocket then travels downstream as it burns out (see figs. 5-3b-c). Consider again the flame surface feature as shown by the arrow labeled '2' in fig. 5-3a. This feature is an example of a type 2 pocket i.e., products surrounded by

reactants. In this case flame propagation causes this pocket to merge with the main flame surface as shown in fig. 5-3b-c. Note that, type 2 pockets are not true pockets but appear because figs. 5-3a-c are two dimensional cuts through a three dimensional instantaneous flame surface. The key point made by figs.5-3a-c is that flame surface features produced at any given location move downstream as they evolve. This is consistent with the non-locality argument made from the theoretical analysis in the previous chapter. The above qualitative behavior was seen for all solutions at the other times as well. Hence, even though the turbulent velocity fluctuations are isotropic and stationary in the present simulations, the qualitative features of the flame surface wrinkling vary spatially. This

behavior is analyzed formally through a correlation analysis of flame surface slope and burning area presented in the next section.

5.1 Correlation analysis

This section describes the non-local nature of flame surface motions fluctuations through a correlation analysis of the flame surface slope and local burning area fluctuations. The key physical phenomenon causing non-local response is the advection of wrinkles by the flow at the mean tangential velocity along the nominal flame surface. Thus, quantities that depend on the characteristics flame surface wrinkling defined at different spatial locations on the flame must be correlated over a time corresponding to the advection time of a wrinkle over the spatial separation distance. This is demonstrated in this section through a series of results from a correlation analysis of flame surface slope (linear limit) derived from the theoretical analysis in chapter 4 and local burning area (non-linear) determined from the computations in chapter 3.

The non-local space time correlation function of the flame surface slope along the nominal flame surface, $R^{NL}_{\xi'\xi'}$, was introduced in the previous chapter (eq. (4.13)). The variation of $R^{NL}_{\xi'\xi'}$ with spatial separation (σ) along the s direction (σ_y =0) for typical values of time interval (τ) at four arbitrarily chosen flame surface locations (given by s) is shown in fig. 5-4. Note that in every case, the peak correlation shift to values of σ corresponding to $\tau \cos\gamma$. This advective characteristic is due to the fact that wrinkles move along the flame surface at the mean tangential flow velocity, $\cos\gamma$, causing the slopes at points spatially separated by σ corresponding to $\tau \cos\gamma$ to become correlated. Also shown is the envelope of the peak correlation values in each case. The width along

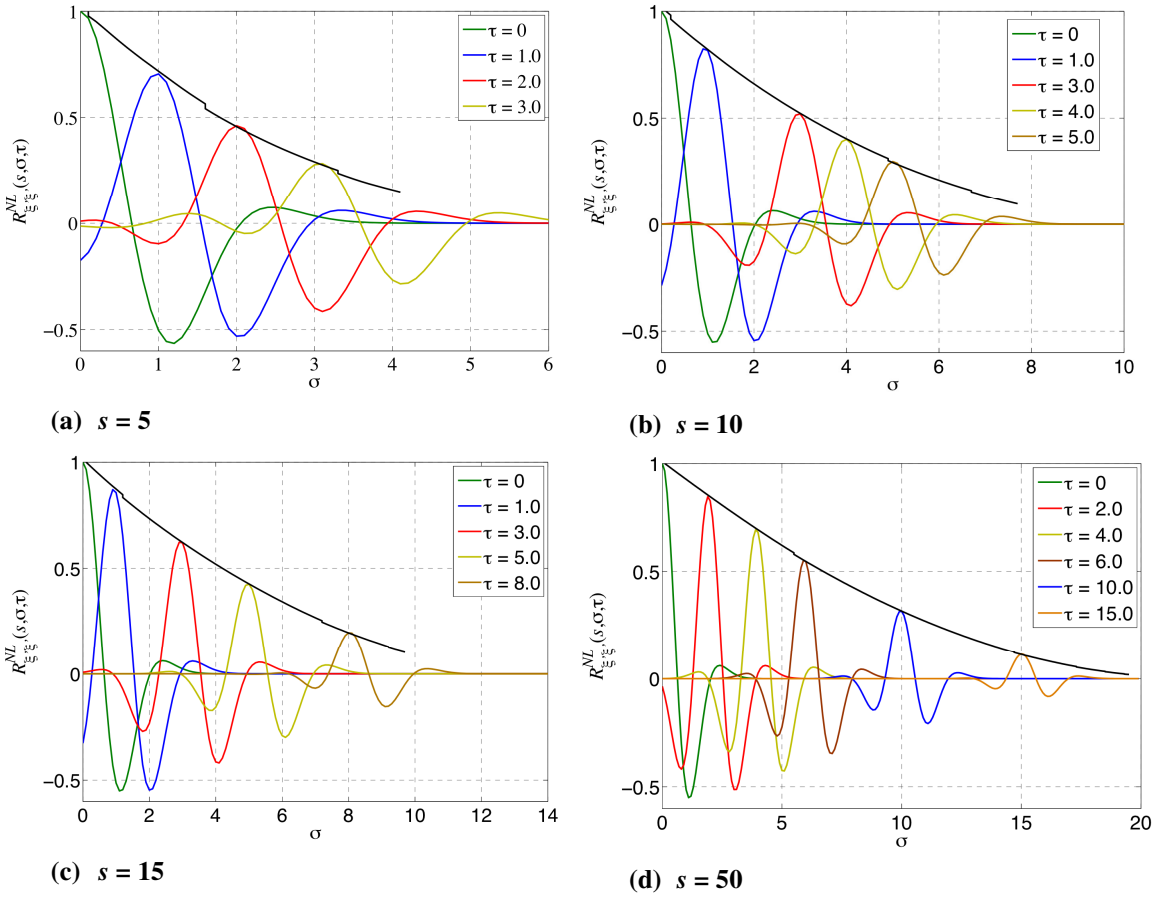

Figure 5-4: Variation of the non-local slope correlation with spatial separation along the *s*-direction at different time intervals as derived using linear Non-local theory at four different spatial locations s = (a) 5 (b) 10 (c) 15 (d) 50. γ ~ 4°). Also shown is the envelope of the maximum correlations at each value of time interval (black curve) for all cases.

the horizontal axis of this envelope denotes the set of points at which the slope fluctuations are maximally correlated with the slope fluctuations at the point referenced by *s* (reference point) eg. the flame surface slope at a distance of *s*=15.0 from the flame holder is significantly correlated with those up to six integral

length scales downstream over time. The decay of these peak values with increasing σ can be explained as follows. First, the correlation drops simply because the velocity perturbations causing slope fluctuations at any two points become increasingly uncorrelated with increasing σ. Secondly, in the linear limit, the net slope at any point

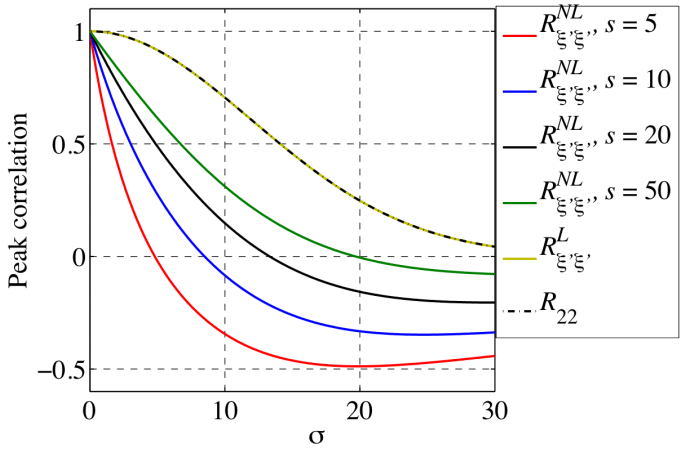

Figure 5-5: Peak correlation envelopes of the local and non-local slope correlations with the correlation envelope of the velocity fluctuations. Flame angle γ~4°.

can be decomposed into a local component due to the local velocity fluctuations and a non-local component which is a result of superposition of flame slope fluctuations from points upstream. The latter contributions are correlated to varying extents with each other depending on where they were first generated. Hence, the correlation between the resultant non-local components at two different flame surface

points drops over time with increasing σ due to a superposition of a large number of varying correlated values. The peak envelopes in fig. 5-4 decay as a result of both of these effects. The importance of the second effect can be appreciated from fig. 5-5 that plots the peak correlation envelopes of the local slope correlation function ($R^{L}_{\xi'\xi'}$) (eq. (4.16)) and the velocity correlation function R_{22} derived in appendix F along with typical envelopes of $R^{NL}_{\xi'\xi'}$. Note that the peak correlation envelope of $R^{L}_{\xi'\xi'}(\sigma,\tau)$ decays at the same rate as that of $R_{22}(\sigma,\tau)$ while the envelopes of $R^{NL}_{\xi'\xi'}(s,\sigma,\tau)$ all decays at a very different rate. The former result is due to the fact that flame surface slope fluctuations in the local case are functions the *local* velocity fluctuations alone. Hence they have to be spatially correlated over the same length and timescales as that of the velocity

fluctuations. Further, with increasing distance from the flame holder, the envelopes of $R^{NL}_{\xi'\xi'}$ begin to move towards the envelope of R_{22}. This is because the non-local components at point that are at large distances from the flame holder are due to superposition of a very large number of uncorrelated contributions. Therefore, the slope correlation due to local velocity disturbances dominates the overall slope correlation between

these points causing the flame response to acquire a more "local" character, resulting in the movement of the envelopes towards that of R_{22} as shown by fig. 5-5. However, there is always a neighbourhood of points from which the contribution to the overall slope correlation function from non-local components at points at large distances from the flame holder are significant. Hence the flame response never really becomes completely "local" in character. As turbulence intensity increases, linear theory cannot be used to determine slope correlations due to the increasing effect of non-linearity on flame surface kinematics. Also, the flame surface becomes multi-valued (in the flame-fixed system) at high turbulence intensities. Hence, computed spatio-temporal correlation estimates for local burning area are presented next.

The spatial distribution of local burning area was evaluated at a 1D grid of points oriented along the *s*-axis at 10 different locations separated by a non-dimensional distance of 2 integral length scales. The grid spacing was chosen to be Δs_g= 0.2. The reference tube dimensions Δs and Δy along the *s* and *y* directions was chosen to be 0.4 and 0.1 respectively when evaluating the local area integral (eq. (3.15)). Thus, a time series of instantaneous burning area distributions were obtained from the G-field at a

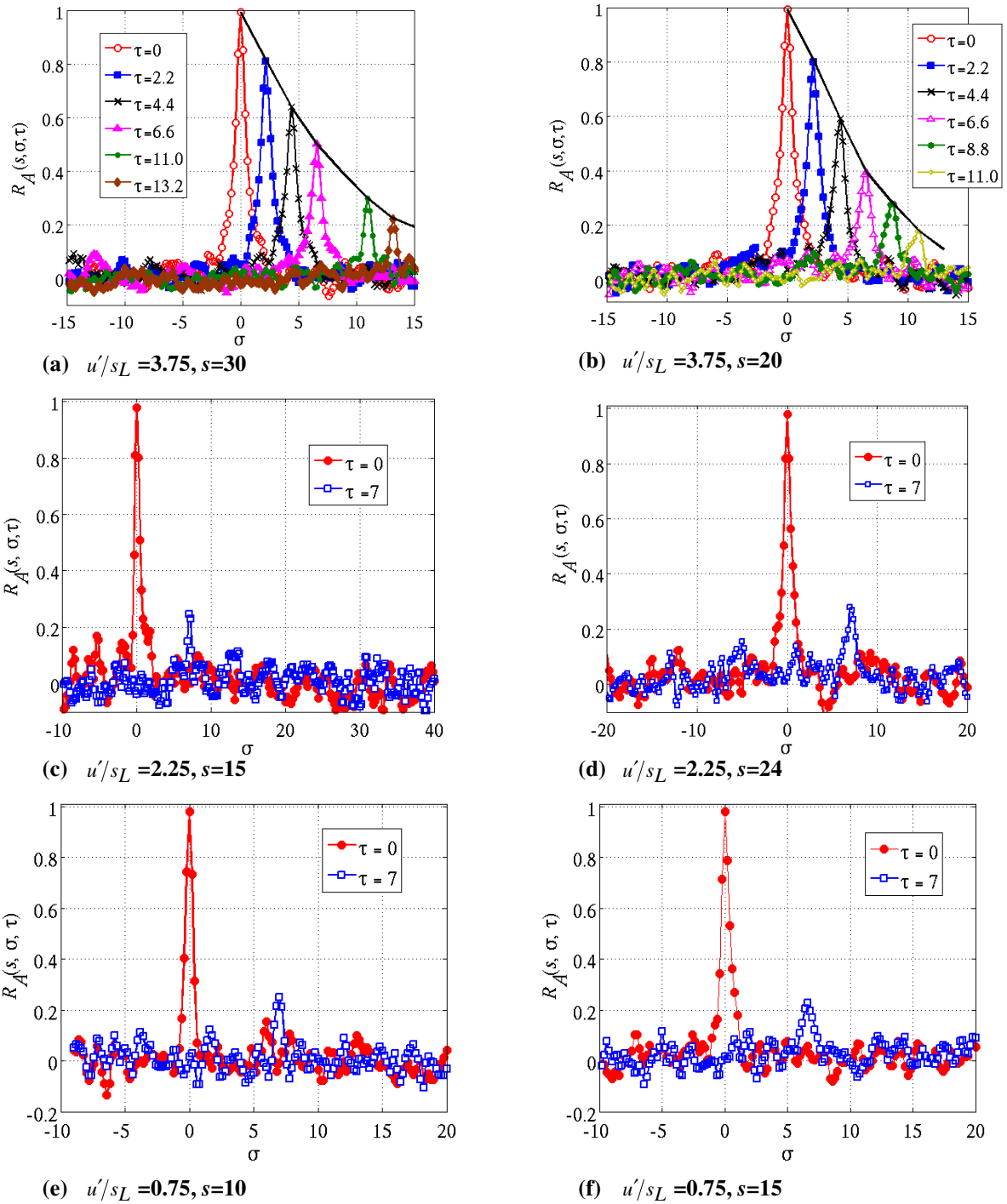

(a) u'/s_L **=3.75,** s**=30**

(b) u'/s_L **=3.75,** s**=20**

(c) u'/s_L **=2.25,** s**=15**

(d) u'/s_L **=2.25,** s**=24**

(e) u'/s_L **=0.75,** s**=10**

(f) u'/s_L **=0.75,** s**=15**

Figure 5-6: Local burning area correlation at different values of time interval τ at arbitrary locations on the flame surface as shown below each individual result. Turbulence intensities, (a)-(b) u'/s_L =3.75, (c)-(d) u'/s_L =2.25 and (e)-(f) u'/s_L =0.75. Also shown is the envelope of peak correlation values for each of the cases (a) and (b) where u'/s_L =3.75 (solid curve *sans* symbols).Flame angle, γ~4° for all cases.

non-dimensional sampling time period of Δt_s=2.2 for the $u'/s_L = 3.75$ case and Δt_s=7.0 for the u'/s_L =2.25 and u'/s_L =0.75 cases. The space-time correlation of local burning area fluctuations can be estimated from the above time series data using the following expression.

$$R_A(s,\sigma_s,\sigma_y,\tau) = \frac{\left\langle A_L(s+\sigma_s, y+\sigma_y, t+\tau) A_L(s,y,t)\right\rangle - \left\langle A_L(s+\sigma_s, y+\sigma_y, t+\tau)\right\rangle \left\langle A_L(s,y,t)\right\rangle}{\left\{\left\langle A_L(s,y,t)^2\right\rangle - \left\langle A_L(s,y,t)\right\rangle^2\right\}^{1/2} \left\{\left\langle A_L(s+\sigma_s, y+\sigma_y, t)^2\right\rangle - \left\langle A_L(s+\sigma_s, y+\sigma_y,,t)\right\rangle^2\right\}^{1/2}} \quad (5.1)$$

Figure 5-6a-f show the typical variation of the local burning area correlation R_A (eq. (5.1) along the s direction (σ_y = 0) for typical values of τ at two arbitrarily chosen flame surface locations for each of the three turbulence intensities. Note the qualitative similarity between these figures and the linear slope correlation results in fig.5-4. The peak correlation occurs at $\sigma = \tau \cos\gamma$ showing the advective characteristic. Also the peak values are seen to decay with increasing σ. This fact can be better appreciated from fig. 5-7 that plots the peak correlation envelopes at several different reference points on the

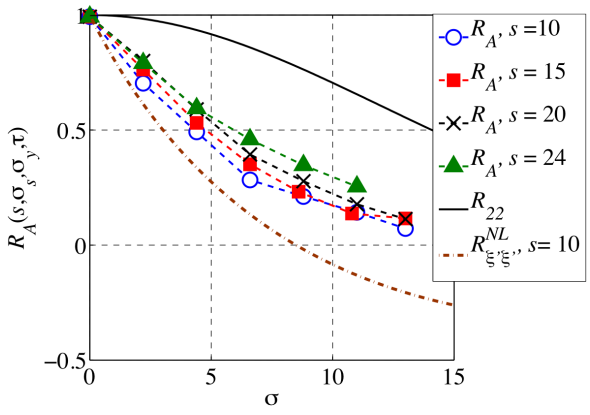

Figure 5-7: Envelope of local area fluctuations at different reference points u'/s_L =3.75, flame angle, γ ~4°. Also shown for reference is the velocity correlation envelope.

nominal flame surface (u'/s_L =3.75).

This decay of the peak correlation occurs in part for the same reasons that cause the peak slope correlation to decay in the linear case. However, in the present non-linear limit, the decay rate of the envelope of R_A is modified due to the influence of kinematic restoration that depends non-linearly upon u'/s_L. Kinematic restoration, results in the eventual destruction of wrinkles induced on the flame surface which also destroys local burning area. The effect of this local burning area destruction on the decay rate of the peak envelope of R_A is discussed next.

Figures 5-8a-b plots the typical variation of the envelope of R_A for three turbulence intensities at two different spatial locations corresponding to distances of s=15 and s=20 respectively, from the flame-holder. Also shown for reference, is the peak correlation envelope

of the velocity correlation function R_{22} along the flame surface. The decay rate of the envelope of R_A increases with increasing turbulence intensity. This trend can be explained

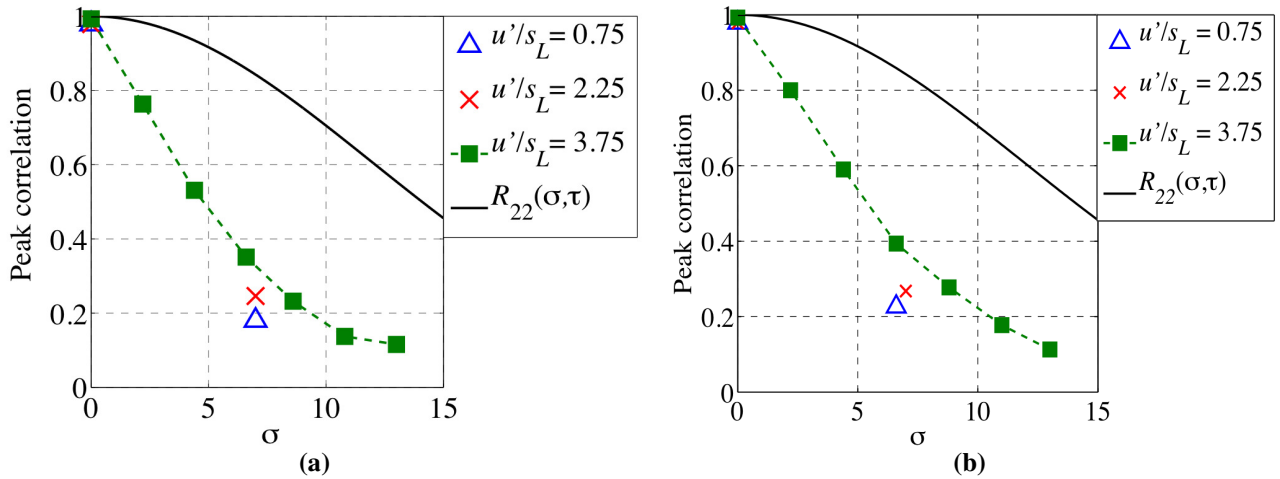

Figure 5-8: Envelope of local area fluctuations at three different turbulence intensities at a distance of a) s=15 and b) s=20 from the flameholder. Flame angle, γ ~4°. Also shown for reference is the velocity correlation envelope.

as follows Consider a wrinkle generated on the flame surface at some location *s*. Turbulence fluctuations excite a range of wrinkling length scales on this wrinkle as it moves downstream. Short wavelength length scales are destroyed quickly by kinematic restoration. Hence these have short correlation lengths when compared to larger wavelength wrinkles that are destroyed at a relatively slower rate. With increasing u'/s_L, these imposed wrinkles become larger i.e., have higher amplitude for a given wavelength. Thus the correlation length of the large wavelength wrinkles increases resulting in an increase in the overall correlation length of local burning area as fig. 5-9 suggests.

In summary, flame surface motions are correlated in time and space along the direction of the mean flow velocity tangential to the flame surface because 1) the velocity perturbations along the flame surface are spatio-temporally correlated and 2) wrinkle advection (non-locality). The presence of the latter effect results in flame surface motions having smaller correlation length scales than those of turbulence fluctuations. At high u'/s_L values, kinematic restoration results in an amplitude dependent filtering operation on flame surface wrinkles of different wavelengths. This results in a net increase in correlation length along the flame surface of large wavelength wrinkles with increasing u'/s_L causing an increase in the correlation length of R_A. The discussion thus far has shown, the influence of non-locality and kinematic restoration on flame surface kinematics through a correlation analysis of the flame surface slope and local burning area. These characteristics of flame surface wrinkling exert a quantitative influence on local consumption speed which is discussed next.

5.2 Local consumption speed

Local consumption speed was defined in general in chapter (see eq. (4.21) and the accompanying discussion). For the present analysis, the spatial variation of the local consumption speed is given by the following expression,

$$\frac{S_{T,LC}(s)}{s_L} = \frac{\langle A_L(s,t) \rangle}{\Delta s \Delta y} \tag{5.2}$$

Where, A_L is the mean local burning area given by eq. (3.15) and the denominator is simply the reference area which in this case, is the area of the patch on the nominal flame surface corresponding to A_L. Figure 5-9a shows the spatial variation of local consumption speed along the flame surface at three different values of u'/s_L (solid curves). These variations were determined by ensemble averaging local burning area realizations at each point from instantaneous snapshots of the G-field obtained from computations. Also

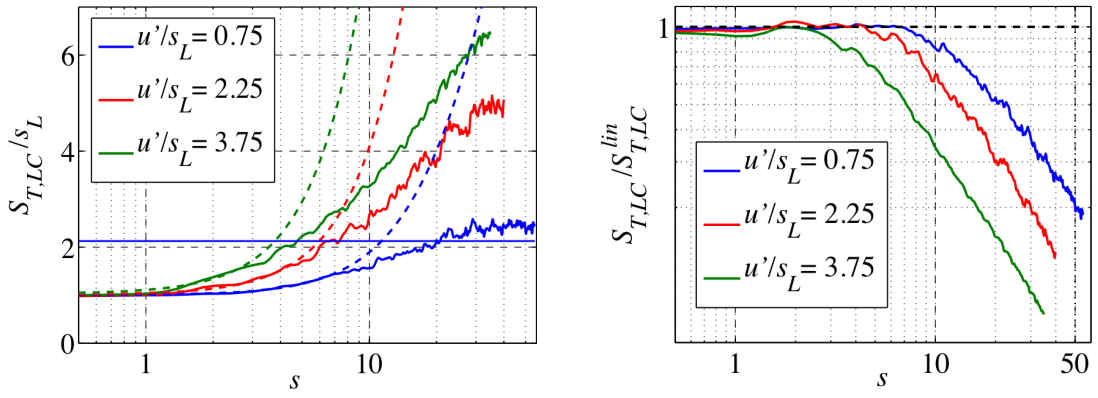

(a) **(b)**

Figure 5-9: Spatial variation of local consumption speed (a) normalized by s_L and (b) normalized by $S_{T,LC}^{Lin}$,at three different turbulence intensities (solid curves) given by the value of u'/s_L . Flame angle, γ ~ 4°. Also shown are the corresponding predictions from linear kinematic theory in each case (broken curves). The horizontal blue line in (a) is the prediction from the theory of Aldredge for u'/s_L =0.75.

shown are the corresponding variations of local consumption speed predicted from the linear non-local theory (eq. (4.34) in chapter 4, broken curves). It is seen that the local consumption speed grows with increasing distance from the flame holder because the flame surface becomes progressively more wrinkled as distance from the flameholder increases.

Figure 5-9b shows the spatial variation of $S_{T,LC}$ normalized by the corresponding value of $S_{T,LC}^{Lin}$ predicted from the linear kinematic theory developed in the previous chapter (eq. (4.36)) for three values of u'/s_L. First, note that all the curves from the computations approach unity as s $\rightarrow$ 0. Also, note that the linear theory reasonably predicts the behavior of local consumption speed for small distances from the flame holder (eg. upto s ~ 8 for u'/s_L = 0.75). Due to flame attachment, the flame surface is relatively less "free" to move close to the flame-holder. Therefore, this initial region is associated with linear flame dynamics. This results in small flame wrinkling amplitudes and flame surface slopes resulting in good agreement of $S_{T,LC}$ with linear theory a fact shown previously, for harmonically forced V-flames (ref. Shanbhogue [48]). With further increase in distance from the flame-holder, the amplitude of flame surface wrinkling increases up to a point where non-linear effects become important. Subsequent growth of $S_{T,LC}$ is then controlled by kinematic restoration which begins to decrease relative rates of wrinkle growth. This causes $S_{T,LC}$ to depart from its linear value. (eg. s ~ 8 for u'/s_L = 0.75). Eventually, it is possible that a dynamic equilibrium between area destruction by kinematic restoration and area creation by flame surface wrinkling is reached, causing the local burning area and hence $S_{T,LC}$ to saturate. This saturation can be seen from fig. 5-10

for the u'/s_L = 0.75 case for $s > 30$. The saturation value for the other two u'/s_L cases was not reached in the present computations. However, in practical situations, the presence of a temperature jump across the flame surface will influence the growth rate of flame surface perturbations due to flame front instabilities such as the Darrieus-Landau instability and/or thermo-diffusive instability. The quantitative impact of these instabilities on the local consumption speed at a given distance from the flame-holder depends on the ratio between the characteristic growth time of these instabilities and the advection time for a wrinkle induced at the flame base to reach the given flame surface location ($s/\cos\gamma$). Hence, the final fully developed local consumption speed (if it exists) will be the resultant of kinematic restoration, flame front instabilities and flame wrinkling due to turbulent velocity fluctuations.

In summary, the present results show that the growth of local consumption speed with increasing distance from the flame-holder can be divided into three regions

1. Linear growth region – local consumption speed growth is described by linear kinematic theory close to the flame-holder.

2. Non-linearity growth region – the spatial growth rate of the local consumption speed is reduced due to increasing effect of kinematic restoration resulting in burning area destruction.

3. Fully developed region– local consumption speed saturates due to a dynamic equilibrium between burning area creation by turbulence and destruction by kinematic restoration.

Next, the implications of non-locality for the development of turbulence-chemistry closure models will be discussed in the perspective of a few existing turbulence closure approaches prevalent in the literature.

5.3 Implications for modeling

As fundamental closure problem in the computation of turbulent premixed flows is determination of the averaged (RANS/URANS) or subfilter (LES) reaction rate term. Several approaches with varying levels of success have been developed over the past several decades to address this problem (Poinsot Veynante [6]). The discussion in this section begins by considering a class of reaction rate closures that have been developed for the Reynolds or Favre averaged progress variable equation presented below (in tensor index notation, dimensional variables).

$$\frac{\partial\left(\bar{\rho}\tilde{c}\right)}{\partial t}+\frac{\partial\left(\bar{\rho}\tilde{u}_j\tilde{c}\right)}{\partial x_j}=-\frac{\partial\left(\overline{\rho u_j'' c''}\right)}{\partial x_j}+\bar{\rho}\tilde{W} \tag{5.3}$$

Where, '~' represents Favre averaging. The first of the two unclosed terms on the RHS represents the change in local mean progress variable due to turbulent velocity fluctuations. Therefore, this term represents a "turbulent" transport type process. The second term on the RHS is the Favre averaged reaction rate term. At first, it is easy to think of these two terms as being independent of each other. However, this is not the case as the sum of the terms on the RHS represents the total contribution to the change in mean progress variable due to unsteady flame surface motions as has been discussed in the review of Lipatnikov and Chomiak [11]. Hence in general, any closure model for the RHS of eq. (5.3), must be a closure for both RHS terms considered together. A popular

closure model for this term was developed by Zimont [15]. In this approach, the RHS eq. (5.3) is replaced with the sum of a "turbulent" gradient diffusion term and a mass burning rate term through the specification of a local consumption speed as follows[6],

$$\frac{\partial\left(\bar{\rho}\tilde{c}\right)}{\partial t}+\frac{\partial\left(\bar{\rho}\tilde{u}_j\tilde{c}\right)}{\partial x_j}=\frac{\partial}{\partial x_j}\left(\bar{\rho}D_t\frac{\partial\tilde{c}}{\partial x_j}\right)+\bar{\rho}S_c\left|\nabla\tilde{c}\right| \tag{5.4}$$

where D_t is a turbulent diffusivity and S_c is the local consumption speed. These are modeled using heuristic arguments based on an assumption of passive scalar diffusion for $\tilde{c}$ as $D_t \sim u'L_{11}$ and $S_c = Au'^{3/4}L_{11}^{1/4}s_L^{1/2}$ (dimensional form) (Zimont [15].). The coefficient A in the model for S_c is a parameter that must be specified. The aim of this approach is to model turbulent premixed flames in that are characterized by a spatially growing flame brush thickness but a fully developed local consumption speed (Prudnikov [49]). The above is an example of a general class of closure approaches known as the Flame Speed Closure (FSC) approach in the literature. Several other heuristic closures for S_c have been reviewed in Lipatnikov and Chomiak [11]. All of them are based more or less on arguments similar to those of Zimont. All of these models however, have adjustable parameters that need to be specified. However, it has been shown in this work that non-locality and flame attachment both affect the spatial distribution of flame speed. Hence, care must be taken to ensure that the values for the adjustable parameters from one

---

[6] Here, the consumption speed S_c represents a measure of the local mass burning rate associated with a $\tilde{c}$ level surface. The local normal direction and local elemental reference burning area vector are given by $\vec{n}=-\nabla\tilde{c}/\left|\nabla\tilde{c}\right|$ and $\tilde{\nabla}c$ respectively. Hence the local average reaction rate per unit volume is given by $\tilde{W} = -S_c\left(\nabla\tilde{c}\bullet\nabla\tilde{c}/\left|\nabla\tilde{c}\right|\right) = -S_c\left|\nabla\tilde{c}\right|$.

configuration must not be applied to a different configuration eg: The parameters for local consumption speed in a low-swirl burner may not be the same as the parameters for a flame in a spherical bomb due to the present of non-locality effects in the former case.

None of the various closure approaches mentioned above account for a spatially developing local consumption speed. The first attempt to capture this effect appears to be that of Lipatnikov and Chomiak[11]. They modified the Zimont model by replacing the constant D_t by a time dependent expression derived from the theory of turbulent diffusion of passive scalars. This yields a spatially varying local consumption speed using arguments similar to those of Zimont as follows,

$$\frac{S_{T,LC}}{s_L} = \frac{S_{c,o}}{s_L}\left[1+\frac{\tau'}{t_{fd}}\left\{e^{-t_{fd}/\tau'}-1\right\}\right]^{1/2} \tag{5.5}$$

Where, t_{fd}/τ' is the ratio of the so-called flame development time to a typical time scale for turbulent diffusion and $S_{c,o}$ is the value of the fully developed flame speed at large distances from the flame holder. The flame development time t_{fd} is the time taken for a fluid particle to travel from the flame holder to the flame surface. Thus, for the analysis presented in this work, $t_{fd}/\tau' = (s\cos\gamma/U_o)/(L_{11}/u') = (s/2)(u'/s_L)\sin 2\gamma$. Thus, eq. (5.5) can be rewritten as

$$\frac{S_c}{s_L} = \frac{S_{c,o}}{s_L}\left[1+\frac{1}{(s/2)(u'/s_L)\sin 2\gamma}\left\{e^{-(s/2)(u'/s_L)\sin 2\gamma}-1\right\}\right]^{1/2} \tag{5.6}$$

The above model will be referred to as the LC model. From the above it is clear that the consumption speed attains the fully developed value, $S_{c,o}$, at large values of s and varies

spatially otherwise. It is interesting therefore, to compare the predictions of initial spatial development of $S_{T,LC}$ from the above model and the results in the present work for the same values of the fully developed value $S_{c,o}$.

The fully developed local consumption speed for the u'/s_L =0.75 case, from present computations, is given by 2.4 (see fig. 5-9a). This value was obtained by taking the average of the local consumption speed values for the u'/s_L =0.75 case between *s*=30 and *s*=50, corresponding to the fully developed region. Thus, using this value in eq. (5.6) ensures that the LC model predicts the same local consumption speed in at large distances from the flameholder as the present computations. Figure 5-10 shows the spatial variation of local consumption speed determined from eq. (5.6) and computations in the present work for the u'/s_L =0.75 case. The agreement between the LC model and the present computations is poor in the initial flame development region. The LC model predicts a growing consumption speed for s>30 where the computations show that the local

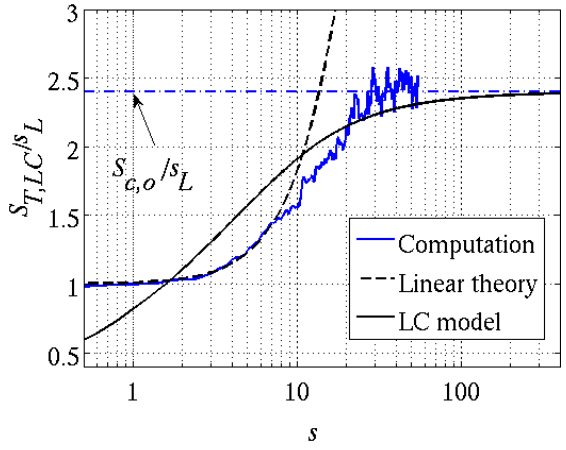

Figure 5-10: Comparison between present computations and the prediction from the local consumption speed model of Lipatnikov and Chomiak (u'/s_L =0.75, γ~4°). Also shown is the prediction from the linear theory (broken curve) developed in the present work.

consumption speed has attained a fully developed state. The possible reasons for this discrepancy are discussed next.

At the flame attachment location, the change in the Favre averaged progress variable must be zero. This means that the RHS of eq. (5.3) must vanish in general for any modeling approach at attachment locations. However, as discussed earlier, the two terms on the RHS are representative of flame kinematics and are not independent of each other. Hence, it is possible to envisage a model where the RHS of eq. (5.3) vanishes at the flame attachment location without each of the two terms vanishing independently. However, this is precisely what happens in the LC model (see the derivation in ref. [11]). Also, the assumption of passive scalar diffusion for mean progress variable in order to derive eq. (5.5) implies that fine scale changes in progress variable value at any point in the flame brush are affected only by local velocity fluctuations. The comparison between peak correlation envelopes of local and non-local correlations presented earlier (see fig. 5-5), suggests that flame surface motions (eg. local burning area) must be correlated in time over length scales that are of the order of the projected integral length scale of the turbulent velocity fluctuations along the flame as was shown for the local slope correlation. However, this is not the case when the flame response is non-local. Hence, this suggests that using a passive scalar diffusion model for local consumption speed is incomplete, at least for the low u'/s_L cases considered here.

Several phenomenological models for consumption speed have been obtained by fitting an expression of the form $S_c/s_L = C\left(u'/s_L\right)^n$ to experimental data (e.g. Kobayashi [50], Bradley [51]) where u'/s_L is a representative turbulence intensity in the flow field.

The constants C and n in these models essentially account for the fully non-linear flame kinematic processes discussed thus far. The values of $S_{T,LC}/s_L$ for each of the present computations are in reasonable agreement with the range of values predicted by these models, eg. The heuristic expression of Bray [52] for an unstretched flame neglecting gas, $S_{T,LC}/s_L = 2.56\left(u'/s_L\right) = 1.92$. However, it must be noted that most of these measurements are *global* consumption speed measurements (see eq. (4.20) and the accompanying discussion). Hence, using these measurements to develop models to close the spatially varying reaction rate term in eq. (5.4) is problematic. Again, the effect of boundary conditions also reduces the universality of the values of C and n across different flame configurations. Recently, Yung-Cheng Chen et al. [53] have measured local consumption speeds for premixed turbulent stagnation point flames (lean Propane/air, lean and rich hydrogen air). Their results show that the local consumption speed varies along the radial direction (see fig. 14 and accompanying discussion in Yung-Cheng Chen et al [53]). While a quantitative comparison between their experiments and the present theory is not possible due to the difference in configurations, their observation is consistent with the predictions of the non-local flame response theory developed in this work.

A rigourous asymptotic analysis for the flame surface kinematics of a freely propagating nominally flat flame in an upstream isotropic and stationary turbulent flow was first performed by Clavin and Williams[54] and later generalized by Aldredge and Williams[44]. From arguments on the general characteristics of the energy spectrum of isotropic turbulence, Aldredge[46] derived an expression for the local consumption speed

from eq. (4.32) as, $S_c/s_L = 1+2\left(u'/s_L\right)^2$. This yields, S_c/s_L ~2.1, 11.0 and 29.0 for u'/s_L =0.75, 2.25 and 3.75 respectively. These values are significantly different from the values of local consumption speed in the fully developed region as shown by fig. 5-9 for the latter two values of u'/s_L because the theory in Aldredge[46] does not capture the effect of kinematic restoration or non-locality. Hence, such "local" models can be used only when there is no non-zero mean tangential flow to the flame surface.

It has been suggested that closures based on modeling the flame surface density equation may successfully capture the effect of non-locality on flame surface motions (Driscoll [12]). This equation has been derived by several groups on the past (Marble Broadwell [55], Trouve Poinsot [13]). A set of closure models for source terms in the latter have been derived from analysis of DNS databases of freely propagating flames in isotropic turbulence (Trouve Poinsot [13]). While this latter approach is attractive since closure models for arbitrarily complex reaction chemistry can be developed, it cannot account for a) the effect of flame attachment boundary conditions and b) the effect of non-locality as both of these aspects are not captured by the DNS. However, these closure models may be applicable in scenarios where there is no mean tangential velocity to the flame brush. Similar DNS studies of freely propagating flames ignoring heat release across the flame surface in order to develop closure models for consumption speed within the framework of the *G*-equation approach (Peters [5]) have been performed by Wenzel and Peters[56, 57]. The validity of this approach is restricted to scenarios where there is no net mean flow along the flame brush because of the same reasons as described above.

The analysis/results presented up to this point has focused on the response characteristics of turbulent flames that are not forced by any coherent velocity fluctuations. The next chapter presents the theoretical formulation for the response of an acoustically forced turbulent premixed flame.

Chapter 6

Forced flame response – Theoretical formulation

This chapter develops a theoretical formulation for the ensemble averaged heat release response of an axis-symmetric center-body stabilized turbulent flame to coherent acoustic forcing. Prior numerical studies of Santosh *et al* [4] showed that the ensemble averaged heat release response at large amplitudes of acoustic forcing is different from the equivalent value determined from existing models for laminar flame response with the laminar flame speed replaced by a modified turbulent displacement speed. Thus, it was concluded that the presence of turbulence changes the ensemble averaged heat release response and that the effect of turbulence is not just that of additive noise. The theoretical formulation presented in this chapter formally shows this result by developing an exact expression for the leading order turbulence correction to the linear laminar transfer functions developed in Schuller *et al*[29] and Preetham *et al*[30], using the technique of asymptotic expansions.

Next, a general modeling framework to determine heat release response using modified flame propagation speed(s) is developed. It is shown that in general, a model for *both* local consumption and displacement speeds are required to rationally model heat release transfer function of the turbulent flame. Expressions for these speeds are developed from the theoretical analysis developed in this chapter. The prediction from this model is compared with predictions from a prior model of Lipatnikov and Sathiah [31] for the flame transfer function of axis-symmetric (in an average sense) centerbody stabilized flames. The rest of this chapter is organized as follows. The essential details of

the theoretical formulation are shown in the following section titled "Theoretical formulation". This is followed by the section that develops the modeling approach titled, "Response Modeling".

6.1 Theoretical formulation

The investigated geometry is shown schematically in Figure 6-1. The analysis in this section will be performed in the burner fixed r-z-θ co-ordinate system as shown. The principal assumptions made in the analysis are the same as stated in chapter 3. The G-equation (eq. (2.3)) in the present burner fixed co-ordinates may be written in dimensional form as,

$$\frac{\partial G}{\partial t}+u\frac{\partial G}{\partial r}+\frac{u_\theta}{r}\frac{\partial G}{\partial \theta}+v\frac{\partial G}{\partial z}=s_L\sqrt{\left(\frac{\partial G}{\partial r}\right)^2+\frac{1}{r^2}\left(\frac{\partial G}{\partial \theta}\right)^2+\left(\frac{\partial G}{\partial z}\right)^2} \qquad (6.1)$$

where, u, u_θ and v are the instantaneous flow velocity components in the r, θ and z directions respectively. Choosing, $G(r,\theta,z,t)=z-\zeta(r,\theta,t)$ in the above yields,

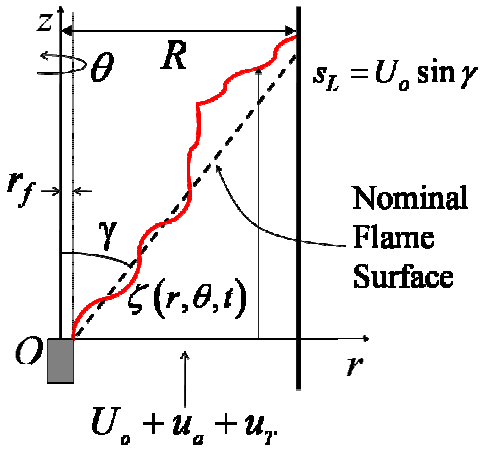

Figure 6-1: Schematic of investigated geometry - axis-symmetric bluff-body stabilized flame.

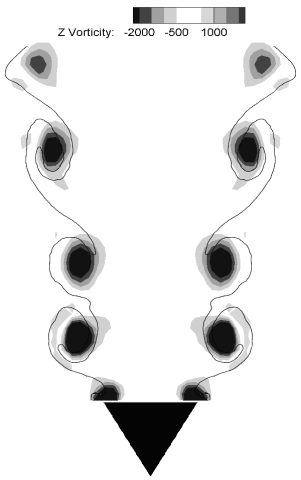

Figure 6-2: Instantaneous image of flame contour and vorticity distribution. Flow is from bottom to top. Image courtesy, Shanbhogue et al [58] (reproduced with permission).

$$\frac{\partial \zeta}{\partial t} + u\frac{\partial \zeta}{\partial r} + \frac{u_\theta}{r}\frac{\partial \zeta}{\partial \theta} - v = -s_L\sqrt{1+\left(\frac{\partial \zeta}{\partial r}\right)^2 + \frac{1}{r^2}\left(\frac{\partial \zeta}{\partial \theta}\right)^2} \tag{6.2}$$

The above can be written in non-dimensional form using: $\left(r^*, z^*\right) = \left(r, z\right)/L_{11}$, $\zeta^* = \zeta/L_{11}$, $\left(u_s^*, v^*, u_\theta^*\right) = \left(u_s, v, u_\theta\right)/U_o$ as,

$$\frac{\partial \zeta^*}{\partial t^*} + u^*\frac{\partial \zeta^*}{\partial r^*} + \frac{u_\theta^*}{r^*}\frac{\partial \zeta^*}{\partial \theta^*} - v^* = -\sin\gamma\sqrt{1+\left(\frac{\partial \zeta^*}{\partial r^*}\right)^2 + \frac{1}{r^{*2}}\left(\frac{\partial \zeta^*}{\partial \theta^*}\right)^2} \tag{6.3}$$

Where, the asterisks represent non-dimensional quantities. These asterisks will be dropped in what follows for notational convenience with the understanding that all expressions henceforth are presented in non-dimensional form unless otherwise specified.

It has been shown in the case of acoustically forced flames that the primary source of coherent velocity perturbations comes from the shedding of vortices caused by shear layer rollup downstream of the flame holding location due to acoustic forcing (Durox et al [59] see also fig. 6-2). Therefore, the net magnitude and phase of the global heat release fluctuations relative to the imposed excitation are characterized by first, the wavelength of the flame surface wrinkles relative to the characteristic dimension of the

flame and second, by the length scale associated with the imposed perturbation. In practical situations, the flame is confined within the combustor liner of a finite radius. Thus, for a specified mean flow velocity and laminar flame speed s_L, the flame has a fixed nominal height denoted by L_f for a given combustor radius, R (see fig. 6-1). Hence, the velocity field in eq. (6.3) is now specified as a superposition of a coherent harmonic excitation with a convected characteristic and a spatially isotropic and stationary turbulence field as follows,

$$\begin{aligned} u(r,\theta,\zeta,t) &= \frac{1}{2}\frac{KSt}{\Lambda}\varepsilon_a r \sin\left[\frac{St}{\Lambda}(K\zeta - t)\right] + \varepsilon_T f_v(r,\theta,\zeta,t) \\ u_\theta(r,\theta,\zeta,t) &= \varepsilon_T f_\theta(r,\theta,\zeta,t) \\ v(r,\theta,\zeta,t) &= 1 + \varepsilon_a \cos\left[\frac{St}{\Lambda}(K\zeta - t)\right] + \varepsilon_T f_u(r,\theta,\zeta,t) \end{aligned} \tag{6.4}$$

Where, the various parameters in the above are defined as follows,

- $\varepsilon_a = u_a'/U_o$ - the amplitude of the coherent excitation component normalized by the mean flow velocity U_o.
- $St = \omega L_f/U_o$ - excitation strouhal number defined in terms of the nominal flame length.
- $\Lambda = L_f/L_{11}$ - the normalized nominal flame length.
- $K = U_o/u_c$ - u_c is the convective velocity of the imposed vortical structures.
- $\varepsilon_T = u_{RMS}'/U_o$, RMS velocity of the background turbulence normalized by mean velocity.
- f_u, f_v, f_θ zero-mean unity variance random functions of their arguments representing the underlying structure of the turbulence velocity fluctuations.

The above specification is a generalization of the velocity field specification used in the laminar flame response analysis of Preetham *et al* [30].

Next, the flame surface shape can be written as a two parameter expansion in ε_a and ε_T as follows,

$$\begin{aligned}\zeta(r,\theta,t) = {} & \zeta_o(r,\theta) + \varepsilon_T \zeta_{1t}(r,\theta,t) + \varepsilon_T^2 \zeta_{2t}(r,\theta,t) + \ldots \\ & + \varepsilon_a \left\{ \zeta_{1c}(r,\theta,t) + \varepsilon_T \zeta_{2ct}(r,\theta,t) + \varepsilon_T^2 \zeta_{3ctt}(r,\theta,t) + \ldots \right\} + \varepsilon_a^2 \{\ldots\} + \ldots \end{aligned} \tag{6.5}$$

where the contribution to the flame surface shape at each order of acoustic forcing amplitude, ε_a has been further expanded into contributions in terms of ε_T. Physically, these contributions capture the effect of coupling between the response due to coherent forcing and the random flame surface wrinkling due to turbulence fluctuations. Henceforth, this coupling with be referred to as "kinematic coupling". Using the above together with the velocity field specification in eq. (6.4) yields the following system of equations.

$O(\varepsilon_a^0)$:

$$\zeta_o(r,\theta) = (r - r_f)\cot\gamma \tag{6.6}$$

$$\frac{\partial \zeta_{1t}}{\partial t} + \cos\gamma \sin\gamma \frac{\partial \zeta_{1t}}{\partial r} = \frac{f_n\left(r,\theta,z=(r-r_f)\cot\gamma,t\right)}{\sin\gamma} \tag{6.7}$$

$$\begin{aligned}\frac{\partial \zeta_{2t}}{\partial t} + \cos\gamma \sin\gamma \frac{\partial \zeta_{2t}}{\partial r} = {} & -\frac{1}{r} f_\theta\left(r,\theta,(r-r_f)\cot\gamma,t\right)\frac{\partial \zeta_{1t}}{\partial \theta} - f_u\left(r,\theta,(r-r_f)\cot\gamma,t\right)\frac{\partial \zeta_{1t}}{\partial r} \\ & - \frac{\sin^2\gamma}{2r^2}\left(\frac{\partial \zeta_{1t}}{\partial \theta}\right)^2 - \sin^4\gamma\left(\frac{\partial \zeta_{1t}}{\partial r}\right)^2 + \frac{\zeta_{1t}(r,\theta,t)}{\sin\gamma}\left\{\left.\frac{\partial f_n}{\partial z}\right|_{\left(r,\theta,z=(r-r_f)\cot\gamma,t\right)}\right\}\end{aligned} \tag{6.8}$$

$O(\varepsilon_a)$:

$$\frac{\partial \zeta_{1c}}{\partial t}+\cos\gamma\sin\gamma\frac{\partial \zeta_{1c}}{\partial r}=\cos\left\{\frac{St}{\Lambda}\left(t-K\left(r-r_f\right)\cot\gamma\right)\right\}+\frac{1}{2}r\frac{KSt}{\Lambda}\cot\gamma\sin\left\{\frac{St}{\Lambda}\left(t-K\left(r-r_f\right)\cot\gamma\right)\right\} \tag{6.9}$$

$$\begin{aligned}\frac{\partial \zeta_{2ct}}{\partial t}+\sin\gamma\cos\gamma\frac{\partial \zeta_{2ct}}{\partial r}=&-\zeta_{1t}\left(r,\theta,t\right)\left(\begin{array}{l}\frac{1}{2}r\frac{K^2St^2}{\Lambda^2}\cos\left[\frac{St}{\Lambda}\left(t-K\left(r-r_f\right)\cot\gamma\right)\right]\cot\gamma\\-\frac{KSt}{\Lambda}\sin\left[\frac{St}{\Lambda}\left(t-K\left(r-r_f\right)\cot\gamma\right)\right]\end{array}\right)\\&-f_u\left(r,\theta,\left(r-r_f\right)\cot\gamma,t\right)\frac{\partial \zeta_{1c}}{\partial r}+\frac{1}{2}\frac{\partial \zeta_{1t}}{\partial r}r\frac{KSt}{\Lambda}\sin\left[\frac{St}{\Lambda}\left(t-K\left(r-r_f\right)\cot\gamma\right)\right]\\&-\sin^4\gamma\frac{\partial \zeta_{1c}}{\partial r}\frac{\partial \zeta_{1t}}{\partial r}-\frac{\zeta_{1c}\left(r,\theta,t\right)}{\sin\gamma}\left\{\left.\frac{\partial f_n}{\partial z}\right|_{\left(r,\theta,z=\left(r-r_f\right)\cot\gamma,t\right)}\right\}\end{aligned} \tag{6.10}$$

where,

$$\frac{f_n\left(r,\theta,z=\left(r-r_f\right)\cot\gamma,t\right)}{\sin\gamma}=f_v\left(r,\theta,z=\left(r-r_f\right)\cot\gamma,t\right)-f_u\left(r,\theta,z=\left(r-r_f\right)\cot\gamma,t\right)\cot\gamma \tag{6.11}$$

The flame attachment assumption (assumption 5) implies the following boundary condition for each of the eqs. (6.6)-(6.10),

$$\zeta_i\left(r_f,\theta,t\right)=0 \tag{6.12}$$

The equation for the $O\left(\varepsilon_T^2\right)$ correction at $O\left(\varepsilon_a\right)$ is presented in Appendix D (eq. (D.15)). The system of equations, (6.6)-(6.10) together with eq. (D.15) must be solved to determine the heat release response of the turbulent flame to leading order in ε_a and ε_T. Equations (6.6) and (6.9) describe laminar flame response. The remaining equations are needed because to capture the effect of kinematic coupling (to leading order). Also, from

eq. (6.9), it is clear that the leading order flame response contribution at $O(\varepsilon_a)$ i.e., the laminar response, is axis-symmetric. Thus, terms involving derivatives of this contribution *w. r. t.* 'θ' vanish and have been omitted from the above equations. Next, an expression for the leading order turbulence correction to the heat release response will be derived.

The instantaneous heat release rate of the flame normalized by the heat release rate of the nominal flame surface is given by the following,

$$q(t)=\frac{\sin\gamma}{\pi\left(R^2-r_f^2\right)}\int_{r_f}^{R}\int_{0}^{2\pi} drd\theta\; r\sqrt{1+\frac{1}{r^2}\left(\frac{\partial\zeta}{\partial\theta}\right)^2+\left(\frac{\partial\zeta}{\partial r}\right)^2} \tag{6.13}$$

Where, R is the radius of the combustor normalized by L_{11}. Using the expansion in eq. (6.5) in the above yields,

$$q(t)=\frac{1}{\pi\left(R^2-r_f^2\right)}\int_{r_f}^{R}\int_{0}^{2\pi} drd\theta\; r\left[\begin{array}{l} 1+\cos\gamma\sin\gamma\dfrac{\partial\zeta_{1t}}{\partial r}\varepsilon_T+\left\{\begin{array}{l}\dfrac{\sin^2\gamma}{2r^2}\left(\dfrac{\partial\zeta_{1t}}{\partial\theta}\right)^2+\dfrac{1}{2}\sin^4\gamma\left(\dfrac{\partial\zeta_{1t}}{\partial r}\right)^2\\ +\cos\gamma\sin\gamma\dfrac{\partial\zeta_{2t}}{\partial r}\end{array}\right\}\varepsilon_T^2 \\ +\left\{\begin{array}{l}\cos\gamma\sin\gamma\dfrac{\partial\zeta_{1c}}{\partial r}+\left\{\sin^4\gamma\dfrac{\partial\zeta_{1c}}{\partial r}\dfrac{\partial\zeta_{1t}}{\partial r}+\cos\gamma\sin\gamma\dfrac{\partial\zeta_{2ct}}{\partial r}\right\}\varepsilon_T \\ +\left(\begin{array}{l}\dfrac{\sin^2\gamma}{r^2}\dfrac{\partial\zeta_{1t}}{\partial\theta}\dfrac{\partial\zeta_{2ct}}{\partial\theta}-\dfrac{\cos\gamma\sin^3\gamma}{2r^2}\left(\dfrac{\partial\zeta_{1t}}{\partial\theta}\right)^2\dfrac{\partial\zeta_{1c}}{\partial r}\\ -\dfrac{3}{2}\cos\gamma\sin^5\gamma\dfrac{\partial\zeta_{1c}}{\partial r}\left(\dfrac{\partial\zeta_{1t}}{\partial r}\right)^2\\ +\sin^4\gamma\left(\dfrac{\partial\zeta_{1t}}{\partial r}\dfrac{\partial\zeta_{2ct}}{\partial r}+\dfrac{\partial\zeta_{1c}}{\partial r}\dfrac{\partial\zeta_{2t}}{\partial r}\right)+\cos\gamma\sin\gamma\dfrac{\partial\zeta_{3ctt}}{\partial r}\end{array}\right)\varepsilon_T^2\end{array}\right\}\varepsilon_a \end{array}\right] \tag{6.14}$$

Noting from the azimuthal symmetry of the configuration, that ensemble averages are independent of θ for the present case of isotropic and stationary turbulence, yields the following from ensemble averaging of the above,

$$\begin{aligned}\left\langle q(t)\right\rangle = 1 &+ \frac{2\varepsilon_T^2}{\left(R^2-r_f^2\right)}\int_{r_f}^{R} dr\ r\left\{\begin{array}{l}\dfrac{\sin^2\gamma}{2r^2}\left\langle\left(\dfrac{\partial\zeta_{1t}}{\partial\theta}\right)^2\right\rangle+\dfrac{1}{2}\sin^4\gamma\left\langle\left(\dfrac{\partial\zeta_{1t}}{\partial r}\right)^2\right\rangle \\ +\cos\gamma\sin\gamma\left\langle\dfrac{\partial\zeta_{2t}}{\partial r}\right\rangle\end{array}\right\} \\ &+\frac{2\varepsilon_a}{\left(R^2-r_f^2\right)}\int_{r_f}^{R} dr\ r\left\{\cos\gamma\sin\gamma\frac{\partial\zeta_{1c}}{\partial r}\right\} \\ &+\frac{2\varepsilon_T^2\varepsilon_a}{\left(R^2-r_f^2\right)}\int_{r_f}^{R} dr\ r\left(\begin{array}{l}\dfrac{\sin^2\gamma}{r^2}\left\langle\dfrac{\partial\zeta_{1t}}{\partial\theta}\dfrac{\partial\zeta_{2ct}}{\partial\theta}\right\rangle-\dfrac{\cos\gamma\sin^3\gamma}{2r^2}\left\langle\left(\dfrac{\partial\zeta_{1t}}{\partial\theta}\right)^2\right\rangle\dfrac{\partial\zeta_{1c}}{\partial r} \\ -\dfrac{3}{2}\cos\gamma\sin^5\gamma\dfrac{\partial\zeta_{1c}}{\partial r}\left\langle\left(\dfrac{\partial\zeta_{1t}}{\partial r}\right)^2\right\rangle \\ +\sin^4\gamma\left(\left\langle\dfrac{\partial\zeta_{1t}}{\partial r}\dfrac{\partial\zeta_{2ct}}{\partial r}\right\rangle+\dfrac{\partial\zeta_{1c}}{\partial r}\left\langle\dfrac{\partial\zeta_{2t}}{\partial r}\right\rangle\right)+\cos\gamma\sin\gamma\left\langle\dfrac{\partial\zeta_{3ctt}}{\partial r}\right\rangle\end{array}\right)\end{aligned} \tag{6.15}$$

The first two terms on the RHS of the above represent the nominal heat release rate and the leading order turbulence correction to the nominal heat release rate. The third term represents the linear laminar heat release response of the flame and the last term represents the leading order turbulence correction at linear order in acoustic forcing. Therefore the net ensemble averaged fluctuation in the heat release rate i.e. the heat release response, is given by the following,

$$\left\langle q'(t)\right\rangle = \frac{2\varepsilon_a}{\left(R^2 - r_f^2\right)}\int_{rf}^{R} dr\ r\left\{\cos\gamma\sin\gamma\frac{\partial\zeta_{1c}}{\partial r}\right\}$$
$$+\frac{2\varepsilon_T^2\varepsilon_a}{\left(R^2 - r_f^2\right)}\int_{rf}^{R} dr\ r\left(\begin{array}{l}\dfrac{\sin^2\gamma}{r^2}\left\langle\dfrac{\partial\zeta_{1t}}{\partial\theta}\dfrac{\partial\zeta_{2ct}}{\partial\theta}\right\rangle - \dfrac{\cos\gamma\sin^3\gamma}{2r^2}\left\langle\left(\dfrac{\partial\zeta_{1t}}{\partial\theta}\right)^2\right\rangle\dfrac{\partial\zeta_{1c}}{\partial r}\\ -\dfrac{3}{2}\cos\gamma\sin^5\gamma\dfrac{\partial\zeta_{1c}}{\partial r}\left\langle\left(\dfrac{\partial\zeta_{1t}}{\partial r}\right)^2\right\rangle\\ +\sin^4\gamma\left(\left\langle\dfrac{\partial\zeta_{1t}}{\partial r}\dfrac{\partial\zeta_{2ct}}{\partial r}\right\rangle + \dfrac{\partial\zeta_{1c}}{\partial r}\left\langle\dfrac{\partial\zeta_{2t}}{\partial r}\right\rangle\right) + \cos\gamma\sin\gamma\left\langle\dfrac{\partial\zeta_{3ctt}}{\partial r}\right\rangle\end{array}\right)$$

(6.16)

The ensemble averaged heat-release rate transfer function is defined as follows.

$$F(St) = \frac{\left\langle\hat{q}(St)\right\rangle/Q_o}{u_a'/U_o} \tag{6.17}$$

Where, the numerator now represents the heat release rate at the forcing frequency, expressed as the Strouhal number (St). The denominator represents the amplitude of the coherent forcing component at the driving frequency, ε_a. From eq.(6.16), the total transfer function can be written as two separate contributions as below,

$$F(St) = F_L(St) + F_T(St)\varepsilon_T^2 \tag{6.18}$$

The first term in the above represents the *linear* heat release transfer function for the laminar flame similar to the results derived in Preetham et al.[30]. The second term is the correction to the linear transfer function due to the presence of background turbulence. From eq.(6.16), F_T can be written as follows,

$$F_T\left(St\right)=\frac{2}{\left(R^2-r_f^2\right)}\int_{r_f}^{R}dr\ r\left(\begin{array}{l}\dfrac{\sin^2\gamma}{r^2}\left\langle\dfrac{\partial\zeta_{1t}}{\partial\theta}\dfrac{\partial\hat{\xi}_{2ct}}{\partial\theta}\right\rangle-\dfrac{\cos\gamma\sin^3\gamma}{2r^2}\left\langle\left(\dfrac{\partial\zeta_{1t}}{\partial\theta}\right)^2\right\rangle\dfrac{\partial\hat{\xi}_{1c}}{\partial r}\\ -\dfrac{3}{2}\cos\gamma\sin^5\gamma\dfrac{\partial\hat{\xi}_{1c}}{\partial r}\left\langle\left(\dfrac{\partial\zeta_{1t}}{\partial r}\right)^2\right\rangle\\ +\sin^4\gamma\left(\left\langle\dfrac{\partial\zeta_{1t}}{\partial r}\dfrac{\partial\hat{\xi}_{2ct}}{\partial r}\right\rangle+\dfrac{\partial\hat{\xi}_{1c}}{\partial r}\left\langle\dfrac{\partial\zeta_{2t}}{\partial r}\right\rangle\right)+\cos\gamma\sin\gamma\left\langle\dfrac{\partial\hat{\xi}_{3ctt}}{\partial r}\right\rangle\end{array}\right)$$

(6.19)

where, the caret, '^', represents the Fourier transform.

The ensemble averages in the second term on the RHS of the above are in general non-zero. For example, eq. (6.9) yields,

$$\zeta_{1t}\left(r,\theta,t\right)=\frac{1}{\cos\gamma\sin^2\gamma}\int_{r_f}^{r}d\eta_1\ f_n\left(\eta_1,\theta,\eta_1-r_f,t-\frac{r-\eta_1}{\cos\gamma\sin\gamma}\right)\qquad(6.20)$$

This yields in turn, the following (see Appendix D),

$$\left\langle\left(\frac{\partial\zeta_{1t}}{\partial r}\right)^2\right\rangle=\frac{1}{\cos^2\gamma\sin^4\gamma}+\frac{2}{\cos^3\gamma\sin^5\gamma}\int_{r_f}^{r}d\eta_1\left.\frac{\partial R_{nn}\left(\eta_1,r,\theta,\theta,\left(\eta_1-r_f\right)\cot\gamma,\left(r-r_f\right)\cot\gamma,\tau\right)}{\partial\tau}\right|_{\tau=\frac{\left(r-\eta_1\right)}{\cos\gamma\sin\gamma}}$$
$$-\frac{1}{\cos^4\gamma\sin^6\gamma}\int_{r_f}^{r}\int_{r_f}^{r}d\eta_1 d\eta_2\left.\frac{\partial^2 R_{nn}\left(\eta_1,\eta_2,\theta,\theta,\left(\eta_1-r_f\right)\cot\gamma,\left(\eta_2-r_f\right)\cot\gamma,\tau\right)}{\partial\tau^2}\right|_{\tau=\frac{\left(\eta_2-\eta_1\right)}{\cos\gamma\sin\gamma}}$$

(6.21)

where, R_{nn} is the normal-normal correlation function of the velocity fluctuations defined in Appendix E. Similar results can be derived for each of the correlations in eq. (6.16) (see Appendix D).

Thus, from eq. (6.19) it is clear that turbulence does not behave as additive noise i.e. it changes the ensemble averaged heat release response amplitude, due to the presence of kinematic coupling. Physically, this kinematic coupling occurs because of *non-linearities*

in flame surface kinematics as follows. First, the flame surface at each point is advected to new locations by the net local velocity field (coherent + turbulent) any instant of time. Thus, the velocities on the LHS of eq. (6.2) are themselves functions of the instantaneous flame position, $\zeta(r,\theta,t)$. Second, kinematic restoration causes eventual destruction of wrinkles induced on the flame causing the net global area fluctuation amplitude to change. These processes clearly result in the coupling between the response of the flame to coherent forcing and turbulence fluctuations. Products between ensemble averaged turbulent contribution terms and laminar forcing terms in eq. (6.19) control the influence of kinematic coupling. All these terms can be evaluated in terms of spatio-temporal correlation functions between various turbulent velocity components as shown in appendix D.

The analysis presented thus far is exact in the sense that no ad-hoc assumptions of equivalent propagation speeds have been made. However, the drawback of the above approach is that it requires knowledge of the nominal flame surface shape in the absence of acoustic forcing in *addition* to the statistical properties of the turbulent velocity field, in order to determine the turbulence correction to the heat release transfer function. While it is possible to ascertain the latter in practical situations, defining a "nominal" flame surface becomes problematic because the definition of the equivalent "laminar" flow is itself is problematic. The presence of a temperature jump across the flame sheet further exacerbates this difficulty as the mean flow velocity upstream of the flame is modified. Hence, a modeling approach must be introduced in order to determine the heat release transfer function in practical situations. The utility of the present formulation, apart from providing insight into the fundamental characteristics of heat release response, is to

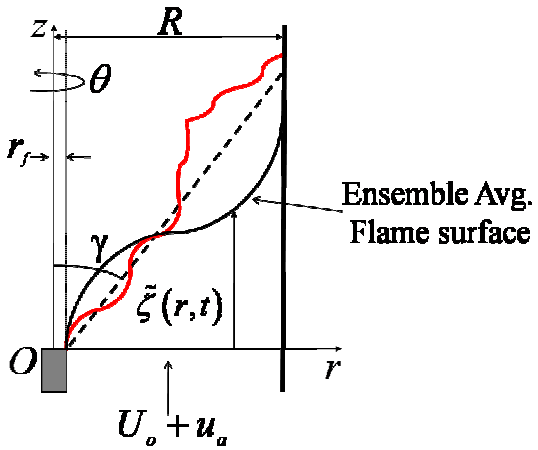

Figure 6-3: Schematic of the investigated geometry showing the ensemble averaged flame surface.

provide a baseline against which the fidelity of different modeling approaches to determining the heat release response for the present canonical configuration can be determined. This will be discussed in the next section.

6.2 Flame response modeling

The *mean* flame surface shape, i.e. the average shape of the flame in the presence of turbulence, is readily accessible from either experiments or computational approaches based on the Reynolds Averaged Navier-Stokes equations (RANS). As discussed in chapter 1, a local "turbulent" propagation (displacement) speed and local consumption speed can be defined at all points on this mean surface. Thus, it is possible to use the G-equation approach to derive a kinematic

equation for the mean flame surface in terms of the ensemble averaged velocity field and the local displacement speed. The heat release response can then be evaluated using the flame surface shape obtained from the above equation and the local consumption speed. This modeling approach is a generalization past modeling approaches for the linear heat

release response transfer function of an axis-symmetric center-body stabilized turbulent flame [31-33].

Let the ensemble averaged flame surface shape at any time relative to the start of the acoustic forcing cycle be denoted by $\tilde{\zeta}(r,t)$ as shown in fig. 6-3. A kinematic equation governing its dynamics in the mean flow field may now be written analogously to eq. (6.3) as follows,

$$\frac{\partial \tilde{\zeta}}{\partial t} + \tilde{u}\frac{\partial \tilde{\zeta}}{\partial r} - \tilde{v} = -f_T(r)\sin\gamma\sqrt{1+\left(\frac{\partial \tilde{\zeta}}{\partial r}\right)^2} \tag{6.22}$$

Where, the non-dimensionalization scheme used in eq. (6.3) has been retained. The '~' represents ensemble averaging. The function f_T on the RHS represents the local propagation velocity of the ensemble averaged flame surface relative to the ensemble averaged upstream flow of reactants, normalized by the laminar flame speed s_L. Thus, this now is a "local" displacement speed. Due to the spatially isotropic nature of the turbulence field in this analysis, the ensemble averaged azimuthal velocity component is identically zero. Further, all mean and ensemble averaged quantities are independent of θ due to axis-symmetry.

The ensemble averaged velocity field can be determined from eq. (6.4) as follows,

$$\begin{aligned}\tilde{u}\left(r,\tilde{\zeta},t\right) &= \frac{1}{2}\frac{KSt}{\Lambda}\varepsilon_a r\sin\left[\frac{St}{\Lambda}\left(K\tilde{\zeta}-t\right)\right]\\ \tilde{v}\left(r,\tilde{\zeta},t\right) &= 1+\varepsilon_a\cos\left[\frac{St}{\Lambda}\left(K\tilde{\zeta}-t\right)\right]\end{aligned} \tag{6.23}$$

Next, an expansion for $\tilde{\zeta}(r,t)$ can be introduced as follows,

$$\tilde{\zeta}(r,t) = \tilde{\zeta}_o(r) + \varepsilon_a\tilde{\zeta}_1(r,t) + O\left(\varepsilon_a^2\right) \tag{6.24}$$

Using the above expansion in eq. (6.22) yields the following system,

$$-1+f_T(r)\sin\gamma\sqrt{1+\left(\frac{d\tilde{\xi}_o}{dr}\right)^2}=0 \tag{6.25}$$

and

$$\frac{\partial\tilde{\xi}_1}{\partial t}+\frac{f_T(r)\left(d\tilde{\xi}_o/dr\right)\sin\gamma}{\sqrt{1+\left(d\tilde{\xi}_o/dr\right)^2}}\frac{\partial\tilde{\xi}_1}{\partial r}=\cos\left[\frac{St}{\Lambda}\left\{t-K\tilde{\xi}_o(r)\right\}\right]+\left(\frac{KSt}{2\Lambda}\frac{d\tilde{\xi}_o}{dr}\right)r\sin\left[\frac{St}{\Lambda}\left\{t-K\tilde{\xi}_o(r)\right\}\right] \tag{6.26}$$

Also, the flame attachment boundary condition yields,

$$\tilde{\xi}_1(0,t)=0 \tag{6.27}$$

Next, eq. (6.26) can be solved as follows. Writing eq. (6.26) in terms in Fourier space at the Strouhal number St/Λ yields,

$$\frac{d\hat{\tilde{\xi}}_1}{dr}-\frac{i(St/\Lambda)\sqrt{1+\left(d\tilde{\xi}_o/dr\right)^2}}{f_T(r)\left(d\tilde{\xi}_o/dr\right)\sin\gamma}\hat{\tilde{\xi}}_1=e^{\frac{iKSt\tilde{\xi}_o(r)}{\Lambda}}\left(1+i\left(\frac{KSt}{2\Lambda}\frac{d\tilde{\xi}_o}{dr}\right)r\right)\frac{\sqrt{1+\left(d\tilde{\xi}_o/dr\right)^2}}{f_T(r)\left(d\tilde{\xi}_o/dr\right)\sin\gamma} \tag{6.28}$$

Solving the above using the method of integrating factors yields,

$$\hat{\tilde{\xi}}_1(r,St)=e^{H_1(r)}\int_{r_f}^{r}d\eta_1\,e^{-H_1(\eta_1)}P(\eta_1,St) \tag{6.29}$$

Where,

$$H(r,St)=\frac{i(St/\Lambda)\sqrt{1+\left(d\tilde{\zeta}_o/dr\right)^2}}{f_T(r)\left(d\tilde{\zeta}_o/dr\right)\sin\gamma}$$

$$H_1(r,St)=\int_{r_f}^{r}d\eta\,H(\eta,St) \tag{6.30}$$

$$P(r,St)=e^{\frac{iKSt\tilde{\zeta}_o(r)}{\Lambda}}\left(1+i\left(\frac{KSt}{2\Lambda}\frac{d\tilde{\zeta}_o}{dr}\right)r\right)\frac{\sqrt{1+\left(d\tilde{\zeta}_o/dr\right)^2}}{f_T(r)\left(d\tilde{\zeta}_o/dr\right)\sin\gamma}$$

The above can be rewritten using eq. (6.25) as follows,

$$H(r,St)=\frac{i(St/\Lambda)}{f_T(r)\sin\gamma\sqrt{1-\left(f_T(r)\sin\gamma\right)^2}}$$

$$H_1(r,St)=\int_{r_f}^{r}d\eta\,H(\eta,St) \tag{6.31}$$

$$P(r,St)=e^{\frac{iKSt\tilde{\zeta}_o(r)}{\Lambda}}\left(1+i\left(\frac{KSt}{2\Lambda}\frac{\sqrt{1-\left(f_T(r)\sin\gamma\right)^2}}{f_T(r)\sin\gamma}\right)r\right)\frac{1}{f_T(r)\sin\gamma\sqrt{1-\left(f_T(r)\sin\gamma\right)^2}}$$

Next, the net heat release rate from the flame (normalized by the mean heat release rate of the unforced flame) can be written in terms of a local consumption speed, $f_c(r)$ (normalized by laminar flame speed s_L) as,

$$\tilde{q}(t)=\frac{\int_{r_f}^{R}dr\;rf_c(r)\sqrt{1+\left(\frac{\partial\tilde{\zeta}}{\partial r}\right)^2}}{\int_{r_f}^{R}dr\;rf_c(r)\sqrt{1+\left(d\tilde{\zeta}_o/dr\right)^2}} \tag{6.32}$$

The above represents the significant difference between the present modeling approach and past approaches that assume either $f_c(r)=f_T(r)$ [31, 32] or $f_c(r)$=constant (You *et*

al [33]). It will be shown shortly that in general both of these assumptions are not true. Expanding the above as series in ε_a yields,

$$\tilde{q}(t) = 1 + \left(\frac{\int_{r_f}^{R} dr\ rf_c(r) \left(\left(\frac{d\tilde{\zeta}_o}{dr} \right) \Big/ \sqrt{1 + \left(d\tilde{\zeta}_o / dr \right)^2} \right) \frac{\partial \tilde{\zeta}_1}{\partial r}}{\int_{r_f}^{R} dr\ rf_c(r) \sqrt{1 + \left(d\tilde{\zeta}_o / dr \right)^2}} \right) \varepsilon_a \tag{6.33}$$

Hence the heat release transfer function can be written in Strouhal number space as,

$$\tilde{F}(St) = \frac{\int_{r_f}^{R} dr\ rf_c(r) \left(\left(\frac{d\tilde{\zeta}_o}{dr} \right) \Big/ \sqrt{1 + \left(d\tilde{\zeta}_o / dr \right)^2} \right) \frac{\partial \hat{\tilde{\zeta}}_1}{\partial r}}{\int_{r_f}^{R} dr\ rf_c(r) \sqrt{1 + \left(d\tilde{\zeta}_o / dr \right)^2}} \tag{6.34}$$

where, '^' represents the value of the Fourier transform of the corresponding quantity. Again, using eq. (6.25) yields,

$$\tilde{F}(St) = \frac{\int_{r_f}^{R} dr\ r \sin\gamma f_c(r) \sqrt{1 - \left(f_T(r) \sin\gamma \right)^2}\ \frac{\partial \hat{\tilde{\zeta}}_1}{\partial r}}{\int_{r_f}^{R} dr\ r \left(f_c(r) / f_T(r) \right)} \tag{6.35}$$

Finally, the derivative of the unsteady flame shape in the above can be evaluated by differentiating eq. (6.29) w. r. t. *r* to yield the following,

$$\frac{d\hat{\tilde{\zeta}}_1}{dr} = P(r, St) + H(r, St) e^{H_1(r, St)} \int_{r_f}^{r} d\eta_1\, e^{-H_1(\eta_1, St)} P(\eta_1, St) \tag{6.36}$$

Thus, for specified local displacement speed and local consumption speed, the heat release transfer function can be evaluated from eqs. (6.35) and (6.36). Next, a model for

$f_c(r) = f_T(r)$ can be derived from the exact asymptotic analysis presented in the previous section as follows.

The mean unforced flame geometry can be specified using the exact asymptotic analysis developed in the previous section from the terms that are zeroth order in forcing amplitude, ε_a as follows (see eq. (6.5)),

$$\tilde{\zeta}_o(r) = (r - r_f)\cot\gamma + \varepsilon_T^2 \langle \zeta_{2t}(r,\theta,t) \rangle + O(\varepsilon_T^3) \tag{6.37}$$

Next, eq. (6.25) represents the kinematic equation that determines the rate of propagation of the above mean flame surface into the upstream reactants, $f_T(r)$ i.e. the local displacement speed. Thus, using eq. (6.37) in eq. (6.25) and retaining term upto $O(\varepsilon_T^2)$ yields,

$$f_T(r) = 1 - \cos\gamma \sin\gamma \left\langle \frac{\partial \zeta_{2t}}{\partial r} \right\rangle \varepsilon_T^2 \tag{6.38}$$

Equation (6.10) together with eq. (6.38) yields,

$$f_T(r) = 1 + \left\{ \begin{array}{l} \frac{1}{r}\left\langle f_\theta\left(r,\theta,(r-r_f)\cot\gamma,t\right)\frac{\partial \zeta_{1t}}{\partial \theta}\right\rangle + \left\langle f_u\left(r,\theta,(r-r_f)\cot\gamma,t\right)\frac{\partial \zeta_{1t}}{\partial r}\right\rangle \\ + \frac{\sin^2\gamma}{2r^2}\left\langle \left(\frac{\partial \zeta_{1t}}{\partial \theta}\right)^2\right\rangle + \sin^4\gamma\left\langle \left(\frac{\partial \zeta_{1t}}{\partial r}\right)^2\right\rangle - \left\langle \frac{\zeta_{1t}(r,\theta,t)}{\sin\gamma}\frac{\partial f_n}{\partial z}\bigg|_{(r,\theta,z=(r-r_f)\cot\gamma,t)}\right\rangle \end{array} \right\} \varepsilon_T^2$$

(6.39)

Next, the *instantaneous* heat release per unit area of the flame is given by,

$$\frac{q(r,\theta,t)}{\rho s_L h_R} = \sqrt{1 + \frac{1}{r^2}\left(\frac{\partial \zeta}{\partial \theta}\right)^2 + \left(\frac{\partial \zeta}{\partial r}\right)^2} \tag{6.40}$$

Using the expansion, eq. (6.5) in the above and ensemble averaging yields,

$$\frac{\tilde{q}_o(r)}{\rho s_L h_R} = \frac{1}{\sin\gamma} + \left\{ \frac{\sin\gamma}{2r^2} \left\langle \left(\frac{\partial \zeta_{1t}}{\partial \theta} \right)^2 \right\rangle + \frac{1}{2} \sin^3\gamma \left\langle \left(\frac{\partial \zeta_{1t}}{\partial r} \right)^2 \right\rangle + \cos\gamma \left\langle \frac{\partial \zeta_{2t}}{\partial r} \right\rangle \right\} \varepsilon_T^2$$

(6.41)

Where, $\tilde{q}_o(r)$ is the mean heat release rate per unit area for the mean flame surface shape given by eq. (6.37). From the discussion on local consumption speed in the previous chapter, the mean heat release rate can be written in terms of local consumption speed $f_c(r)$ as follows,

$$\frac{\tilde{q}_o(r)}{\rho h_R s_L} = f_c(r) \sqrt{1 + \left(\frac{d\tilde{\zeta}_o}{dr} \right)^2} \tag{6.42}$$

Thus, using eq. (6.37) together with eq. (6.41) in the above and retaining terms upto $O(\varepsilon_T^2)$ yields,

$$f_c(r) = 1 + \left\{ \frac{\sin^2\gamma}{2r^2} \left\langle \left(\frac{\partial \zeta_{1t}}{\partial \theta} \right)^2 \right\rangle + \frac{1}{2} \sin^4\gamma \left\langle \left(\frac{\partial \zeta_{1t}}{\partial r} \right)^2 \right\rangle + \cos\gamma \sin\gamma \left\langle \frac{\partial \zeta_{2t}}{\partial r} \right\rangle \right\} \varepsilon_T^2 \tag{6.43}$$

And using eq. (6.10) in the above yields the following result,

$$f_c(r) = 1 + \left\{ \begin{array}{l} -\frac{1}{r} \left\langle f_\theta\left(r, \theta, (r - r_f)\cot\gamma, t\right) \frac{\partial \zeta_{1t}}{\partial \theta} \right\rangle - \left\langle f_u\left(r, \theta, (r - r_f)\cot\gamma, t\right) \frac{\partial \zeta_{1t}}{\partial r} \right\rangle \\ + \left\langle \frac{\zeta_{1t}(r, \theta, t)}{\sin\gamma} \frac{\partial f_n}{\partial z}\bigg|_{\left(r, \theta, z = (r - r_f)\cot\gamma, t\right)} \right\rangle \end{array} \right\} \varepsilon_T^2$$

(6.44)

From the results for various ensemble averages in terms of spatio-temporal turbulence velocity correlations presented in appendix D, it is clear that f_c and f_T are different from each other.

The present heat release transfer function model assumes that the spatial distribution of local displacement and consumption speeds does not change over an acoustic cycle. This is not true in general due to kinematic coupling because acoustic forcing introduces coherent wrinkling component on the flame surface resulting in a coherent fluctuation component of ensemble averaged flame slope/burning area. Added to this is the influence of non-locality. Thus, the local consumption speed and displacement speeds will now have a coherent time varying component as well. As such, eqs. (6.39) and (6.44) represent the $O\left(\varepsilon_a^0\right)$ contribution to the local displacement and consumption speeds respectively in an expansion in terms of ε_a for these quantities. However, the analysis presented in the previous section for the turbulence correction to the laminar response *implicitly* captures this time variation of local consumption and displacement speeds within its framework as it includes all leading order kinematic coupling terms and non-local flame response.

Explicit results for the present turbulent flame speed models have been obtained using the results presented in appendix D and the spatio-temporal correlations derived using the formulation in appendix F together with the longitudinal correlation specified in chapter 3 (eq. (3.13)). Explicit results for the total transfer function have been obtained for the local consumption/displacement speed models given in eqs. (6.39) and (6.44). Therefore, a comparison between that result and the flame response model developed in the present section will serve to ascertain the relative importance of the coherent variation in turbulent displacement and consumption speeds due to non-locality in determining the overall flame response.

The results developed in this chapter present a description of the heat release response of turbulent flames to acoustic forcing in the limit of low intensity turbulence. These results will be discussed in the next chapter.

Chapter 7

Forced flame response - Results

This chapter presents the principal results from the analysis of the heat release response of turbulent premixed flames to acoustic forcing. The discussion is divided into two sections. The first section presents results on the general characteristics of turbulent flame response to acoustic forcing contrasted with the corresponding features in the case of a laminar flame. It is shown that the *ensemble averaged linear* response in the forced turbulent flame scenario is modified by turbulence and therefore, turbulence does not behave like additive noise. Further, the characteristics of heat release response change significantly from the corresponding laminar characteristics when the length scale of acoustic forcing is of the order of the integral length scale, L_{11}. This is because of increased influence of kinematic coupling between the response of the flame to coherent forcing and random turbulence fluctuations respectively. This is manifested as a net increase in transfer function gain. These results are presented in the following section titled “Flame response characteristics”. The section titled “Modeling approach” presents comparisons between models for turbulent flame response with the results of the exact analysis.

7.1 Flame response characteristics

The analysis in the previous chapter showed that the presence of a spatio-temporally random velocity field results in a non-zero leading order correction to the linear transfer function. This is because of non-linear coupling between coherent flame surface

perturbations induced by the acoustic forcing and random wrinkling induced by the turbulence. The leading order turbulence correction term can be determined from the expression in eq. (6.19). For the spatio-temporal correlation functions used in this work, it was not possible to analytically determine a closed form solution for the above turbulence correction. Hence, a numerical integration technique using a 30 point Gauss-Legendre quadrature was adopted. The change in the value of the magnitude and phase of the leading order transfer function correction at the highest value of Strouhal number, St, between further successive refinements was less than 10^{-5}. All lengths in this chapter will be presented as non-dimensional numbers normalized by the integral length scale, L_{11}.

From the discussion in the context of local consumption speed in chapter 5, it was observed that flame surface kinematics in the near-field of the flame-holder are well described by linear theory. The same result applies *qualitatively* in the present axis-symmetric case as well. The difference is only in the quantitative aspect of the results. The value of r_f was chosen to be 1.0. The upper limit of the outer most integral in eq. (6.19) is the radius of the combustor (assumed circular in cross-section) which in the framework of this analysis is a specified parameter. This was assumed as R = 2.0. Thus for a specified flame angle of γ=45^{o} the nominal height of the flame is given by Λ = 1.0. For the values of R, r_f and γ assumed here, the slant length of the nominal flame surface is ~ 2.8. Thus the results suggest that at low u'/s_L values, the dynamics of the flame surface are well described by leading order kinematic equations developed in the previous chapter.

The characteristics of linear flame response in the laminar limit, within the framework of the simplifying assumptions in this work, were discussed extensively by Preetham *et al* [30]. The principal conclusions of that work will be reviewed here to provide a background for the discussion on turbulent flame response. The net flame surface slope at any point on the flame surface is a resultant of superposition of contributions from a particular solution that depends on

spatial non-uniformity of the flow-field and boundary condition generated terms. Thus the linear transfer function in the laminar limit can be decomposed into two terms resulting from each of the above two contributions to the net flame response. The amplitude and phase of these two contributions are characterized by a reduced Strouhal number $St_2 = St/\cos^2\gamma$ and $K\cos^2\gamma$ which is the ratio of the mean tangential velocity to the flame surface to the propagation velocity of vortical structures projected along the mean flame surface. Thus, at different Strouhal numbers, the net transfer function is a result of constructive and destructive interference between the above two transfer function components. Thus, it was shown for certain values of $K\cos^2\gamma$ the transfer function gain for the present axis-symmetric flame configuration exceeds unity and can also exhibit non-monotonic behaviour such as the appearance of local minima in the response, i.e. frequencies at which the transfer function amplitude reaches a minimum. The underlying physical mechanism that causes this behaviour is the non-locality phenomenon described in chapters 4 and 5.

Figure 7-1 shows the variation of the total transfer function, i.e. $F_L(St_2) + F_T(St_2)\varepsilon_T^2$ (see eq. (6.18)) with St_2 for typical values of convection speed ratio, K. Also shown is the

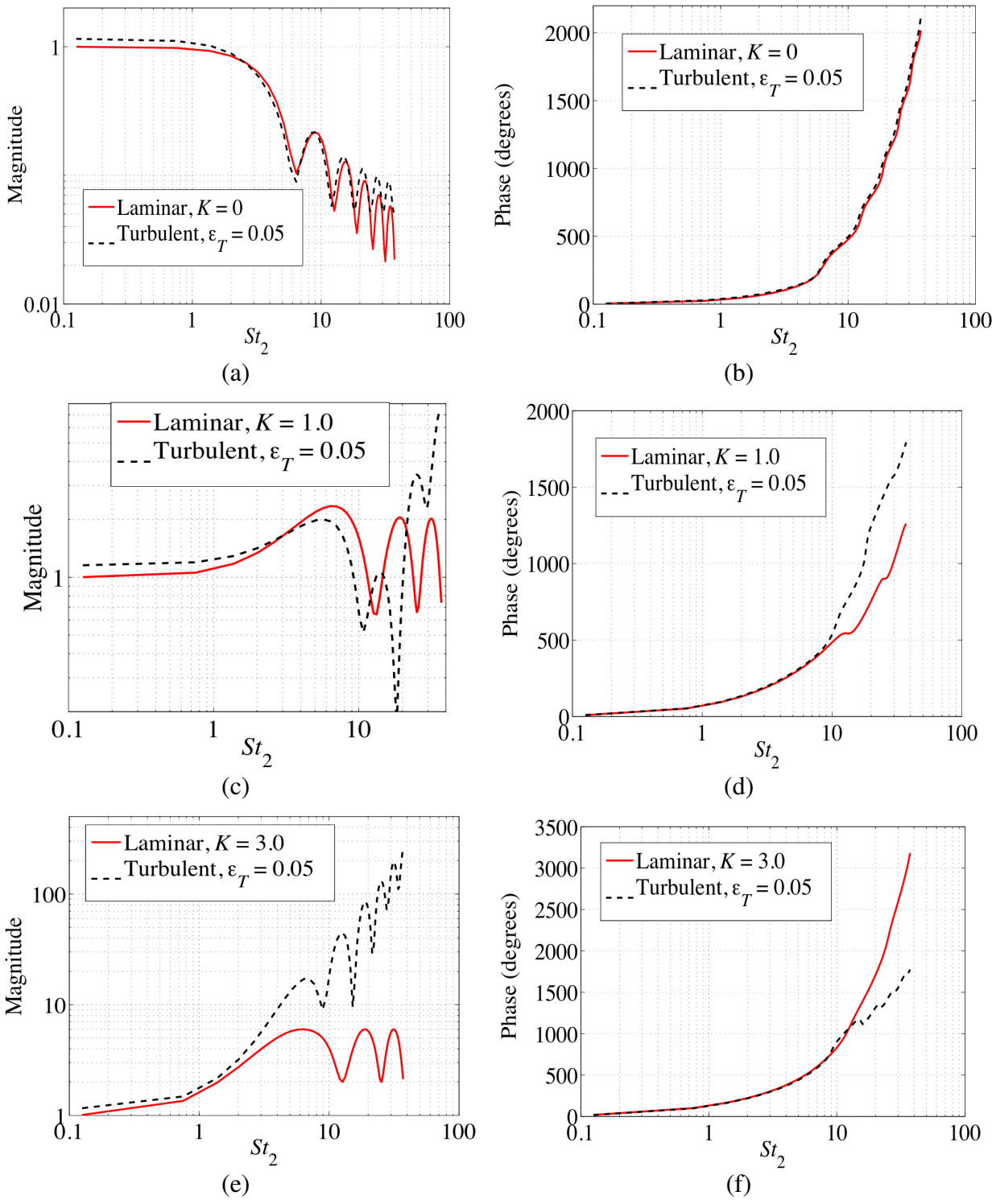

Figure 7-1: Variation of total transfer function magnitude and phase with Strouhal number for typical values of *K*= (a)-(b) 0, (c)-(d) 1.0 and (e)-(f) 3.0. Also shown for reference in each case is the corresponding laminar transfer function. Flame angle γ=45°.

corresponding variation of the laminar transfer function for reference in each case. The turbulence intensity $\varepsilon_T = u_T'/U_o$ = 0.05. Note that the variation of the transfer function magnitude and phase of the turbulent case are qualitatively similar to the corresponding laminar variations at low to moderate St_2 values. This qualitative behaviour is due to the same reasons for non-monotonic behavior of laminar flame response magnitude that were discussed in Preetham et al [30] viz.,

the net flame response is a superposition of responses from the boundary condition term and a spatial flow non-uniformity term as a result of non-locality.

The *quantitative* difference in the magnitude between laminar and turbulent cases (e.g. $0 < St_2 < 20$ for $K = 1.0$) is because of kinematic coupling between the response of the flame surface to coherent and random velocity fluctuations and non-locality that now cause the burning rate variation along the flame to change from its unforced value. It shown in appendix E that for $K > 0$, this quantitative leading order turbulence correction is characterized by the ratio of the length scale of turbulence to that of the coherent acoustic perturbations. This can be defined as a turbulence Strouhal number $St_{c,Turb} = fL_{11}/u_c = St_2\left(K\cos^2\gamma/2\pi\Lambda\right)$.

Next, note that as $St_2 \to 0$, each of the magnitude curves in fig. 7-1 start from a small non-unity value. With increasing St_2 the magnitude and phase vary in a qualitatively similar manner as that of the corresponding laminar transfer function. This is at variance with the analysis of Polifke and Lawn [60] who suggest that the heat release transfer function magnitude should reach unity as $St_2 \to 0$, for perfectly premixed flames. They give the following relation (dimensional form),

$$\frac{\delta\dot{Q}}{\dot{Q}} = \frac{\delta\dot{m}_f}{\dot{m}_f} = \frac{\delta u_B}{u_B} \tag{7.1}$$

where, $\dot{m}_f$ is the global mass burning rate of the flame and u_B is a reference velocity that describes the forcing velocity field. Thus, they conclude that the transfer function magnitude must approach unity as $St_2 \rightarrow 0$ because, $\lim_{St_2 \rightarrow 0}\left\{\left(\delta\dot{Q}/\dot{Q}\right)\Big/\left(\delta u_B/u_B\right)\right\} = 1$. However, the second equality in eq. (7.1) implicitly assumes that the global consumption speed of the flame is unaffected by the presence of coherent forcing. Since the net response of the flame due to the coherent forcing and turbulence fluctuations are kinematically coupled, the coherent response affects the net flame surface wrinkling due to turbulence fluctuations. Hence, global/local consumption speeds will vary in a coherent unsteady manner when the flame is acoustically forced. Therefore, writing (in dimensional form) $\dot{m}_f = \rho_u S_{T,GC}(t) A_{ref}(t)$, where, A_{ref} is the unsteady ensemble averaged reference area, $S_{T,GC}$ is the global consumption speed of the flame in the presence of acoustic forcing and ρ_u is the unburnt gas density, eq. (7.1) can be rewritten as ,

$$\frac{\delta\dot{Q}}{\dot{Q}} = \frac{\delta\dot{m}_f}{\dot{m}_f} = \frac{\delta A_{ref}}{A_{ref}} + \frac{\delta S_{T,GC}}{S_{T,GC}} \tag{7.2}$$

Dividing the above expression by $\delta u_B/u_B$ yields,

$$\frac{\delta\dot{Q}/\dot{Q}}{\delta u_B/u_B} = \frac{\delta A_{ref}/A_{ref}}{\delta u_B/u_B} + \frac{\delta S_{T,GC}/S_{T,GC}}{\delta u_B/u_B} \tag{7.3}$$

The first term on the RHS approaches unity in the limit of $St_2 \rightarrow 0$ (i.e., low-frequency limit). However, the second term does not do so in general because of the presence of kinematic coupling between the coherent wrinkling and the random wrinkling as will be

shown later. This point can be seen from fig 7-2a-b that shows the variation of the magnitude of the turbulence correction and its phase relative to the laminar response with St_2. The various $|F_T|$ curves tend to a constant non-zero value as $St_2 \rightarrow 0$. Note also from fig. 7-2a that the phase of this correction term relative to the laminar forcing is $< 90^o$ for all values of K as $St_2 \rightarrow 0$. This means that the contributions to the total transfer function due to the laminar response and due to the leading order turbulence correction add constructively, resulting in the magnitude of the total transfer function being > 1 as $St_2 \rightarrow 0$.

Next, fig. 7-2a shows that $|F_T|$ decreases with increasing St_2 for all values of K. This can be explained by consideration of kinematic restoration effects that cause destruction of small length scale wrinkles induced on the coherent flame surface wrinkling component due to turbulence fluctuations as shown schematically in fig. 7-3. Note first that the laminar analysis of Preetham el al [30] shows that when $K > 0$, the wavelength of

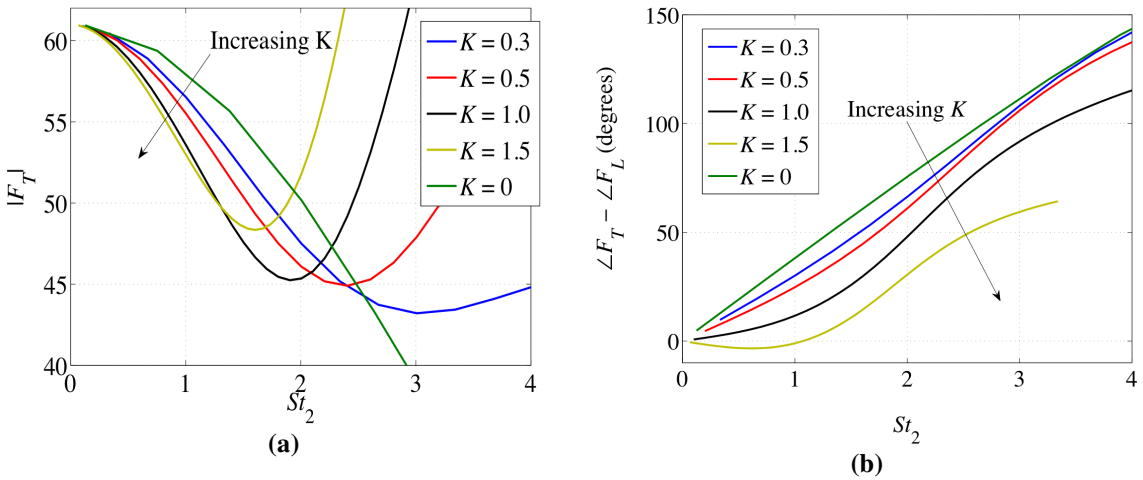

Figure 7-2: Variation of the leading order turbulence correction term with Strouhal number (a) magnitude and (b) phase. Flame angle, $\gamma = 45^o$ and flame length, Λ=1.

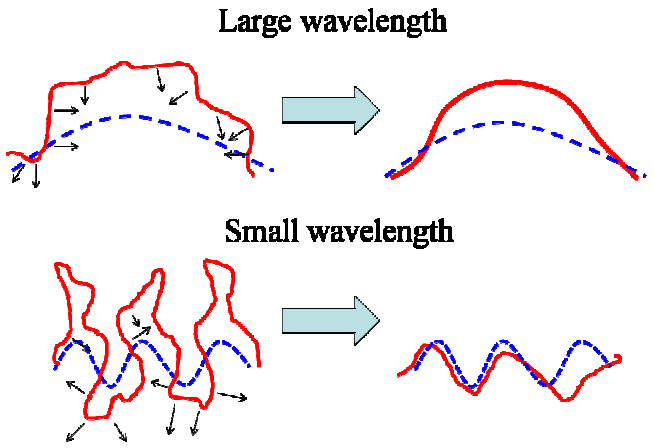

Figure 7-3: Schematic showing the influence of the wavelength of coherent forcing relative to the turbulent scales on burning area destruction. The solid curves on the left show schematically the resultant wrinkling if there were no kinematic restoration. The broken curves show schematically, the base-line coherent wrinkling. The small arrows show the direction of flame surface propagation.

flame surface wrinkling induced on the flame by coherent velocity fluctuations is controlled by u_c/f . This is shown schematically by the broken lines on both sides of the large arrows in fig. 7-3. Due to the presence of turbulence, additional small length scale wrinkling is induced on this coherent baseline which, in the absence of kinematic restoration would increase flame wrinkling amplitudes as shown by the corresponding solid lines to the left of the large arrows.

Next, due to flame surface propagation (i.e. kinematic restoration), the short length scale high amplitude wrinkles (bottom left, fig. 7-3) are destroyed faster than wrinkles of comparable amplitude and length scale (top left, fig. 7-3) as the whole flame surface feature travels along the flame surface (due to non-locality, see figures to the right of the large arrows in fig. 7-3), over a fixed time interval. Thus, kinematic restoration prevents the net local burning area fluctuation from deviating significantly from the laminar baseline value at smaller coherent wavelengths (bottom right of fig. 7-3). Hence, the magnitude of the leading order turbulence correction to the laminar flame response will

decrease with increasing St_2 as shown by the curves in fig. 7-2a. Further, for a given value of St_2, the coherent forcing wavelength decreases with increasing K since $u_c/f = U_o/(Kf)$. Thus, by the same argument as given above, the magnitude of the turbulence correction must decrease with increasing K as shown in fig. 7-2a. With further increase in St_2, the wavelength of the coherent forcing component $(=u_c/f)$ decreases until it becomes comparable to the length scales of turbulence fluctuations. Thus, the flame is now excited by a randomly varying velocity field with an oscillation amplitude at a single length scale corresponding to the length scale (u_c/f) of coherent forcing. From the standpoint of flame wrinkling, this results in large amplitude wrinkles being generated over small wavelengths whose destruction time decreases with decreasing wavelength, i.e increasing St_2. Hence, the $O(\varepsilon_T^2)$ kinematic restoration terms included in F_T are insufficient to suppress this increase in area resulting in the increase in $|F_T|$ with increasing St_2. This result can be seen explicitly from a high frequency limit analysis of

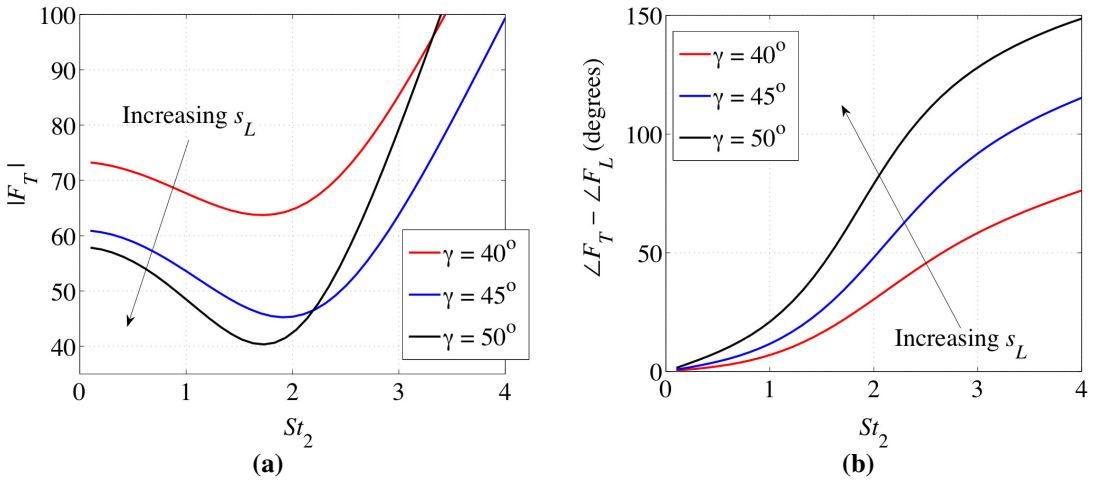

Figure 7-4: Variation of the (a) Magnitude and (b) phase relative to laminar response of the leading order turbulence correction for different flame angles γ, K = 1.0, Λ = 1.

F_T in Appendix E.

Next, the above reasoning suggests that the turbulence correction magnitude must reduce as the *laminar* flame speed increases as a higher laminar flame speed causes wrinkles to be destroyed more efficiently. Note that within the framework of the present analysis, a change in flame angle γ for a given value of K implies a change in the value of s_L because the value of K fixes the mean flow velocity U_o. Figure 7-4 shows the variation of the turbulence correction magnitude and phase (relative to the laminar correction) for three different values of flame angle. By definition, an increase γ implies an increase in laminar flame speed (see fig. 6-1). Thus, it is clear from fig. 7-4 that $|F_T|$ reduces with increasing s_L. Note also that the phase relative to the laminar correction is $< 90^o$ over a larger range of St_2 at smaller s_L values. The implication of this result is that the change in the ensemble averaged value of heat release response due to turbulence would be more pronounced in lean premixed systems.

Next, note that for K = 0 case, fig. 7-5 shows that, the increase in $|F_T|$ occurs at a much larger value of St_2 even though the wavelength of the coherent forcing $u_c / f \to \infty$ for this case. Preetham et al [30] showed that the length scale of flame wrinkling in this case is controlled by the flame attachment condition. Thus, the length scale of flame wrinkling in the K = 0 case is given by U_o/f. Therefore, the present asymptotic analysis is valid until, $U_o/f \sim L_{11} \Rightarrow St_2 \sim 2\pi\Lambda/\cos^2\gamma$. The vertical line in fig. 7-5 marks this St_2 value for the present choice of parameters. Higher order contributions to the turbulence correction for the $K = 0$ case would become significant at values of St_2 to the right of this

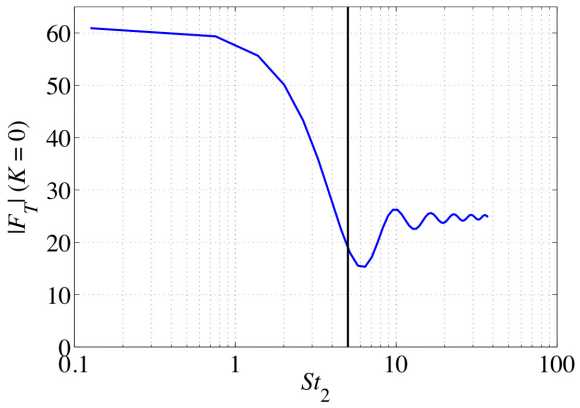

Figure 7-5: Variation of leading order turbulence correction magnitude for K = 0. Flame angle, γ=45^o, and flame length, Λ=1. The vertical line shows the characteristic St_2 value beyond which coherent flame wrinkling wavelength becomes comparable to turbulence length scales.

line. Note that the decrease in $|F_T|$ to the left of this line is because of the same reasons as described for the K > 0 case.

In summary, the results presented in this section show that the total ensemble averaged heat release response transfer function to leading order in turbulence intensity is qualitatively similar, but quantitatively different, from the corresponding baseline laminar transfer function at low to medium St_2. The flame response does not go to unity in the low St_2 limit because of the coherent response of the local/global consumption speeds to acoustic forcing. This is caused by kinematic coupling between coherent flame motions from acoustic forcing and random wrinkling due to turbulence fluctuations in addition to non-locality. This kinematic coupling causes the magnitude and phase of the total turbulent transfer function to differ quantitatively from its laminar baseline value at low to moderate Strouhal numbers. With increasing St_2 and s_L, the decreased destruction time of short wavelength wrinkles causes the magnitude of the correlation function to drop. Beyond a certain critical Strouhal number (dependent on K) the length scale of coherent fluctuations becomes the same as the length scales of the turbulence fluctuations in the

energy containing range. This results in large amplitude wrinkling of the flame surface. Thus, higher order kinematic restoration terms become significant and must be included in order to correctly predict the leading order turbulence correction to the flame transfer function.

7.2 Response modeling

The results of the asymptotic approach presented in the previous section provide useful insight into the fundamental physical processes that characterize the heat release response of turbulent premixed flames. However, in practical situations, it may not always be possible to determine the nominal flame surface shape except for simple configurations as analyzed in this work for the reasons discussed before (see chapter 6 end of response section).

Heat release transfer function predictions have been obtained for two different turbulent flame speed models. The first of these is based on the specification of local displacement and consumption speeds $f_T(r)$ and $f_c(r)$ from eqs. (6.39) and (6.44) respectively. Thus, this approach captures the non-local nature of *unforced* turbulent flame surface motions. The effect of kinematic coupling is not captured. Explicit expressions for eqs. (6.39) and (6.44) can be derived using the expressions presented in appendix D and the spatio-temporal turbulent velocity correlation functions derived using the procedure described in appendix F.

The second model is that of Lipatnikov and Chomiak (referred to as the LC model). The details of the derivation of this model are given in their review paper (ref. [11]). The final expression for the local consumption speed is repeated here for convenience.

$$f_c^{Lip}(r) = \frac{S_o}{s_L}\left\{1 + \frac{T}{t'(r)}\left(e^{-t'(r)/T} - 1\right)\right\} \tag{7.4}$$

Where, $t'(r)$ is a flame development time i.e., the time taken for a fluid particle to reach the flame surface from the burner inlet and T is a turbulent mixing time. The flame development time was determined following the procedure in refs. [31, 32] by first numerically evaluating the following integral (30-point Gauss-Legendre quadrature) to obtain at parametrization $r = r(t')$ (non-dimensional form).

$$r(t') = r_f + \frac{S_o}{s_L}\int_0^{t'} d\tau \left\{1 + \frac{T}{\tau}\left(e^{-\tau/T} - 1\right)\right\} \tag{7.5}$$

The value of S_o/s_L was specified as $0.09/\sin\gamma = 0.13$ following [31]. This value was

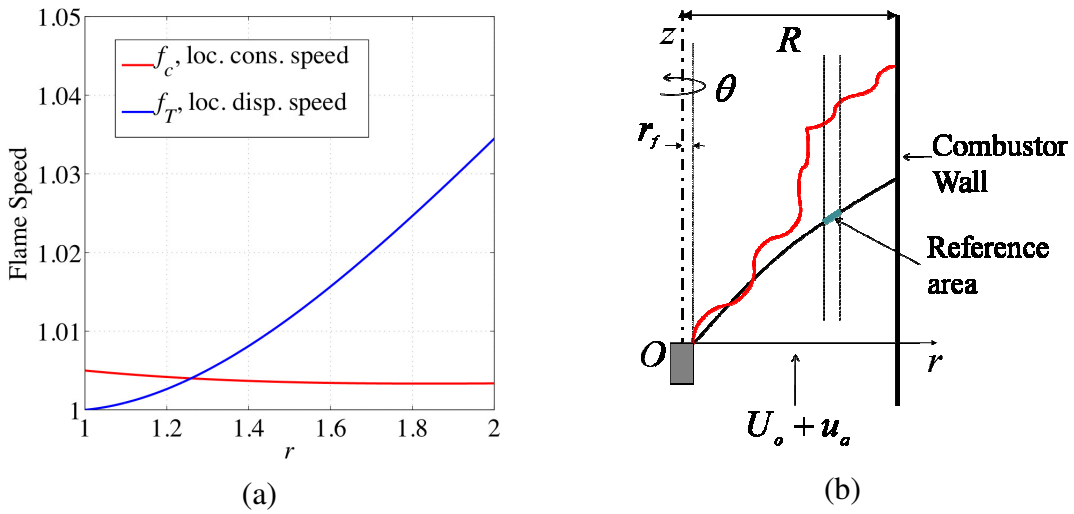

(a) (b)

Figure 7-6: a) Variation of local consumption and displacement speeds from the non-local model and b) schematic showing the reference area on the unforced mean surface used to define $f_c(r)$, $\mathcal{E}_T$ = 0.05, γ= 45° and Λ=1.

obtained by Dowling[22] for the present configuration from the theoretical analysis of Bloxsidge et al [61]. The mixing time T was specified as $l_{E,\max}/\varepsilon_T = \sqrt{2\pi}/0.05 \sim 50$. Thus, the radial variation of $f_c^{Lip}(r)$ can be specified in parametric form using eq. (7.5) in terms of the parameter t'. Finally, in keeping with the assumption made in [31-33], it was assumed that $f_T(r) = f_c^{Lip}(r)$. As discussed in chapter 5, this consumption/displacement speed model amounts to assuming that the flame surface responds locally to turbulent velocity fluctuations. Again, the kinematic coupling effects are not captured in this model as well.

Figure 7-6a shows the radial variation of local consumption and displacement speeds from the non-local model (eqs. (6.39) and (6.44)). Note first from fig. 7-6a that the predicted $f_T(r)$ and $f_c(r)$ variations with r are not the same, as noted in the previous chapter. The spatial variation in each of the above is induced by flame surface response non-locality as discussed in chapters 4 and 5. The difference between the two quantities is due to the fact that $f_T(r)$ is the propagation speed of the mean flame surface in the burner fixed co-ordinates (see fig. 6-3), while $f_c(r)$ is a measure of the net mass burning rate change due to turbulence of an area element on the mean flame surface. This reference area is shown schematically in fig. 7-6b. The mean surface shown in this figure is not the same as the nominal flame surface because of the presence of turbulence fluctuations. Notice that for the low value of turbulence intensity assumed in the present analysis (ε_T = 0.05), the area change due to flame wrinkling will be relatively small when compared the reference area shown in fig. 7-6b resulting in the value of

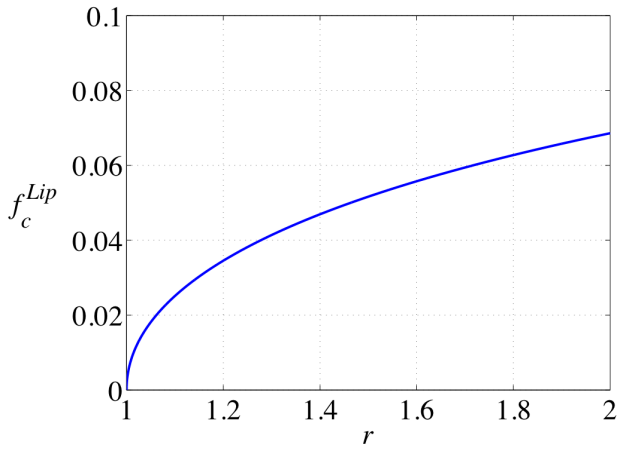

Figure 7-7: Variation of normalized local consumption/displacement speeds from the theory of Lipatnikov and Chomiak. Turbulent mixing time T=50, S_o/s_L =0.13, γ= 45^o and flame length, Λ=1.

$f_c(r)$ ~ 1, suggesting that the assumption of You et al. [33], i.e. $f_c(r)$ = constant is a good assumption in this case. However, the same cannot be assured at higher turbulence intensities. Thus, in the results presented next, the predictions of the present non-local model and those of You et al.[33] will not be very different from each other. Therefore, only results from the former model will be presented in the interest of clarity.

The corresponding variation of f_c, (or f_T) from the LC model is shown in fig. 7-7. Note that this model predicts a consumption speed that is lower than the laminar flame speed. This is not an artifact of the choice of model input parameters as can be seen in general from eq. (7.4) but rather, due to the turbulent diffusion assumption as discussed in chapter 5. However, the above result will be retained in order to compare predictions between the two modeling approaches.

Figure 7-8 compares the predicted variation of the magnitude and phase of the heat-release transfer function from the modeling approach using the different models for $f_T(r)$ and $f_c(r)$ as described above, and the exact asymptotic analysis presented in the

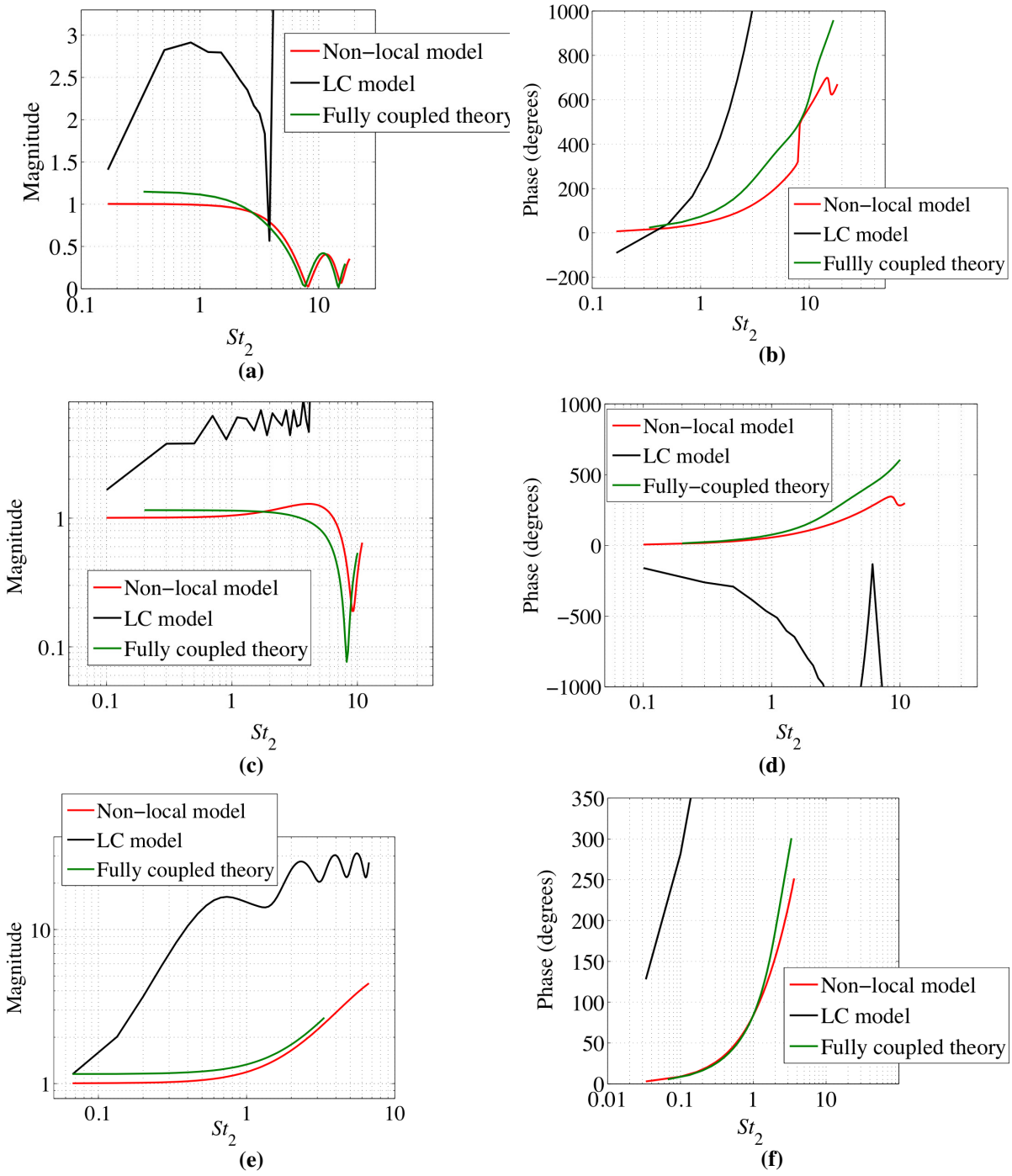

Figure 7-8: Comparison of transfer function magnitude and phase from the two modeling approaches and the theoretical analysis (a)-(b) K = 0.3, (c)-(d) K = 0.5, (e)-(f) K = 1.5, ε_T =0.05 and γ= 45°

previous section. Consider first the non-local model. Note that in every case, the agreement between the predicted magnitude and phase from the non-local model is in good agreement with the exact asymptotic result. However, the model cannot capture the non-unity magnitude of the exact result as $St_2 \rightarrow 0$ because the assumed flame speed model does not predict the modulation of flame speed with coherent forcing as no description of kinematic coupling effects on the local consumption and displacement speeds has been included. This result provides further evidence in support of the argument advanced earlier in this context.

The LC model prediction is in poor agreement with the exact asymptotic result. The possible reasons for this result are as follows. First, the consumption and displacement speeds have been assumed to be identical. This is at variance with the exact kinematic result that the non-local model shows. Second, the model does not account for the non-local nature of flame surface response within its framework as discussed in chapter 5. Further, the model requires the specification of a fully developed flame speed value (S_o / s_L). This value has been specified from the heuristic argument of Dowling. This requirement represents the general issue with, most heuristic models for displacement/consumption speed as they are based on adjustable parameters that may be hard to determine in general. The LC model is an example of such a model. However, the results from the non-local model presented here are encouraging and suggest that models that incorporate the physics of non-local response may be more successful in predicting turbulent premixed flame heat-release response for low values of St_2. As they capture more realistically the underlying features of flame surface perturbations.

Chapter 8

Conclusion and recommendations

The principal conclusions of the present work are as follows.

8.1 Flame kinematics – unforced flame

The net flame surface wrinkling at any point on the flame surface is a resultant of the superposition of wrinkles generated at upstream points at earlier times causing the flame response to become non-local. Thus the spatio-temporal correlation functions of flame surface slope and local burning area show advected characteristics. The correlation length over which flame surface slope and burning area decay is shown to be smaller than that of the corresponding length scale for turbulence fluctuations. The decay rate of the local burning area correlation reduces with u'/s_L because the characteristic destruction time of large length scale wrinkles induced on the flame surface by turbulent fluctuations increases.

Explicit results for the spatial distribution of local consumption speed were determined from linear theory and were compared to corresponding results from computations. It was found that there is always a region close to the flame holder where the flame's dynamics are linear resulting in the good agreement between the linear theory and computed result. Beyond this region kinematic restoration limits the increase in burning area due to flame wrinkling and causes the value to deviate from the predicted linear theory value. The present results suggest that the local consumption speed eventually reaches a constant value when the rate of area destruction due to kinematic

restoration balances the creation of area by turbulence fluctuations. A comparison of present results with the spatially developing local consumption speed of Lipatnikov and Chomiak [11] resulted in poor agreement suggesting that the underlying turbulent diffusion hypotheses made in the latter are incomplete when describing attached flames.

8.2 Forced response – Heat release transfer function

The ensemble averaged heat release response of a turbulent premixed flame is quantitatively different from the corresponding response if there were no turbulent fluctuations (i.e. if the flame were to be laminar). This is due to kinematic coupling between the flame wrinkling due to the coherent response and the random wrinkling due to turbulence flucutations. It is shown that this leading order correction to the ensemble averaged heat release is characterized by a Strouhal number based on a turbulence length scale and the convective velocity of imposed coherent harmonic forcing, the nominal flame angle (which is a surrogate for the laminar flame speed in this analysis) and the ratio of mean flow velocity to the convective speed of the coherent fluctuations.

Kinematic coupling results in the modulation of local/global consumption speeds due to acoustic forcing resulting in a non-unity gain in the low Strouhal number limit for the total transfer function. The magnitude of the turbulence correction drops with increasing Strouhal number because of the destruction of high amplitude small scale wrinkles on the flame surface that are destroyed by kinematic restoration. Kinematic coupling also causes the phase of the leading order turbulence correction term relative to the laminar baseline contribution to vary. The above arguments are supported by a reduction in turbulence correction magnitude with increasing laminar flame speed.

A generalized modeling approach to determine turbulent flame response is developed in terms of general local consumption and displacement speed models. Predictions from this model are obtained for the present configuration from a non-local consumption and displacement speed models developed in the present work as also from the model of Lipatnikov and Chomiak [11]. The non-local model recovers reasonably, the qualitative and quantitative features of the flame response as predicted by the exact asymptotic solution. However, the predicted response using model of Lipatnikov and Chomiak[11] is in poor agreement with the same. Hence, this result suggests that in general distinct consumption and displacement speed models incorporating the features of non-local flame surface response will be more successful in predicting the overall heat release response of turbulent flames.

8.3 Recommendations for future work

The present analysis may be extended to include the influence of flame stretch on the laminar flame speed in the low amplitude turbulence limit. The results thus obtained may be compared with existing DNS/experimental studies of similar configurations in order to understand the influence of flame stretch on turbulent flame surface motions from a kinematic perspective. This may be done in the initial linear kinematic region in the near-field of the bluff body. This may be performed for both acoustically forced and unforced cases.

Further numerical computations such as those performed in this work may be performed over a wider range of turbulence intensities in order to study possible self similarity characteristics of flame surface wrinkling and local consumption speed

saturation at high turbulence intensities in order to elucidate well known self-similar characteristics of turbulent flame brushes.

Since the present computations for the unforced case indicate good agreement with linear theory at low u'/s_L values, it is possible that this fact may be exploited in order to develop subgrid scale flame wrinkling/local consumption/displacement speed models for LES computations.

Computations in the high Strouhal number limit for the forced case maybe performed with an algorithmic approach that takes advantage of distributed memory systems. Thus, the influence of turbulence on the ensemble averaged flame response at high turbulence intensities can be determined.

Further experimental/theoretical work is required to describe the modulation of local and global consumption speeds as also the local displacement speed of flame surface motions over an excitation cycle due to the presence of kinematic coupling and non-locality. It is envisaged that this knowledge will allow for more accurate modeling of the ensemble averaged heat release response of turbulent premixed flame subjected to acoustic forcing.

The present asymptotic analysis for the forced response may be extended to the quasi-steady partially premixed regime analogously to past laminar approaches by including a description of passive scalar transport for the mixture fraction from theoretical considerations. The heat release response model may also be extended to the partially-premixed case by replacing the present constant equivalence ratio non-local turbulent

flame speed model with the partially premixed equivalents from the exact asymptotic analysis.

The recent experimental work of Shanbhogue et al [48] has shown that the coherent forcing amplitude for an acoustically forced nominally two dimensional premixed flame stabilized on a prismatic center-body decays with increasing distance from the flame holder. This effect may be incorporated into the velocity model of the present work.

Appendix A

Grid convergence

Grid convergence studies were performed to ensure that the grid was able to accurately resolve flame surface perturbations at the lowest turbulence intensity considered in this study i.e. $u'/s_L = 0.75$. This is because the level-set method tracks flame surface motions implicitly as the zero iso-surface of a three dimensional function. Hence sufficient grid resolution is required to accurately resolve flame surface features at the lowest value of turbulence intensity. Further, a qualitative examination of flame surface features revealed that the flame surface wrinkling amplitudes increase with increasing distance from the flame-holder. Therefore, the grid should have sufficient resolution to resolve the features of flame surface wrinkling in the near-field of the flame-holder. Computations for the nominally two dimensional V-flame were perfomed on grids with spacing Δx = 0.2, 0.1 and 0.05 for the present grid convergence study.

Figure A-1 shows the spatial variation of the ensemble averaged increase in local burning area, normalized by the corresponding reference area on the nominal flame surface ($\Delta A_I/A_{L,ref}$), due to turbulence fluctuations along the s-direction i.e., along the nominal flame surface, for each of the three grid resolutions. The solution at Δx = 0.2, 0.1 was obtained from averaging 400 and 900 realizations, respectively, of local burning area for each value of s. The solution for the Δx=0.05 case was determined from 1580 realizations at each value of s. Also shown for reference is the prediction of the above from linear kinematic theory (the second term on the RHS in eq. (4.34)). All curves as

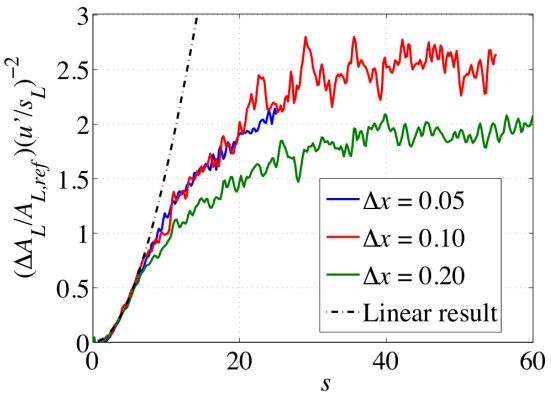

Figure A-1: Variation of ensemble averaged local burning area increase with flame surface location (on the nominal flame surface). Flame angle $\gamma \sim 4^o$. The broken curve shows the linear result.

presented have been normalized by $(u'/s_L)^2$. The number of grid points along the z-direction is 676 and has been kept constant for all the data shown in fig. A-1. Note this shows that the local burning area variation in the initial linear kinematics region is qualitatively similar for the Δx = 0.1 and 0.05 cases. Hence the latter is chosen as a reference solution.

Figure A-2 shows the spatial variation of the relative change in $\Delta A_L/A_{L,ref}$ as a percentage of the corresponding reference solution value for two successive grid refinements from Δx = 0.2 to Δx = 0.1 and Δx = 0.1 to 0.05. These curves are labeled by the coarser value of Δx in the refinement in each case. Note that the average relative change in local burning area increase is mostly less than 10% (avg. ~ 6.8%) for the latter refinement when compared to the former (avg. ~ 20.8%). Hence the grid size of Δx = 0.1 was chosen as the grid size for the results presented in chapter 5 in order to resolve the flame surface features sufficiently far away while ensuring that the solution is reasonably grid independent in a statistical sense. In the case of the results for the forced flame analysis however, the coarser value of Δx = 0.2 was chosen so as to allow for pockets

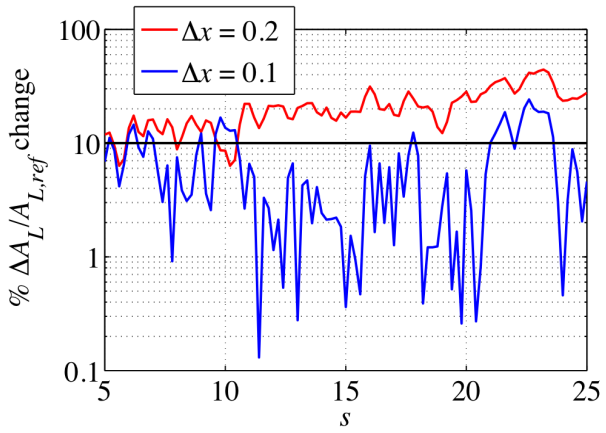

Figure A-2: Relative change in $\Delta A_L/A_{L,ref}$ over two successive grid refinements as a percentage of $\Delta A_L/A_{L,ref}$ at Δx=0.05. Note that in the second case, the relative change is less than 10% for a major portion of the flame surface considered.

formed on the flame surface to burn out within the domain as far as possible without increasing the number of grid points along the z-direction. Hence numerical results at large turbulence intensities alone have been presented in this work for this latter case in chapter 7. The latter constraint was imposed by the total system memory available on the computers used for the simulations in this work. It is envisaged that this restriction can be removed in the future by a dynamic scheduling implementation of the present numerical algorithms on distributed memory systems.

Appendix B

Non-Local Slope Correlation Functions

Expressions for the non-local slope correlations will be derived in this section in terms of the tranverse correlation function of the turbulence fluctuations presented in chapter . The non-local slope correlation function is given by eq. (4.13). This is repeated below for convenience.

$$R_{\xi'\xi'}^{NL}\left(s,\sigma_s,\sigma_y,\tau\right)=\frac{\left\langle\left(\partial\xi_{1t}/\partial s\right)\Big|_{s,y,t}\left(\partial\xi_{1t}/\partial s\right)\Big|_{s+\sigma_s,y+\sigma_y,t+\tau}\right\rangle}{\left\langle\left(\partial\xi_{1t}/\partial s\right)^2\right\rangle^{1/2}\Big|_{s,y,t}\left\langle\left(\partial\xi_{1t}/\partial s\right)^2\right\rangle^{1/2}\Big|_{s+\sigma_s,y+\sigma_y t}} \tag{B.1}$$

The instantaneous solution for the flame surface slope is given by the following,

$$\frac{\partial\xi_{1t}}{\partial s}\left(s,y,t\right)=\frac{1}{\cos\gamma}f_n\left(s,y,0,t\right)-\frac{1}{\cos^2\gamma}\int_0^s d\eta_1\ \frac{\partial f_n\left(\eta_1,y,0,\tau\right)}{\partial\tau}\Bigg|_{\tau=t-\frac{(s-\eta_1)}{\cos\gamma}} \tag{B.2}$$

The above yields,

$$\frac{\partial\xi_{1t}}{\partial s}\Bigg|_{s,y,t}\ \frac{\partial\xi_{1t}}{\partial s}\Bigg|_{s+\sigma_s,y+\sigma_y,t+\tau}=\left(\begin{array}{l}\frac{1}{\cos^2\gamma}f_n\left(s,y,0,t\right)f_n\left(s+\sigma_s,y+\sigma_y,0,t+\tau\right)\\ -\frac{1}{\cos^3\gamma}\int_0^{s+\sigma_s}d\eta_1\ f_n\left(s,y,0,t\right)\frac{\partial f_n\left(\eta_1,y+\sigma_y,0,\tau'\right)}{\partial\tau'}\Big|_{\tau'=t+\tau-\frac{(s+\sigma_s-\eta_1)}{\cos\gamma}}\\ -\frac{1}{\cos^3\gamma}\int_0^{s}d\eta_1\ f_n\left(s+\sigma_s,y+\sigma_y,0,t+\tau\right)\frac{\partial f_n\left(\eta_1,y,0,\tau'\right)}{\partial\tau'}\Big|_{\tau'=t-\frac{(s-\eta_1)}{\cos\gamma}}\\ +\frac{1}{\cos^4\gamma}\int_0^{s+\sigma_s}\int_0^{s}d\eta_1 d\eta_1'\ \frac{\partial f_n\left(\eta_1',y,0,\tau'\right)}{\partial\tau'}\Big|_{\tau'=t-\frac{(s-\eta_1')}{\cos\gamma}}\ \frac{\partial f_n\left(\eta_1,y+\sigma_y,0,\tau''\right)}{\partial\tau''}\Big|_{\tau''=t+\tau-\frac{(s+\sigma_s-\eta_1)}{\cos\gamma}}\end{array}\right) \tag{B.3}$$

Ensemble averaging the above equation yields,

$$\left\langle \left.\frac{\partial \xi_{1t}}{\partial s}\right|_{s,y,t} \left.\frac{\partial \xi_{1t}}{\partial s}\right|_{s+\sigma_s,y+\sigma_y,t+\tau} \right\rangle = \frac{1}{\cos^2\gamma} R_{22}\left(\sigma_s,\sigma_y,\tau\right) + \frac{1}{\cos^3\gamma}\int_0^{s+\sigma_s} d\eta_1 \left\{\frac{\partial R_{22}\left(\sigma_s',\sigma_y,\tau'\right)}{\partial \tau'}\right\}\Bigg|_{\substack{\sigma_s'=s-\eta_1,\\ \tau'=-\tau+\frac{(s+\sigma_s-\eta_1)}{\cos\gamma}}}$$

$$+\frac{1}{\cos^3\gamma}\int_0^{s} d\eta_1 \left\{\frac{\partial R_{22}\left(\sigma_s',\sigma_y,\tau'\right)}{\partial \tau'}\right\}\Bigg|_{\substack{\sigma_s'=\sigma_s+s-\eta_1\\ \tau'=\tau+\frac{(s-\eta_1)}{\cos\gamma}}}$$

$$-\frac{1}{\cos^4\gamma}\int_0^{s+\sigma_s}\int_0^{s} d\eta_1 d\eta_1' \left.\frac{\partial^2 R_{22}\left(\sigma_s',\sigma_y,\tau'\right)}{\partial \tau'^2}\right|_{\substack{\sigma_s'=\eta_1-\eta_1'\\ \tau'=\tau-\left\{\frac{\sigma_s-(\eta_1-\eta_1')}{\cos\gamma}\right\}}} \tag{B.4}$$

where, R_{22} is determined from the analysis in Appendix F. Thus, using the above in eq. (B.1) yields the desired result.

The corresponding local slope correlation (eq. (4.16)) can be derived using an approach along the lines of the analysis presented in Aldredge[46]. The starting point is the kinematic equation for flame surface perturbations assuming local response (eq. (4.14)) as follows,

$$\frac{\partial \xi_{1t}^L}{\partial t} = f_n\left(s,y,0,t\right) \tag{B.5}$$

Since, the turbulence fluctuations are assumed to be stationary and isotropic, the above can be written in terms of fourier components as follows,

$$\hat{\xi}_{1t}^L\left(k_s,k_y,\omega\right) = \frac{\hat{f}_n\left(k_s,k_y,0,\omega\right)}{-i\omega} \tag{B.6}$$

The above yields the following for the slope along the *s*-direction,

$$\frac{\partial \xi_{1t}^{L}}{\partial s} = \frac{1}{(2\pi)^3} \int_{-\infty}^{\infty} dk_s dk_y d\omega e^{-i\left(k_s s + k_y y + \omega t\right)} \left(\frac{k_s}{\omega}\right) \hat{f}_n\left(k_s, k_y, 0, \omega\right) \tag{B.7}$$

The integration on the RHS of the above is performed over each of the variables. Using the Weiner-Khinchin theorem, the above can be rewritten as follows,

$$\frac{\partial \xi_{1t}^{L}}{\partial s} = \frac{1}{(2\pi)^3} \int_{-\infty}^{\infty} ds_1 dy_1 dt_1 \; q\left(s_1, y_1, t_1\right) \; f_n\left(s - s_1, y - y_1, t - t_1\right) \tag{B.8}$$

where, the function q is the inverse fourier transform of the term within parantheses on the RHS of eq. (B.7). Thus correlation of flame surface slope between two flame surface locations (s, y) and $\left(s + \sigma_s, y + \sigma_y\right)$, at times t and $t+\tau$, is determined as follows,

$$\begin{aligned}
&\left\langle \left.\frac{\partial \xi_{1t}^{L}}{\partial s}\right|_{s,y,t} \left.\frac{\partial \xi_{1t}^{L}}{\partial s}\right|_{s+\sigma_s, y+\sigma_y, t+\tau} \right\rangle \\
&= \frac{1}{(2\pi)^6} \int_{-\infty}^{\infty}\int_{-\infty}^{\infty} ds_1 dy_1 dt_1 \, ds_2 dy_2 dt_2 \begin{Bmatrix} q\left(s_1, y_1, t_1\right) \\ q\left(s_2, y_2, t_2\right) \end{Bmatrix} \left\langle f_n\left(s - s_1, y - y_1, t - t_1\right) f_n\left(s + \sigma_s - s_2, y + \sigma_y - y_2, t + \tau - t_2\right) \right\rangle \\
&= \frac{1}{(2\pi)^6} \int_{-\infty}^{\infty}\int_{-\infty}^{\infty} ds_1 dy_1 dt_1 \, d\sigma_s' d\sigma_y' d\tau' \begin{Bmatrix} q\left(s_1, y_1, t_1\right) \\ q\left(s_1 + \sigma_s', y_1 + \sigma_y', t_1 + \tau'\right) \end{Bmatrix} \left\langle \begin{matrix} f_n\left(s - s_1, y - y_1, t - t_1\right) \\ f_n\left(\begin{matrix} s - s_1 + \sigma_s - \sigma_s', y - y_1 + \sigma_y - \sigma_y', \\ t - t_1 + \tau - \tau' \end{matrix}\right) \end{matrix} \right\rangle \\
&= \frac{1}{(2\pi)^6} \int_{-\infty}^{\infty}\int_{-\infty}^{\infty} ds_1 dy_1 dt_1 \, d\sigma_s' d\sigma_y' d\tau' \begin{Bmatrix} q\left(s_1, y_1, t_1\right) \\ q\left(s_1 + \sigma_s', y_1 + \sigma_y', t_1 + \tau'\right) \end{Bmatrix} R_{22}\left(\sigma_s - \sigma_s', \sigma_y - \sigma_y', \tau - \tau'\right) \\
&= \frac{1}{(2\pi)^3} \int_{-\infty}^{\infty} d\sigma_s' d\sigma_y' d\tau' \, R_{22}\left(\sigma_s - \sigma_s', \sigma_y - \sigma_y', \tau - \tau'\right) \int_{-\infty}^{\infty} dk_s dk_y d\omega \left(\frac{k_s}{\omega}\right)^2 e^{-i\left(k_s \sigma_s' + k_y \sigma_y' + \omega \tau'\right)} \\
&= \int_{-\infty}^{\infty} d\sigma_s' d\sigma_y' d\tau' \, R_{22}\left(\sigma_s - \sigma_s', \sigma_y - \sigma_y', \tau - \tau'\right) \left(\frac{|\tau'|}{2} \delta\left(\sigma_y'\right) \frac{d^2 \delta\left(\sigma_s'\right)}{d\sigma_s'^2}\right) \\
&= \int_{-\infty}^{\infty} d\tau' \frac{|\tau'|}{2} \left\{ -\frac{\partial^2 R_{22}\left(\sigma_s'', \sigma_y, \tau''\right)}{\partial \sigma_s''^2} \right\} \Bigg|_{\sigma_s'' = \sigma_s, \tau'' = \tau + \tau'}
\end{aligned} \tag{B.9}$$

Thus, the resultant local slope correlation function is given by,

$$R^{L}_{\xi'\xi'}\left(\sigma_s,\sigma_y,\tau\right)=\frac{\int_{-\infty}^{\infty}d\tau'\left|\tau'\right|\left\{-\frac{\partial^2 R_{22}\left(\sigma_s'',\sigma_y'',\tau''\right)}{\partial\sigma_s''^2}\right\}\Bigg|_{\sigma_s''=\sigma_s,\sigma_y''=\sigma_y,\tau''=\tau'+\tau}}{\int_{-\infty}^{\infty}d\tau'\left|\tau'\right|\left\{-\frac{\partial^2 R_{22}\left(\sigma_s'',\sigma_y'',\tau''\right)}{\partial\sigma_s''^2}\right\}\Bigg|_{\sigma_s''=0,\sigma_y''=0,\tau''=\tau'}} \quad \text{(B.10)}$$

Appendix C

Unforced flame formulation

The aim of this appendix is to document details of derivation of mean-squared flame surface slope as a supplement to the theoretical formulation for local consumption speed analysis presented in chapter 4. The starting point of the analysis is the solution to the flame surface shape at leading order as follows,

$$\xi_{1t}(s,y,t)=\frac{1}{\cos\gamma}\int_0^s d\eta_1\ f_n\left(\eta_1,y,0,t-\frac{(s-\eta_1)}{\cos\gamma}\right) \tag{C.1}$$

Differentiating the above w. r. t. s yields,

$$\frac{\partial\xi_{1t}}{\partial s}=\frac{1}{\cos\gamma}f_n(s,y,0,t)-\frac{1}{\cos^2\gamma}\int_0^s d\eta_1\ \left.\frac{\partial f_n(\eta_1,y,0,\tau)}{\partial\tau}\right|_{\tau=t-\frac{(s-\eta_1)}{\cos\gamma}} \tag{C.2}$$

Thus, the above yields,

$$\left(\frac{\partial\xi_{1t}}{\partial s}\right)^2=\frac{1}{\cos^2\gamma}\left(\begin{array}{l} f_n(s,y,0,t)f_n(s,y,0,t)-\dfrac{2}{\cos\gamma}\displaystyle\int_0^s d\eta_1\ f_n(s,y,0,t)\left.\frac{\partial f_n(\eta_1,y,0,\tau')}{\partial\tau'}\right|_{\tau'=t-\frac{(s-\eta_1)}{\cos\gamma}} \\ +\dfrac{1}{\cos^2\gamma}\displaystyle\int_0^s\int_0^s d\eta_1 d\eta_1'\ \left.\frac{\partial f_n(\eta_1',y,0,\tau')}{\partial\tau'}\right|_{\tau'=t-\frac{(s-\eta_1')}{\cos\gamma}}\left.\frac{\partial f_n(\eta_1,y,0,\tau'')}{\partial\tau''}\right|_{\tau''=t-\frac{(s-\eta_1)}{\cos\gamma}} \end{array}\right) \tag{C.3}$$

Ensemble averaging the above yields,

$$\left\langle \left(\frac{\partial \xi_{1t}}{\partial s} \right)^2 \right\rangle = \frac{1}{\cos^2\gamma} \left(\begin{array}{l} 1 + \dfrac{2}{\cos\gamma} \displaystyle\int_0^s d\eta_1 \left. \dfrac{\partial R_{22}\left(\sigma_s, \sigma_y, \tau\right)}{\partial \tau} \right|_{\substack{\sigma_s = s-\eta_1, \sigma_y = 0 \\ \tau = t - \frac{(s-\eta_1)}{\cos\gamma}}} \\ -\dfrac{1}{\cos^2\gamma} \displaystyle\int_0^s \int_0^s d\eta_1 d\eta_1' \left. \dfrac{\partial^2 R_{22}\left(\sigma_s, \sigma_y, \tau\right)}{\partial \tau^2} \right|_{\substack{\sigma_s = \eta_1 - \eta_1', \sigma_y = 0 \\ \tau = t - \frac{(\eta_1 - \eta_1')}{\cos\gamma}}} \end{array} \right) \tag{C.4}$$

The last term in the parentheses on the RHS can be rewritten in terms of $\sigma = \eta_1 - \eta_1'$ to yield the following expression

$$\left\langle \left(\frac{\partial \xi_{1t}}{\partial s} \right)^2 \right\rangle = \frac{1}{\cos^2\gamma} \left(\begin{array}{l} 1 + \dfrac{2}{\cos\gamma} \displaystyle\int_0^s d\eta_1 \left. \dfrac{\partial R_{22}\left(\sigma_s, \sigma_y, \tau\right)}{\partial \tau} \right|_{\substack{\sigma_s = s-\eta_1, \sigma_y = 0 \\ \tau = t - \frac{(s-\eta_1)}{\cos\gamma}}} \\ -\dfrac{1}{\cos^2\gamma} \displaystyle\int_{-s}^s d\sigma \left(s - |\sigma|\right) \left. \dfrac{\partial^2 R_{22}\left(\sigma_s, \sigma_y, \tau\right)}{\partial \tau^2} \right|_{\substack{\sigma_s = \sigma, \sigma_y = 0 \\ \tau = t - \frac{\sigma}{\cos\gamma}}} \end{array} \right) \tag{C.5}$$

Next differentiating eq. (C.1) w. r. t. *y* yields,

$$\frac{\partial \xi_{1t}(s, y, t)}{\partial y} = \frac{1}{\cos\gamma} \int_0^s d\eta_1 \frac{\partial f_n\left(\eta_1, y, 0, t - \dfrac{(s-\eta_1)}{\cos\gamma}\right)}{\partial y} \tag{C.6}$$

Squaring the above yields,

$$\left(\frac{\partial \xi_{1t}(s, y, t)}{\partial y} \right)^2 = \frac{1}{\cos^2\gamma} \int_0^s \int_0^s d\eta_1 \, d\eta_1' \frac{\partial f_n\left(\eta_1, y, 0, t - \dfrac{(s-\eta_1)}{\cos\gamma}\right)}{\partial y} \frac{\partial f_n\left(\eta_1', y, 0, t - \dfrac{(s-\eta_1')}{\cos\gamma}\right)}{\partial y} \tag{C.7}$$

Ensemble averaging the above yields,

$$\left\langle \left(\frac{\partial \xi_{1t}(s,y,t)}{\partial y} \right)^2 \right\rangle = \frac{1}{\cos^2 \gamma} \int_0^s \int_0^s d\eta_1 \, d\eta_1' \, \frac{\partial^2 R_{22}(\sigma_s, \sigma_y, \tau)}{\partial \sigma_y^2} \Bigg|_{\substack{\sigma_s = \eta_1 - \eta_1', \sigma_y = 0, \\ \tau = \frac{\eta_1 - \eta_1'}{\cos \gamma}}} \qquad \text{(C.8)}$$

Appendix D

Forced flame formulation

The aim of this appendix is to document the expressions for the various terms appearing in the leading order turbulence correction to the heat release transfer function. This correction term is repeated here for convenience.

$$F_T\left(St\right)=\frac{2}{\left(R^2-r_f^2\right)}\int_{r_f}^{R}drd\theta\ r\left(\begin{array}{l}\frac{\sin^2\gamma}{r^2}\left\langle\frac{\partial\zeta_{1t}}{\partial\theta}\frac{\partial\hat{\xi}_{2ct}}{\partial\theta}\right\rangle+\sin^4\gamma\left(\left\langle\frac{\partial\zeta_{1t}}{\partial r}\frac{\partial\hat{\xi}_{2ct}}{\partial r}\right\rangle\right)\\-\left(\frac{1+\cos^2\gamma}{2\cos\gamma}\right)\sin^5\gamma\frac{\partial\hat{\xi}_{1c}}{\partial r}\left\langle\left(\frac{\partial\zeta_{1t}}{\partial r}\right)^2\right\rangle-\frac{\sin^3\gamma}{2r^2\cos\gamma}\left\langle\left(\frac{\partial\zeta_{1t}}{\partial\theta}\right)^2\right\rangle\frac{\partial\hat{\xi}_{1c}}{\partial r}\\+\frac{\sin^3\gamma}{\cos\gamma}\frac{\partial\hat{\xi}_{1c}}{\partial r}\left(\begin{array}{l}-\frac{1}{r}\left\langle f_\theta\left(r,\theta,\left(r-r_f\right)\cot\gamma,t\right)\frac{\partial\zeta_{1t}}{\partial\theta}\right\rangle\\-\left\langle f_u\left(r,\theta,\left(r-r_f\right)\cot\gamma,t\right)\frac{\partial\zeta_{1t}}{\partial r}\right\rangle\end{array}\right)\\+\frac{\sin^2\gamma}{\cos\gamma}\frac{\partial\hat{\xi}_{1c}}{\partial r}\left\langle\zeta_{1t}\left(r,\theta,t\right)\left\{\left.\frac{\partial f_n}{\partial z}\right|_{\left(r,\theta,z=\left(r-r_f\right)\cot\gamma,t\right)}\right\}\right\rangle+\cos\gamma\sin\gamma\left\langle\frac{\partial\hat{\xi}_{3ctt}}{\partial r}\right\rangle\end{array}\right)\tag{D.1}$$

The expressions for the above will be presented in time domain. These can be converted to the Strouhal number domain via a fourier transform. The fundamental result is the flame shape at leading order in ε_T as follows,

$$\zeta_{1t}\left(r,\theta,t\right)=\frac{1}{\cos\gamma\sin^2\gamma}\int_{r_f}^{r}f_n\left(\eta_1,\theta,z=\left(\eta_1-r_f\right)\cot\gamma,t-\frac{\left(r-\eta_1\right)}{\cos\gamma\sin\gamma}\right)d\eta_1\tag{D.2}$$

The various spatio-temporal correlation functions required for the evaluation of the ensemble averages in eq. (D.1) are as follows,

- Normal-normal correlation:

$$R_{nn}\left(\eta_1,\eta_2,\theta,\phi,z_1,z_2,\tau\right)=\left\langle f_n\left(\eta_1,\phi,z_1,t\right)f_n\left(\eta_2,\theta,z_2,t+\tau\right)\right\rangle$$

- Normal-radial correlation:

$$R_{un}\left(\eta_1,\eta_2,\theta,\phi,z_1,z_2,\tau\right)=\left\langle f_n\left(\eta_1,\phi,z_1,t\right)f_u\left(\eta_2,\theta,z_2,t+\tau\right)\right\rangle$$

- Normal-azimuthal correlation:

$$R_{\theta n}\left(\eta_1,\eta_2,\theta,\phi,z_1,z_2,\tau\right)=\left\langle f_n\left(\eta_1,\phi,z_1,t\right)f_\theta\left(\eta_2,\theta,z_2,t+\tau\right)\right\rangle$$

- Azimuthal-radial correlation:

$$R_{\theta u}\left(\eta_1,\eta_2,\theta,\phi,z_1,z_2,\tau\right)=\left\langle f_u\left(\eta_1,\phi,z_1,t\right)f_\theta\left(\eta_2,\theta,z_2,t+\tau\right)\right\rangle$$

- Radial-radial correlation:

$$R_{uu}\left(\eta_1,\eta_2,\theta,\phi,z_1,z_2,\tau\right)=\left\langle f_u\left(\eta_1,\phi,z_1,t\right)f_u\left(\eta_2,\theta,z_2,t+\tau\right)\right\rangle$$

Thus, the various terms in eq. (D.1) can be evaluated as follows,

Terms from $O\left(\varepsilon_a^0\right)$:

$$\left\langle \left(\frac{\partial \zeta_{1t}\left(r,\theta,t\right)}{\partial r} \right)^2 \right\rangle = \frac{1}{\cos^2\gamma \sin^4\gamma} + \frac{2}{\cos^3\gamma \sin^5\gamma} \int_{r_f}^{r} \left. \frac{\partial R_{nn}\left(\eta_1, r, \theta, \theta, \left(r-r_f\right)\cot\gamma, \tau\right)}{\partial \tau} \right|_{\tau=\frac{(r-\eta_1)}{\cos\gamma\sin\gamma}} d\eta_1 - \frac{1}{\cos^4\gamma \sin^6\gamma} \int_{r_f}^{r}\int_{r_f}^{r} \left. \frac{\partial^2 R_{nn}\left(\eta_1, \eta_2, \theta, \theta, \left(\eta_2-r_f\right)\cot\gamma, \tau\right)}{\partial \tau^2} \right|_{\tau=\frac{(\eta_2-\eta_1)}{\cos\gamma\sin\gamma}} d\eta_1 d\eta_2 \tag{D.3}$$

$$\left\langle \left(\frac{\partial \zeta_{1t}\left(r,\theta,t\right)}{\partial \theta} \right)^2 \right\rangle = \frac{1}{\cos^2\gamma \sin^4\gamma} \int_{r_f}^{r}\int_{r_f}^{r} d\eta_1 d\eta_2 \left[\frac{\partial^2}{\partial\phi\partial\theta} \left\{ R_{nn}\left(\eta_1, \eta_2, \theta, \phi, \left(\eta_1-r_f\right)\cot\gamma, \left(\eta_2-r_f\right)\cot\gamma, \left(\eta_2-\eta_1\right)/\cos\gamma\sin\gamma\right)\right\}\right]\Bigg|_{\theta=\phi} \tag{D.4}$$

$$\left\langle f_\theta\left(r,\theta,r-r_f,t\right)\frac{\partial \zeta_{1t}}{\partial\theta}\right\rangle = \frac{1}{\cos\gamma\sin^2\gamma} \int_{r_f}^{r} d\eta_1 \left[\frac{\partial}{\partial\phi} \left\{ R_{\theta n}\left(\eta_1, r, \theta, \phi, \left(\eta_1-r_f\right)\cot\gamma, \left(r-r_f\right)\cot\gamma, \left(r-\eta_1\right)/\cos\gamma\sin\gamma\right)\right\}\right]\Bigg|_{\theta=\phi} \tag{D.5}$$

$$\left\langle f_u\left(r,\theta,r-r_f,t\right)\frac{\partial\zeta_{1t}}{\partial r}\right\rangle=\left\{\begin{array}{l}-\dfrac{1}{\sin^2\gamma}\\ +\dfrac{1}{\cos^2\gamma\sin^3\gamma}\displaystyle\int_{r_f}^{r}\left.\frac{\partial R_{un}\left(\eta_1,r,\theta,\theta,\left(\eta_1-r_f\right)\cot\gamma,\left(r-r_f\right)\cot\gamma\tau\right)}{\partial\tau}\right|_{\tau=\frac{(r-\eta_1)}{\cos\gamma\sin\gamma}}d\eta_1\end{array}\right\} \tag{D.6}$$

$$\left\langle\zeta_{1t}\left(r,\theta,t\right)\frac{f_{n,z}\left(r,\theta,\left(r-r_f\right)\cot\gamma,t\right)}{\sin\gamma}\right\rangle$$
$$=\frac{1}{\cos\gamma\sin^3\gamma}\int_{r_f}^{r}d\eta_1\left[\frac{\partial}{\partial z_2}\left\{R_{nn}\left(\eta_1,r,\theta,\theta,\left(\eta_1-r_f\right)\cot\gamma,z_2,\left(r-\eta_1\right)/\cos\gamma\sin\gamma\right)\right\}\right]\Bigg|_{z_2=\left(r-r_f\right)\cot\gamma} \tag{D.7}$$

Terms from $O(\varepsilon_a)$:

$$\left\langle\frac{\partial\zeta_{1t}}{\partial\theta}\frac{\partial\zeta_{2ct}}{\partial\theta}\right\rangle=\left.\frac{\partial^2\left\langle\zeta_{1t}\left(r_1,\phi,t\right)\zeta_{2ct}\left(r,\theta,t\right)\right\rangle}{\partial\phi\partial\theta}\right|_{\substack{\theta=\phi\\ r_1=r}} \tag{D.8}$$

$$\left\langle\frac{\partial\zeta_{1t}}{\partial r}\frac{\partial\zeta_{2ct}}{\partial r}\right\rangle=\left.\frac{\partial^2\left\langle\zeta_{1t}\left(r_1,\phi,t\right)\zeta_{2ct}\left(r,\theta,t\right)\right\rangle}{\partial r_1\partial r}\right|_{\substack{\theta=\phi\\ r_1=r}} \tag{D.9}$$

The derivatives on the RHS of both of the above can be evaluated by appropriately differentiating the following expression.

$$\left\langle \zeta_{1t}(r_1,\phi,t)\,\zeta_{2ct}(r,\theta,t)\right\rangle$$

$$= \frac{-1}{\sin^2\gamma}\int_{r_f}^{r} d\eta_2 \left\langle \zeta_{1t}(r_1,\phi,t)\,\zeta_{1t}\left(\eta_2,\theta,t-\frac{r-\eta_2}{\sin\gamma\cos\gamma}\right)\right\rangle \begin{Bmatrix} \frac{1}{2}K^2\eta_2\left(\frac{St}{\Lambda}\right)^2\cos\left(\frac{St}{\Lambda}\left(t-\frac{r-\eta_2}{\sin\gamma\cos\gamma}-K\left(\eta_2-r_f\right)\cot\gamma\right)\right) \\ -\frac{KSt}{\Lambda\cot\gamma}\sin\left(\frac{St}{\Lambda}\left(t-\frac{r-\eta_2}{\sin\gamma\cos\gamma}-K\left(\eta_2-r_f\right)\cot\gamma\right)\right) \end{Bmatrix}$$

$$-\frac{1}{\sin\gamma\cos\gamma}\int_{r_f}^{r} d\eta_2 \left\langle \zeta_{1t}(r_1,\phi,t)\,f_u\left(\eta_2,\theta,\left(\eta_2-r_f\right)\cot\gamma,t-\frac{r-\eta_2}{\sin\gamma\cos\gamma}\right)\right\rangle \frac{\partial\zeta_{1c}\left(\eta_2,\theta,t-\frac{r-\eta_2}{\sin\gamma\cos\gamma}\right)}{\partial r}$$

$$+\frac{1}{2\sin\gamma\cos\gamma}\int_{r_f}^{r} d\eta_2 K\eta_2\left(\frac{St}{\Lambda}\right)\left\langle \zeta_{1t}(r_1,\phi,t)\frac{\partial\zeta_{1t}\left(\eta_2,\theta,t-\frac{r-\eta_2}{\sin\gamma\cos\gamma}\right)}{\partial r}\right\rangle \sin\left(\frac{St}{\Lambda}\left(t-\frac{r-\eta_2}{\sin\gamma\cos\gamma}-K\left(\eta_2-r_f\right)\cot\gamma\right)\right)$$

$$-\frac{\sin^3\gamma}{\cos\gamma}\int_{r_f}^{r} d\eta_2 \frac{\partial\zeta_{1c}\left(\eta_2,\theta,t-\frac{r-\eta_2}{\sin\gamma\cos\gamma}\right)}{\partial r}\left\langle \zeta_{1t}(r_1,\phi,t)\frac{\partial\zeta_{1t}\left(\eta_2,\theta,t-\frac{r-\eta_2}{\sin\gamma\cos\gamma}\right)}{\partial r}\right\rangle$$

$$-\frac{1}{\sin\gamma\cos\gamma}\int_{r_f}^{r} d\eta_2\zeta_{1c}\left(\eta_2,\theta,t-\frac{r-\eta_2}{\sin\gamma\cos\gamma}\right)\left\langle \zeta_{1t}(r_1,\phi,t)\frac{f_{n,z}\left(\eta_2,\theta,\left(\eta_2-r_f\right)\cot\gamma,t-\frac{r-\eta_2}{\sin\gamma\cos\gamma}\right)}{\sin\gamma}\right\rangle \tag{D.10}$$

The various correlations required to evaluate the above expression are as follows,

$$\left\langle \zeta_{1t}(r_1,\phi,t)\,\zeta_{1t}(r,\theta,t)\right\rangle =$$

$$\frac{1}{\cos^2\gamma\sin^4\gamma}\int_{r_f}^{r_1}\int_{r_f}^{r} d\eta_1 d\eta_2\; R_{nn}\left(\eta_1,\eta_2,\phi,\theta,\left(\eta_1-r_f\right)\cot\gamma,\left(\eta_2-r_f\right)\cot\gamma,\left(r_1-r+\eta_2-\eta_1\right)/\cos\gamma\sin\gamma\right) \tag{D.11}$$

$$\left\langle \zeta_{1t}(r_1,\phi,t)\,f_u\left(r,\theta,\left(r-r_f\right)\cot\gamma,t\right)\right\rangle$$

$$= \frac{1}{\cos\gamma\sin^2\gamma}\int_{r_f}^{r_1} d\eta_1\; R_{un}\left(\eta_1,r,\theta,\theta,\left(\eta_1-r_f\right)\cot\gamma,\left(r-r_f\right)\cot\gamma,\left(r_1-\eta_1\right)/\cos\gamma\sin\gamma\right) \tag{D.12}$$

$$\left\langle \zeta_{1t}\left(r_1,\phi,t\right)\frac{\partial\zeta_{1t}}{\partial r}\bigg|_{r,\theta,t}\right\rangle$$

$$=\frac{1}{\cos^2\gamma\sin^4\gamma}\left(\begin{array}{l}\int_{r_f}^{r_1}d\eta_1 R_{nn}\left(\eta_1,\eta_2,\theta,\phi,\left(\eta_2-r_f\right)\cot\gamma,\left(\eta_1-r_f\right)\cot\gamma,\dfrac{\left(r_1-\eta_1\right)}{\cos\gamma\sin\gamma}\right)\\ +\dfrac{1}{\cos\gamma\sin\gamma}\int_{r_f}^{r_1}\int_{r_f}^{r}d\eta_1' d\eta_1\left.\dfrac{\partial R_{nn}\left(\eta_1,\eta_1',\theta,\phi,\left(\eta_1'-r_f\right)\cot\gamma,\left(\eta_1-r_f\right)\cot\gamma,\tau\right)}{\partial\tau}\right|_{\tau=\frac{r_1-r+(\eta_1-\eta_1')}{\cos\gamma\sin\gamma}}\end{array}\right)$$

(D.13)

$$\left\langle \zeta_{1t}\left(r_1,\phi,t\right)\frac{f_{n,z}\left(r,\theta,\left(r-r_f\right)\cot\gamma,t\right)}{\sin\gamma}\right\rangle$$

$$=\frac{1}{\cos\gamma\sin^3\gamma}\int_{r_f}^{r_1}d\eta_1\left.\frac{\partial R_{nn}\left(\eta_1,r,\phi,\theta,\left(\eta_1-r_f\right)\cot\gamma,z_2,\left(r_1-\eta_1\right)/\cos\gamma\sin\gamma\right)}{\partial z_2}\right|_{z_2=\left(r-r_f\right)\cot\gamma}$$

(D.14)

.Finally, the term $\left\langle\frac{\partial\zeta_{3ctt}}{\partial r}\right\rangle$ can be evaluated as the solution to the following equation

$$\frac{\partial\langle\zeta_{3ctt}\rangle}{\partial t}+\cos\gamma\sin\gamma\frac{\partial\langle\zeta_{3ctt}\rangle}{\partial r}=$$

$$-\begin{Bmatrix}\frac{1}{2}K^2\left(\frac{St}{\Lambda}\right)^2\cos\left[\frac{St}{\Lambda}\left(t-K\left(r-r_f\right)\cot\gamma\right)\right]+\\ \frac{1}{4}K^3r\left(\frac{St}{\Lambda}\right)^3\cot\gamma\sin\left[\frac{St}{\Lambda}\left(t-\left(r-r_f\right)\cot\gamma\right)\right]\end{Bmatrix}\left\langle\zeta_{1t}\left(r,\theta,t\right)^2\right\rangle$$

$$-\begin{Bmatrix}\frac{1}{2}K^2r\left(\frac{St}{\Lambda}\right)^2\cos\left[\frac{St}{\Lambda}\left(t-K\left(r-r_f\right)\cot\gamma\right)\right]\cot\gamma\\ -KSt\sin\left[\frac{St}{\Lambda}\left(t-\left(r-r_f\right)\cot\gamma\right)\right]\end{Bmatrix}\left\langle\zeta_{2t}\left(r,\theta,t\right)\right\rangle$$

$$+\frac{1}{r}\left\langle f_\theta\left(r,\theta,\left(r-r_f\right)\cot\gamma,t\right)\frac{\partial\zeta_{2ct}}{\partial\theta}\right\rangle-\frac{1}{4}K^2r\left(\frac{St}{\Lambda}\right)^2\cos\left[\left(\frac{St}{\Lambda}\right)\left(t-K\left(r-r_f\right)\cot\gamma\right)\right]\frac{\partial\left\langle\zeta_{1t}\left(r,\theta,t\right)^2\right\rangle}{\partial r}$$

$$-\left\langle f_u\left(r,\theta,\left(r-r_f\right)\cot\gamma,t\right)\frac{\partial\zeta_{2ct}}{\partial r}\right\rangle+\frac{1}{2}Kr\left(\frac{St}{\Lambda}\right)\sin\left[\left(\frac{St}{\Lambda}\right)\left(t-\left(r-r_f\right)\cot\gamma\right)\right]\left\langle\frac{\partial\zeta_{2t}}{\partial r}\right\rangle$$

$$+\sin^3\gamma\cos\gamma\left(\frac{\partial\zeta_{1c}}{\partial r}\left\langle\left(\frac{\partial\zeta_{1t}}{\partial r}\right)^2\right\rangle+\cot\gamma\left\langle\frac{\partial\zeta_{1t}}{\partial r}\frac{\partial\zeta_{2ct}}{\partial r}\right\rangle\right)$$

$$-\frac{1}{2}\sin\gamma\cos\gamma\frac{\partial\zeta_{1c}}{\partial r}\begin{pmatrix}\left(3\cos^2\gamma-1\right)\sin^2\gamma\left\langle\left(\frac{\partial\zeta_{1t}}{\partial r}\right)^2\right\rangle-\frac{\sin^2\gamma}{r^2}\left\langle\left(\frac{\partial\zeta_{1t}}{\partial\theta}\right)^2\right\rangle\\ -2\sin\gamma\cos\gamma\left\langle\frac{\partial\zeta_{2t}}{\partial r}\right\rangle\end{pmatrix}$$

$$-\sin^2\gamma\left(\frac{1}{r^2}\left\langle\frac{\partial\zeta_{1t}}{\partial\theta}\frac{\partial\zeta_{2ct}}{\partial\theta}\right\rangle+\left\langle\frac{\partial\zeta_{1t}}{\partial r}\frac{\partial\zeta_{2ct}}{\partial r}\right\rangle\right)-\zeta_{1c}\left(r,\theta,t\right)\left\langle\zeta_{1t}\left(r,\theta,t\right)\frac{f_{n,zz}\left(r,\theta,\left(r-r_f\right)\cot\gamma,t\right)}{\sin\gamma}\right\rangle$$

$$-\left\langle\zeta_{2ct}\left(r,\theta,t\right)\frac{f_{n,z}\left(r,\theta,\left(r-r_f\right)\cot\gamma,t\right)}{\sin\gamma}\right\rangle-\frac{\partial\zeta_{1c}}{\partial r}\left\langle\zeta_{1t}\left(r,\theta,t\right)f_{u,z}\left(r,\theta,\left(r-r_f\right)\cot\gamma,t\right)\right\rangle$$

$$-\zeta_{1c}\left(r,\theta,t\right)\left\{\left\langle\frac{\partial\zeta_{1t}}{\partial r}f_{u,z}\left(r,\theta,\left(r-r_f\right)\cot\gamma,t\right)\right\rangle+\frac{1}{r}\left\langle\frac{\partial\zeta_{1t}}{\partial\theta}f_{\theta,z}\left(r,\theta,\left(r-r_f\right)\cot\gamma,t\right)\right\rangle\right\}$$

(D.15)

$$\left\langle \zeta_{1t}\left(r,\theta,t\right)^2 \right\rangle = \frac{1}{\cos^2\gamma \sin^4\gamma} \int_{r_f}^{r}\int_{r_f}^{r} d\eta_2 d\eta_1 R_{nn}\left(\eta_1,\eta_2,\theta,\theta,\left(\eta_1-r_f\right)\cot\gamma,\left(\eta_2-r_f\right)\cot\gamma,\left(\eta_2-\eta_1\right)/\cos\gamma\sin\gamma\right) \tag{D.16}$$

$$\begin{aligned}\left\langle \frac{\partial \zeta_{2t}\left(r,\theta,t\right)}{\partial r} \right\rangle = &-\frac{1}{r\cos\gamma\sin\gamma}\left\langle f_\theta\left(r,\theta,\left(r-r_f\right)\cot\gamma,t\right)\frac{\partial\zeta_{1t}}{\partial\theta}\right\rangle \\ &-\frac{\sin\gamma}{2r^2\cos\gamma}\left\langle\left(\frac{\partial\zeta_{1t}}{\partial\theta}\right)^2\right\rangle - \frac{\sin^3\gamma}{\cos\gamma}\left\langle\left(\frac{\partial\zeta_{1t}}{\partial r}\right)^2\right\rangle \\ &-\frac{1}{\cos\gamma\sin\gamma}\left\langle f_u\left(r,\theta,\left(r-r_f\right)\cot\gamma,t\right)\frac{\partial\zeta_{1t}}{\partial r}\right\rangle \\ &+\frac{1}{\cos\gamma\sin^2\gamma}\left\langle \zeta_{1t}\left(r,\theta,t\right) f_{n,z}\left(r,\theta,z=r-r_f,t\right)\right\rangle\end{aligned} \tag{D.17}$$

The correlation $\left\langle \zeta_{2t}\left(r,\theta,t\right)\right\rangle$ can be evaluated by integrating the above *w. r. t. r.*

Next,

$$\left\langle f_\theta\left(r,\theta,\left(r-r_f\right)\cot\gamma,t\right)\frac{\partial\zeta_{2ct}}{\partial\theta}\right\rangle = \frac{\partial}{\partial\phi}\left\langle f_\theta\left(r_1,\theta,\left(r-r_f\right)\cot\gamma,t\right)\zeta_{2ct}\left(r,\phi,t\right)\right\rangle\Big|_{r_1=r,\phi=\theta} \tag{D.18}$$

$$\left\langle f_\theta\left(r,\theta,\left(r-r_f\right)\cot\gamma,t\right)\frac{\partial\zeta_{2ct}}{\partial r}\right\rangle = \frac{\partial}{\partial r}\left\langle f_\theta\left(r_1,\theta,\left(r-r_f\right)\cot\gamma,t\right)\zeta_{2ct}\left(r,\phi,t\right)\right\rangle\Big|_{r_1=r,\phi=\theta} \tag{D.19}$$

The above can be evaluated from the following expression,

$$\left\langle f_\theta\left(r_1,\theta,\left(r_1-r_f\right)\cot\gamma,t\right)\zeta_{2ct}\left(r,\phi,t\right)\right\rangle =$$

$$-\frac{K^2St^2}{2\Lambda^2\sin^2\gamma}\int_{r_f}^{r}d\eta_2\left[\begin{array}{l}\left\langle f_\theta\left(r_1,\theta,\left(r_1-r_f\right)\cot\gamma,t\right)\zeta_{1t}\left(\eta_2,\phi,t-\dfrac{r-\eta_2}{\sin\gamma\cos\gamma}\right)\right\rangle\times \\ \left(\begin{array}{l}\eta_2\cos\left(\dfrac{St}{\Lambda}\left(t-\dfrac{r-\eta_2}{\sin\gamma\cos\gamma}-K\left(\eta_2-r_f\right)\cot\gamma\right)\right) \\ -\dfrac{2\Lambda}{KSt\cot\gamma}\sin\left(\dfrac{St}{\Lambda}\left(t-\dfrac{r-\eta_2}{\sin\gamma\cos\gamma}-K\left(\eta_2-r_f\right)\cot\gamma\right)\right)\end{array}\right)\end{array}\right]$$

$$-\frac{1}{\sin\gamma\cos\gamma}\int_{r_f}^{r}d\eta_2\left\langle\begin{array}{l}f_\theta\left(r_1,\theta,\left(r_1-r_f\right)\cot\gamma,t\right)\times \\ f_u\left(\eta_2,\phi,\left(\eta_2-r_f\right)\cot\gamma,t-\dfrac{r-\eta_2}{\sin\gamma\cos\gamma}\right)\end{array}\right\rangle\frac{\partial\zeta_{1c}\left(\eta_2,\theta,t-\dfrac{r-\eta_2}{\sin\gamma\cos\gamma}\right)}{\partial r}$$

$$+\frac{1}{2\sin\gamma\cos\gamma}\int_{r_f}^{r}d\eta_2K\eta_2\frac{St}{\Lambda}\left[\begin{array}{l}\left\langle f_\theta\left(r_1,\theta,\left(r_1-r_f\right)\cot\gamma,t\right)\dfrac{\partial\zeta_{1t}}{\partial r}\Big|_{\left(\eta_2,\phi,t-\frac{r-\eta_2}{\sin\gamma\cos\gamma}\right)}\right\rangle \\ \sin\left(\dfrac{St}{\Lambda}\left(t-\dfrac{r-\eta_2}{\sin\gamma\cos\gamma}-K\left(\eta_2-r_f\right)\cot\gamma\right)\right)\end{array}\right]$$

$$-\frac{\sin^3\gamma}{\cos\gamma}\int_{r_f}^{r}d\eta_2\frac{\partial\zeta_{1c}\left(\eta_2,\theta,t-\dfrac{r-\eta_2}{\sin\gamma\cos\gamma}\right)}{\partial r}\left\langle f_\theta\left(r_1,\theta,\left(r_1-r_f\right)\cot\gamma,t\right)\frac{\partial\zeta_{1t}}{\partial r}\Big|_{\left(\eta_2,\phi,t-\frac{r-\eta_2}{\sin\gamma\cos\gamma}\right)}\right\rangle$$

$$-\frac{1}{\sin^2\gamma\cos\gamma}\int_{r_f}^{r}d\eta_2\zeta_{1c}\left(\eta_2,\theta,t-\frac{r-\eta_2}{\sin\gamma\cos\gamma}\right)\left\langle\begin{array}{l}f_\theta\left(r_1,\theta,\left(r_1-r_f\right)\cot\gamma,t\right)\times \\ f_{n,z}\left(\eta_2,\phi,\left(\eta_2-r_f\right)\cot\gamma,t-\dfrac{r-\eta_2}{\sin\gamma\cos\gamma}\right)\end{array}\right\rangle \tag{D.20}$$

The correlations in the above are as follows,

$$\left\langle f_\theta\left(r_1,\theta,\left(r_1-r_f\right)\cot\gamma,t\right)\zeta_{1t}\left(\eta_2,\phi,t-\frac{r-\eta_2}{\sin\gamma\cos\gamma}\right)\right\rangle$$

$$=\frac{1}{\cos\gamma\sin^2\gamma}\int_{r_f}^{\eta_2}d\eta_1\,R_{\theta n}\left(\eta_1,r_1,\phi,\theta,\left(\eta_1-r_f\right)\cot\gamma,\left(r_1-r_f\right)\cot\gamma,\left(r-\eta_1\right)/\cos\gamma\sin\gamma\right)\Big|_{\theta=\phi} \tag{D.21}$$

$$\left\langle f_\theta\left(r_1,\theta,\left(r_1-r_f\right)\cot\gamma,t\right) f_u\left(\eta_2,\phi,\left(\eta_2-r_f\right)\cot\gamma,t-\frac{r-\eta_2}{\sin\gamma\cos\gamma}\right)\right\rangle$$
$$= R_{\theta u}\left(\eta_2,r_1,\theta,\phi,\left(\eta_2-r_f\right)\cot\gamma,\left(r_1-r_f\right)\cot\gamma,\left(r-\eta_2\right)/\cos\gamma\sin\gamma\right)\Big|_{\theta=\phi} \tag{D.22}$$

$$\left\langle f_\theta\left(r_1,\theta,\left(r_1-r_f\right)\cot\gamma,t\right)\frac{\partial\zeta_{1t}}{\partial r}\Big|_{\left(\eta_2,\phi,t-\frac{r-\eta_2}{\sin\gamma\cos\gamma}\right)}\right\rangle$$
$$= \frac{1}{\cos\gamma\sin^2\gamma} R_{\theta n}\left(\eta_2,r_1,\phi,\theta,\left(\eta_2-r_f\right)\cot\gamma,\left(r_1-r_f\right)\cot\gamma,\left(r-\eta_2\right)/\sin\gamma\cos\gamma\right) \tag{D.23}$$
$$+\frac{1}{\cos^2\gamma\sin^3\gamma}\int_{r_f}^{\eta_2} d\eta_1 \frac{\partial R_{\theta n}\left(\eta_1,r_1,\phi,\theta,\left(\eta_1-r_f\right)\cot\gamma,\left(r_1-r_f\right)\cot\gamma,\tau\right)}{\partial\tau}\Big|_{\substack{\theta=\phi \\ \tau=\left(r-\eta_1\right)/\sin\gamma\cos\gamma}}$$

$$\left\langle f_\theta\left(r,\theta,\left(r-r_f\right)\cot\gamma,t\right) f_{n,z\theta}\left(\eta_2,\theta,\left(\eta_2-r_f\right)\cot\gamma,t-\frac{r-\eta_2}{\sin\gamma\cos\gamma}\right)\right\rangle$$
$$= \frac{\partial^2}{\partial\phi\partial z} R_{\theta n}\left(\eta_2,r,\phi,\theta,z,\left(r-r_f\right)\cot\gamma,\left(r-\eta_2\right)/\sin\gamma\cos\gamma\right)\Big|_{\phi=\theta,z=\left(\eta_2-r_f\right)\cot\gamma} \tag{D.24}$$

$$\left\langle f_\theta\left(r_1,\theta,\left(r_1-r_f\right)\cot\gamma,t\right) f_{n,z}\left(\eta_2,\phi,\left(\eta_2-r_f\right)\cot\gamma,t-\frac{r-\eta_2}{\sin\gamma\cos\gamma}\right)\right\rangle$$
$$= \frac{\partial R_{\theta n}\left(\eta_2,r_1,\phi,\theta,z_1,\left(r_1-r_f\right)\cot\gamma,\left(r-\eta_2\right)/\sin\gamma\cos\gamma\right)}{\partial z}\Big|_{z_1=\left(\eta_2-r_f\right)\cot\gamma} \tag{D.25}$$

Next,

$$\left\langle \zeta_{2ct}\left(r,\theta,t\right)\frac{f_{n,z}\left(r,\theta,\left(r-r_f\right)\cot\gamma,t\right)}{\sin\gamma}\right\rangle$$

$$=\frac{-1}{\sin^2\gamma\cos\gamma}\int_{r_f}^{r}d\eta_2\left\langle\begin{matrix}\zeta_{1t}\left(\eta_2,\theta,t-\dfrac{r-\eta_2}{\sin\gamma\cos\gamma}\right)\\ f_{n,z}\left(r,\theta,\left(r-r_f\right)\cot\gamma,t\right)\end{matrix}\right\rangle\left(\begin{matrix}\dfrac{1}{2}K^2\eta_2\left(\dfrac{St}{\Lambda}\right)^2\cos\left(\dfrac{St}{\Lambda}\left(\begin{matrix}t-\dfrac{r-\eta_2}{\sin\gamma\cos\gamma}\\ -K\left(\eta_2-r_f\right)\cot\gamma\end{matrix}\right)\right)\cot\gamma\\ -\dfrac{KSt}{\Lambda}\sin\left(\dfrac{St}{\Lambda}\left(\begin{matrix}t-\dfrac{r-\eta_2}{\sin\gamma\cos\gamma}\\ -K\left(\eta_2-r_f\right)\cot\gamma\end{matrix}\right)\right)\end{matrix}\right)$$

$$-\frac{1}{\sin^2\gamma\cos\gamma}\int_{r_f}^{r}d\eta_2\left\langle\begin{matrix}f_u\left(\eta_2,\theta,\left(\eta_2-r_f\right)\cot\gamma,t-\dfrac{r-\eta_2}{\sin\gamma\cos\gamma}\right)\\ f_{n,z}\left(r,\theta,\left(r-r_f\right)\cot\gamma,t\right)\end{matrix}\right\rangle\frac{\partial\zeta_{1c}\left(\eta_2,\theta,t-\dfrac{r-\eta_2}{\sin\gamma\cos\gamma}\right)}{\partial r}$$

$$+\frac{1}{2\sin^2\gamma\cos\gamma}\int_{r_f}^{r}d\eta_2\eta_2\left(\frac{KSt}{\Lambda}\right)\left\langle\begin{matrix}f_{n,z}\left(r,\theta,\left(r-r_f\right)\cot\gamma,t\right)\\ \left.\dfrac{\partial\zeta_{1t}}{\partial r}\right|_{\left(\eta_2,\theta,t-\frac{r-\eta_2}{\sin\gamma\cos\gamma}\right)}\end{matrix}\right\rangle\sin\left(\frac{St}{\Lambda}\left(\begin{matrix}t-\dfrac{r-\eta_2}{\sin\gamma\cos\gamma}\\ -K\left(\eta_2-r_f\right)\cot\gamma\end{matrix}\right)\right)$$

$$-\frac{\sin^2\gamma}{\cos\gamma}\int_{r_f}^{r}d\eta_2\frac{\partial\zeta_{1c}\left(\eta_2,\theta,t-\dfrac{r-\eta_2}{\sin\gamma\cos\gamma}\right)}{\partial r}\left\langle f_{n,z}\left(r,\theta,\left(r-r_f\right)\cot\gamma,t\right)\left.\frac{\partial\zeta_{1t}}{\partial r}\right|_{\left(\eta_2,\theta,t-\frac{r-\eta_2}{\sin\gamma\cos\gamma}\right)}\right\rangle$$

$$-\frac{1}{\sin^3\gamma\cos\gamma}\int_{r_f}^{r}d\eta_2\zeta_{1c}\left(\eta_2,\theta,t-\frac{r-\eta_2}{\sin\gamma\cos\gamma}\right)\left\langle\begin{matrix}f_{n,z}\left(r,\theta,\left(r-r_f\right)\cot\gamma,t\right)\\ f_{n,z}\left(\eta_2,\theta,\left(\eta_2-r_f\right)\cot\gamma,t-\dfrac{r-\eta_2}{\sin\gamma\cos\gamma}\right)\end{matrix}\right\rangle \tag{D.26}$$

$$\left\langle f_{n,z}\left(r,\theta,\left(r-r_f\right)\cot\gamma,t\right)f_u\left(\eta_2,\theta,\left(\eta_2-r_f\right)\cot\gamma,t-\frac{r-\eta_2}{\sin\gamma\cos\gamma}\right)\right\rangle$$

$$=\left.\frac{\partial R_{un}\left(r,\eta_2,\theta,\theta,z_1,\left(\eta_2-r_f\right)\cot\gamma,\left(r-\eta_2\right)/\sin\gamma\cos\gamma\right)}{\partial z_1}\right|_{z_1=\left(r-r_f\right)\cot\gamma} \tag{D.27}$$

$$\left\langle \begin{matrix} f_{n,z}\left(r,\theta,\left(r-r_f\right)\cot\gamma,t\right) \\ f_{n,z}\left(\eta_2,\theta,\left(\eta_2-r_f\right)\cot\gamma,t-\dfrac{r-\eta_2}{\sin\gamma\cos\gamma}\right) \end{matrix} \right\rangle$$
$$= \frac{\partial^2}{\partial z_1 \partial z_2} R_{nn}\left(r,\eta_2,\theta,\theta,z_1,z_2,\left(r-\eta_2\right)/\sin\gamma\cos\gamma\right)\Big|_{\substack{z_1=\left(r-r_f\right)\cot\gamma \\ z_2=\left(\eta_2-r_f\right)\cot\gamma}} \tag{D.28}$$

$$\left\langle f_{n,z}\left(r,\theta,\left(r-r_f\right)\cot\gamma,t\right)\frac{\partial\zeta_{1t}}{\partial r}\Big|_{\left(\eta_2,\theta,t-\frac{r-\eta_2}{\sin\gamma\cos\gamma}\right)}\right\rangle$$
$$= \frac{1}{\cos\gamma\sin^2\gamma}\frac{\partial R_{nn}\left(r,\eta_2,\theta,\theta,z,\left(\eta_2-r_f\right)\cot\gamma,\left(r-\eta_2\right)/\sin\gamma\cos\gamma\right)}{\partial z}\Big|_{z=\left(r-r_f\right)\cot\gamma} \tag{D.29}$$
$$+\frac{1}{\cos^2\gamma\sin^3\gamma}\int_{r_f}^{\eta_2}\frac{\partial^2 R_{nn}\left(\eta_1,r,\theta,\theta,\left(\eta_1-r_f\right)\cot\gamma,z,\tau\right)}{\partial z\partial\tau}\Big|_{z=\left(\eta_2-r_f\right)\cot\gamma,\tau=\frac{r-\eta_1}{\sin\gamma\cos\gamma}} d\eta_1$$

$$\left\langle f_{n,z}\left(r,\theta,\left(r-r_f\right)\cot\gamma,t\right)\frac{\partial\zeta_{1t}\left(\eta_2,\theta,t-\dfrac{r-\eta_2}{\sin\gamma\cos\gamma}\right)}{\partial r}\right\rangle$$
$$= \frac{1}{\cos\gamma\sin^2\gamma}\frac{\partial R_{nn}\left(\eta_2,r,\theta,\theta,\left(\eta_2-r_f\right)\cot\gamma,z,\left(r-\eta_2\right)/\sin\gamma\cos\gamma\right)}{\partial z}\Big|_{z=\left(r-r_f\right)\cot\gamma} \tag{D.30}$$
$$+\frac{1}{\cos^2\gamma\sin^3\gamma}\int_{r_f}^{\eta_2}\frac{\partial^2 R_{nn}\left(\eta_1,r,\theta,\theta,\left(\eta_1-r_f\right)\cot\gamma,z,\tau\right)}{\partial z\partial\tau}\Big|_{z=\left(r-r_f\right)\cot\gamma,\tau=\frac{r-\eta_1}{\sin\gamma\cos\gamma}} d\eta_1$$

$$\left\langle \zeta_{1t}\left(r,\theta,t\right)\frac{f_{n,zz}\left(r,\theta,\left(r-r_f\right)\cot\gamma,t\right)}{\sin\gamma}\right\rangle$$
$$= \frac{1}{\cos\gamma\sin^3\gamma}\int_{r_f}^{r}\frac{\partial^2 R_{nn}\left(r,\eta_1,z,\left(\eta_1-r_f\right)\cot\gamma,\left(r-\eta_1\right)/\cos\gamma\sin\gamma\right)}{\partial z^2}\Big|_{z=\left(r-r_f\right)\cot\gamma} d\eta_1 \tag{D.31}$$

$$\left\langle \frac{\partial \zeta_{1t}}{\partial \theta} f_{\theta,z}\left(r,\theta,\left(r-r_f\right)\cot\gamma,t\right)\right\rangle$$
$$= \frac{1}{\cos\gamma\sin^2\gamma}\int_{r_f}^{r} d\eta_1 \frac{\partial^2}{\partial\theta\partial z} R_{\theta n}\left(\eta_1,r,\theta,\phi,\left(\eta_1-r_f\right)\cot\gamma,z,\left(r-\eta_1\right)/\cos\gamma\sin\gamma\right)\Big|_{\phi=\theta,z=\left(r-r_f\right)\cot\gamma}$$

(D.32)

$$\left\langle \frac{\partial \zeta_{1t}}{\partial r} f_{u,z}\left(r,\theta,\left(r-r_f\right)\cot\gamma,t\right)\right\rangle$$
$$= \frac{1}{\cos\gamma\sin^2\gamma}\frac{\partial R_{un}\left(r,r,\theta,\theta,z,\left(r-r_f\right)\cot\gamma,0\right)}{\partial z}\Big|_{z=\left(r-r_f\right)\cot\gamma} \qquad \text{(D.33)}$$
$$+\frac{1}{\cos^2\gamma\sin^3\gamma}\left\langle \int_{r_f}^{r}\frac{\partial^2}{\partial z\partial\tau} R_{un}\left(\eta_1,r,\theta,\theta,\left(\eta_1-r_f\right)\cot\gamma,z,\tau\right)\Big|_{z=\left(r-r_f\right)\cot\gamma,\tau=\frac{(r-\eta_1)}{\cos\gamma\sin\gamma}} d\eta_1\right\rangle$$

Appendix E

Turbulence correction – Strouhal number dependence

This chapter presents an analysis of the expressions presented in Appendix D in order to elucidate the role of turbulence Strouhal number $St_{c,Turb} = \omega L_{11}/u_c$. The analysis is presented in terms of the time domain expressions for the turbulence correction in the interest of readability. Specifically, the Strouhal number dependence of kinematic coupling terms comprising the leading order turbulence correction to the laminar transfer function will be examined. These terms have the following general form,

$$\frac{\partial^a R_{\alpha\beta}}{\partial z^b \partial \theta^c \partial \phi^d \partial r^e} B \tag{E.1}$$

where, $R_{\alpha\beta}$ can be any of the correlations used in the above expressions. The indices *a-e* are integers that take values from 0-3 as appropriate. The quantity $\underline{B}$ can in general be ζ_{1c} or its higher order derivatives or just trigonometric functions in terms of *St*, *K* and *t*. Note that the derivative of $R_{\alpha\beta}$ on the above is independent of *St* and hence does not vary with changes in Strouhal number. Hence, it is useful to determine the Strouhal number scaling in general of the other derivative in the above.

Thus, the solution for ζ_{1c} is given by the following,

$$\zeta_{1c}(r,t)=\frac{Kr}{\left(-2+2K\cos^2\gamma\right)}\cos\left[\frac{St}{\Lambda}\left(t+K\left(r-r_f\right)\cot\gamma\right)\right]$$
$$-\frac{Kr_f}{\left(-2+2K\cos^2\gamma\right)}\cos\left[\frac{St}{\Lambda}\left(t-\frac{K\left(r-r_f\right)}{\sin\gamma\cos\gamma}\right)\right] \tag{E.2}$$
$$-\frac{\Lambda\left(-4+4K\cos^2\gamma-2K\sin\gamma\cos\gamma\right)}{St\left(-2+2K\cos^2\gamma\right)^2}\left\{\begin{array}{l}\sin\left[\frac{St}{\Lambda}\left(t+K\left(r-r_f\right)\cot\gamma\right)\right]\\ -\sin\left[\frac{St}{\Lambda}\left(t-\frac{K\left(r-r_f\right)}{\sin\gamma\cos\gamma}\right)\right]\end{array}\right\}$$

Replacing $St=\frac{\Lambda}{K}St_{c,Turb}$, the above becomes,

$$\zeta_{1c}(r,t)=\frac{Kr}{\left(-2+2K\cos^2\gamma\right)}\cos\left[\frac{St_{c,Turb}}{K}\left(t+K\left(r-r_f\right)\cot\gamma\right)\right]$$
$$-\frac{Kr_f}{\left(-2+2K\cos^2\gamma\right)}\cos\left[\frac{St_{c,Turb}}{K}\left(t-\frac{K\left(r-r_f\right)}{\sin\gamma\cos\gamma}\right)\right]$$
$$-\frac{K\left(-4+4K\cos^2\gamma-2K\sin\gamma\cos\gamma\right)}{2\pi St_{c,Turb}\left(-2+2K\cos^2\gamma\right)^2}\left\{\begin{array}{l}\sin\left[\frac{St_{c,Turb}}{K}\left(t+K\left(r-r_f\right)\cot\gamma\right)\right]\\ -\sin\left[\frac{St_{c,Turb}}{K}\left(t-\frac{K\left(r-r_f\right)}{\sin\gamma\cos\gamma}\right)\right]\end{array}\right\}$$

(E.3)

Clearly, $\zeta_{1c}(r,t)$ can be written as follows $\zeta_{1c}(r,t)=F_{1c}\left(K,\gamma,St_{c,Turb}\right)$. It follows from eq. (E.3) that $\partial^m\zeta_{1c}/\partial r^m$ is $O\left(St_{c,Turb}^m\right)$ is also a function K, γ and $St_{c,Turb}$ as well.

Next, each of the kinematic coupling terms can be in Appendix D can be expressed as a function K, γ and $St_{c,Turb}$. Further, the high frequency scaling of these terms can be determined by integrating each term successively by parts. An example of this is shown

for one term below. The term that is leading order in $St_{c,Turb}$ (denoted by $LOT[\bullet]$) in eq. (D.26) can be analyzed as follows (*St* has been replaced by $St_{c,Turb}$),

$$LOT\left[\left\langle \zeta_{2ct}(r,\theta,t)\frac{f_{n,z}\left(r,\theta,(r-r_f)\cot\gamma,t\right)}{\sin\gamma}\right\rangle\right]St=\frac{\Lambda}{K}St_{c,Turb}$$

$$=\frac{-St_{c,Turb}^2}{2\sin^3\gamma}\int_{r_f}^{r}d\eta_2\left\langle\begin{matrix}\zeta_{1t}\left(\eta_2,\theta,t-\dfrac{r-\eta_2}{\sin\gamma\cos\gamma}\right)\\ f_{n,z}\left(r,\theta,(r-r_f)\cot\gamma,t\right)\end{matrix}\right\rangle\left(\eta_2\cos\left(\frac{St_{c,Turb}}{K}\left(t-\frac{r-\eta_2}{\sin\gamma\cos\gamma}-K(\eta_2-r_f)\cot\gamma\right)\right)\right)$$

$$=\frac{-St_{c,Turb}^2}{2\sin^3\gamma}\left\{\left\langle\begin{matrix}\zeta_{1t}\left(\eta_2,\theta,t-\dfrac{r-\eta_2}{\sin\gamma\cos\gamma}\right)\\ f_{n,z}\left(r,\theta,(r-r_f)\cot\gamma,t\right)\end{matrix}\right\rangle\eta_2\cos\left(\frac{St_{c,Turb}}{K}\left(\begin{matrix}t-\dfrac{r-\eta_2}{\sin\gamma\cos\gamma}\\ -K(\eta_2-r_f)\cot\gamma\end{matrix}\right)\right)\right|_{r_f}^{r}\right\}$$

$$+\frac{St_{c,Turb}(K\cos\gamma)}{2\sin^2\gamma\left(1-K\cos^2\gamma\right)}\int_{r_f}^{r}d\eta_2\frac{\partial}{\partial\eta_2}\left\{\left\langle\begin{matrix}\zeta_{1t}\left(\eta_2,\theta,t-\dfrac{r-\eta_2}{\sin\gamma\cos\gamma}\right)\\ f_{n,z}\left(r,\theta,(r-r_f)\cot\gamma,t\right)\end{matrix}\right\rangle\eta_2\right\}\sin\left(\frac{2\pi}{K}St_{c,Turb}\left(\begin{matrix}t-\dfrac{r-\eta_2}{\sin\gamma\cos\gamma}\\ -K(\eta_2-r_f)\cot\gamma\end{matrix}\right)\right) \tag{E.4}$$

Prolonging the above process *ad infinitum* shows that the LHS is $O\left(St_{c,Turb}^2\right)$ to leading order for $St_{c,Turb}$>1. The other coupling terms may be similarly analyzed. The results are summarized below,

$$\left\langle \zeta_{2ct}(r,\theta,t)\frac{f_{n,z}\left(r,\theta,(r-r_f)\cot\gamma,t\right)}{\sin\gamma}\right\rangle\sim O\left(St_{c,Turb}^2\right) \tag{E.5}$$

$$\left\langle f_\theta\left(r_1,\theta,(r_1-r_f)\cot\gamma,t\right)\zeta_{2ct}(r,\phi,t)\right\rangle\sim O\left(St_{c,Turb}^2\right) \tag{E.6}$$

$$\left\langle \zeta_{1t}(r_1,\phi,t)\zeta_{2ct}(r,\theta,t)\right\rangle\sim O\left(St_{c,Turb}^2\right) \tag{E.7}$$

From eq. (D.15), the above results yield (at leading order, $St_{c,Turb}$>1),

$$\left\langle \frac{\partial \zeta_{3ctt}}{\partial r} \right\rangle \sim O\left(St_{c,Turb}^2\right) \tag{E.8}$$

$$\left\langle \frac{\partial \zeta_{1t}}{\partial r} \frac{\partial \zeta_{2ct}}{\partial r} \right\rangle \sim O\left(St_{c,Turb}\right) \tag{E.9}$$

$$\left\langle \frac{\partial \zeta_{1t}}{\partial \theta} \frac{\partial \zeta_{2ct}}{\partial \theta} \right\rangle \sim O\left(St_{c,Turb}\right) \tag{E.10}$$

Thus it is clear from the above results and equation for the turbulence correction (eq. (6.19)) that

$$F_T\left(St\right) \sim O\left(St_{c,Turb}^2\right) \tag{E.11}$$

The above result implies that the turbulence correction grows rapidly as $St_{c,Turb}$ becomes large, i.e. as the convective length scale of the coherent fluctuations becomes comparable to turbulence length scales as shown in chapter 7. Thus, higher order terms must be included to balance this effect.

It is also possible to gain insight into the behaviour of these coupling terms with varying *K* and a fixed value of *St*. The leading order term in eq. (D.26) yields,

$$
\begin{aligned}
&LOT\left[\left\langle \zeta_{2ct}\left(r,\theta,t\right)\frac{f_{n,z}\left(r,\theta,\left(r-r_f\right)\cot\gamma,t\right)}{\sin\gamma}\right\rangle\right]\\
&=\frac{-K^2St^2}{2\Lambda^2\sin^3\gamma}\int_{r_f}^{r}d\eta_2\left\langle\begin{matrix}\zeta_{1t}\left(\eta_2,\theta,t-\dfrac{r-\eta_2}{\sin\gamma\cos\gamma}\right)\\ f_{n,z}\left(r,\theta,\left(r-r_f\right)\cot\gamma,t\right)\end{matrix}\right\rangle\left(\eta_2\cos\left(\frac{St}{\Lambda}\left(t-\frac{r-\eta_2}{\sin\gamma\cos\gamma}-K\left(\eta_2-r_f\right)\cot\gamma\right)\right)\right)\\
&=\frac{-K^2}{2\sin^3\gamma}\left(\frac{St}{\Lambda}\right)^2\left\{\left\langle\begin{matrix}\zeta_{1t}\left(\eta_2,\theta,t-\dfrac{r-\eta_2}{\sin\gamma\cos\gamma}\right)\\ f_{n,z}\left(r,\theta,\left(r-r_f\right)\cot\gamma,t\right)\end{matrix}\right\rangle\eta_2\cos\left(\frac{St}{\Lambda}\left(\begin{matrix}t-\dfrac{r-\eta_2}{\sin\gamma\cos\gamma}\\ -K\left(\eta_2-r_f\right)\cot\gamma\end{matrix}\right)\right)\right|_{r_f}^{r}\right\}\\
&+\left(\frac{St}{\Lambda}\right)\frac{K^2\cos\gamma}{2\sin^2\gamma\left(1-K\cos^2\gamma\right)}\int_{r_f}^{r}d\eta_2\frac{\partial}{\partial\eta_2}\left\{\left\langle\begin{matrix}\zeta_{1t}\left(\eta_2,\theta,t-\dfrac{r-\eta_2}{\sin\gamma\cos\gamma}\right)\\ f_{n,z}\left(r,\theta,\left(r-r_f\right)\cot\gamma,t\right)\end{matrix}\right\rangle\eta_2\right\}\sin\left(\frac{St}{\Lambda}\left(\begin{matrix}t-\dfrac{r-\eta_2}{\sin\gamma\cos\gamma}\\ -K\left(\eta_2-r_f\right)\cot\gamma\end{matrix}\right)\right)
\end{aligned}
\tag{E.12}
$$

Notice, that the net result of one step of integration by parts produces a factor of $\left(\Lambda/St\right)\left\{K\cos\gamma\sin\gamma/\left(1-K\cos^2\gamma\right)\right\}$ in front of the trailing integral. Thus prolonging this procedure *ad infinitum* yields in a series in terms of the above quantity with coefficients that have the exact same form as coupling terms. Thus with all other parameters held constant these terms that yield a series in the above parameter vanish as $K\rightarrow 0$ resulting in weak kinematic coupling. This fact is borne out by the delayed high strouhal number increase (relative to K > 0 cases) in the value of the turbulence correction term for the K = 0 case.

Appendix F

Turbulence Correlation Functions

This appendix derives a general framework to evaluate the various spatio-temporal correlation functions used in the present work. This derivation is presented in dimensional form for clarity and ease of understanding. A constant uniform mean flow and Taylor's hypothesis is assumed. Thus, consider any two arbitrary points (labeled '1' and '2') chosen to be an distance *s* apart as shown schematically in fig. F-1. Also shown are a system of unit vectors that will be used in the present derivation. It is required to find the spatio-temporal correlation between velocity fluctuations along directions given by unit vectors $\hat{e}_{n1}$ and $\hat{e}_{n1}$ as shown in fig. F-1. If the position vectors of these points '1' and '2'are denoted by $\vec{x}_1$ and $\vec{x}_2$ respectively, this correlation function, denoted by $R_{n1n2}\left(s\hat{e}_s,\tau\right)$, can be written as follows.

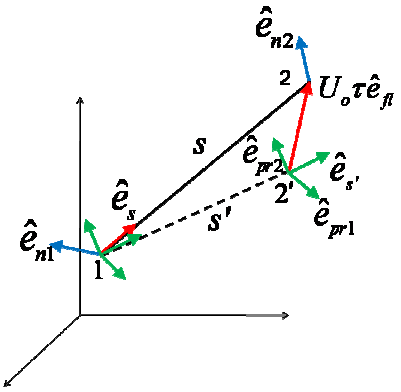

Figure F-1: Schematic of vector system used to evaluate space time correlation functions between points 1 and 2 separated by distance *s*. Co-ordinate axes for reference only. No assumptions have been made about the underlying co-ordinate system representation of the vectors.

$$R_{n1n2}\left(s\hat{e}_s,\tau\right)=\left\langle\left\{\vec{u}\left(\vec{x}_1,t\right)\cdot\hat{e}_{n1}\right\}\left\{\vec{u}\left(\vec{x}_2,t+\tau\right)\cdot\hat{e}_{n2}\right\}\right\rangle \tag{F.1}$$

Assuming Taylor's hypothesis, the above can be re-written as below,

$$R_{n1n2}\left(s\hat{e}_s,\tau\right)=\left\langle\left\{\vec{u}\left(\vec{x}_1,t\right)\cdot\hat{e}_{n1}\right\}\left\{\vec{u}\left(\vec{x}_2-\left(U_o\tau\right)\hat{e}_{fl},t\right)\cdot\hat{e}_{n2}\right\}\right\rangle \tag{F.2}$$

Notice that the RHS of the above is now the spatial correlation between points 1 and 2′ as shown by fig. F-1, where the position vector of the point 2′ is given by, $\vec{x}_2-\left(U_o\tau\right)\hat{e}_{fl}$. The unit vector $\hat{e}_{fl}$ is aligned along the direction of the mean flow. It is now possible to define an orthogonal system of unit vectors, $\hat{e}_{s'},\hat{e}_{pr1}$ and $\hat{e}_{pr2}$ at points 1 and 2′ as follows.

$$\begin{aligned}
\hat{e}_{s'}&=\frac{s\hat{e}_s-U_o\tau\hat{e}_{fl}}{\sqrt{s^2+U_o^2\tau^2-2U_o\tau s\left(\hat{e}_s\bullet\hat{e}_{fl}\right)}}\\
\hat{e}_{pr1}=\hat{e}_{s'}\times\hat{e}_{pr2}&=\frac{s\hat{e}_s\times\left(\hat{e}_s\times\hat{e}_{fl}\right)-U_o\tau\hat{e}_{fl}\times\left(\hat{e}_s\times\hat{e}_{fl}\right)}{\left|\hat{e}_s\times\hat{e}_{fl}\right|\sqrt{s^2+U_o^2\tau^2-2U_o\tau s\left(\hat{e}_s\bullet\hat{e}_{fl}\right)}}\\
\hat{e}_{pr2}&=\frac{\hat{e}_s\times\hat{e}_{fl}}{\left|\hat{e}_s\times\hat{e}_{fl}\right|}
\end{aligned} \tag{F.3}$$

Next, the velocities in eq. (F.2) can be written in terms of components along the above directions to yield the following

$$R_{n1n2}\left(s\hat{e}_s,\tau\right)=\left\langle\begin{Bmatrix}\left\{u_{s'}\left(\vec{x}_1,t\right)\left(\hat{e}_s\cdot\hat{e}_{n1}\right)+u_{pr1}\left(\vec{x}_1,t\right)\left(\hat{e}_{pr1}\cdot\hat{e}_{n1}\right)+u_{pr2}\left(\vec{x}_1,t\right)\left(\hat{e}_{pr2}\cdot\hat{e}_{n1}\right)\right\}\\ \left\{u_{s'}\left(\vec{x}_2-\left(U_o\tau\right)\hat{e}_{fl},t\right)\left(\hat{e}_s\cdot\hat{e}_{n2}\right)+u_{pr1}\left(\vec{x}_2-\left(U_o\tau\right)\hat{e}_{fl},t\right)\left(\hat{e}_{pr1}\cdot\hat{e}_{n2}\right)\right\}\\ +u_{pr2}\left(\vec{x}_2-\left(U_o\tau\right)\hat{e}_{fl},t\right)\left(\hat{e}_{pr2}\cdot\hat{e}_{n2}\right)\end{Bmatrix}\right\rangle \tag{F.4}$$

Since the turbulence field is isotropic, the above can be written in terms of the longitudinal and lateral correlation functions of the isotropic turbulence as follows,

$$R_{n1n2}\left(s\hat{e}_s,\tau\right)=R_{11}\left(s'\right)\left(\hat{e}_s\cdot\hat{e}_{n1}\right)\left(\hat{e}_s\cdot\hat{e}_{n2}\right)+R_{22}\left(s'\right)\left\{\left(\hat{e}_{pr1}\cdot\hat{e}_{n1}\right)\left(\hat{e}_{pr1}\cdot\hat{e}_{n2}\right)+\left(\hat{e}_{pr2}\cdot\hat{e}_{n1}\right)\left(\hat{e}_{pr2}\cdot\hat{e}_{n2}\right)\right\} \tag{F.5}$$

where, $s' = \sqrt{s^2 + U_o^2\tau^2 - 2U_o\tau s\left(\hat{e}_s \bullet \hat{e}_{fl}\right)}$ i.e., the spatial separation between points 1 and 2'.

The dot products in eq. (F.5) can be written in terms of $\hat{e}_s$ and $\hat{e}_{fl}$ as below,

$$\begin{aligned}
\hat{e}_{s'} \bullet \hat{e}_{n1} &= \frac{s\left(\hat{e}_s \bullet \hat{e}_{n1}\right) - U_o\tau\left(\hat{e}_{fl} \bullet \hat{e}_{n1}\right)}{\sqrt{s^2 + U_o^2\tau^2 - 2U_o\tau s\left(\hat{e}_s \bullet \hat{e}_{fl}\right)}} \\
\hat{e}_{pr1} \bullet \hat{e}_{n1} &= \frac{\left(s\left(\hat{e}_s \bullet \hat{e}_{fl}\right) - U_o\tau\right)\left(\hat{e}_s \bullet \hat{e}_{n1}\right) + \left(U_o\tau\left(\hat{e}_s \bullet \hat{e}_{fl}\right) - s\right)\left(\hat{e}_{fl} \bullet \hat{e}_{n1}\right)}{\sqrt{\left(s^2 + \left(U_o\tau\right)^2 - 2sU_o\tau\left(\hat{e}_s \bullet \hat{e}_{fl}\right)\right)\left(1 - \left(\hat{e}_s \bullet \hat{e}_{fl}\right)^2\right)}} \\
\hat{e}_{pr2} \bullet \hat{e}_{n1} &= \frac{\left(\hat{e}_s \times \hat{e}_{fl}\right) \bullet \hat{e}_{n1}}{\left|\hat{e}_s \times \hat{e}_{fl}\right|}
\end{aligned} \tag{F.6}$$

The corresponding dot products with $\hat{e}_{n2}$ can be determined by replacing $\hat{e}_{n1}$ in the above with $\hat{e}_{n2}$. Finally, mass conservation for incompressible flows implies that (ref. Pope[42]),

$$R_{22}\left(s'\right) = R_{11}\left(s'\right) + \frac{s'}{2}\frac{\partial R_{11}\left(s'\right)}{\partial s'} \tag{F.7}$$

Thus, eqs. (F.5)-(F.7) represent the complete set of results that are needed to determine $R_{n1n2}\left(s\hat{e}_s, \tau\right)$. Next, the specific values of the above unit vectors for spatio-temporal correlation functions that arise in the theoretical analysis presented in this work are presented. These will be presented in non-dimensional form using the same non-dimensionalization scheme used throughout the present work.

Unforced flame analysis:

The only correlation that is requires is the correlation between the fluctuating velocity components along the normal to the nominal flame surface at two distinct points on the surface. Thus, the set of vectors needed to evaluate R_{22} are as follows,

$$\hat{e}_s = \frac{\sigma_s \sin\gamma \hat{e}_x + \sigma_y \hat{e}_y + \sigma_s \cos\gamma \hat{e}_z}{\sqrt{\sigma_s^2 + \sigma_y^2}}$$
$$\hat{e}_{fl} = \hat{e}_z \tag{F.8}$$
$$\hat{e}_{n1} = \hat{e}_{n2} = -\cos\gamma \hat{e}_x + \sin\gamma \hat{e}_z$$

Forced flame analysis:

It is useful to formulate correlation functions between two general points in space in order to evaluate the various terms that characterize the turbulence correction to the heat release transfer function. These are as follows,

Normal-normal correlation $\left(R_{nn}\right)$:

$$\hat{e}_s = \frac{\left(\eta_2 \cos\theta - \eta_1 \cos\phi\right)\hat{e}_x + \left(\eta_2 \sin\theta - \eta_1 \sin\phi\right)\hat{e}_y + \left(z_2 - z_1\right)\hat{e}_z}{\sqrt{\eta_1^2 + \eta_2^2 - 2\eta_1\eta_2 \cos\left(\theta - \phi\right) + \left(z_2 - z_1\right)^2}}$$
$$\hat{e}_{fl} = \hat{e}_z \tag{F.9}$$
$$\hat{e}_{n1} = -\cos\gamma\left(\cos\phi \hat{e}_x + \sin\phi \hat{e}_y\right) + \sin\gamma \hat{e}_z$$
$$\hat{e}_{n2} = -\cos\gamma\left(\cos\theta \hat{e}_x + \sin\theta \hat{e}_y\right) + \sin\gamma \hat{e}_z$$

Normal-radial correlation $\left(R_{nu}\right)$:

$$\hat{e}_s = \frac{\left(\eta_2 \cos\theta - \eta_1 \cos\phi\right)\hat{e}_x + \left(\eta_2 \sin\theta - \eta_1 \sin\phi\right)\hat{e}_y + \left(z_2 - z_1\right)\hat{e}_z}{\sqrt{\eta_1^2 + \eta_2^2 - 2\eta_1\eta_2 \cos\left(\theta - \phi\right) + \left(z_2 - z_1\right)^2}}$$
$$\hat{e}_{fl} = \hat{e}_z \tag{F.10}$$
$$\hat{e}_{n1} = -\cos\gamma\left(\cos\phi \hat{e}_x + \sin\phi \hat{e}_y\right) + \sin\gamma \hat{e}_z$$
$$\hat{e}_{n2} = \cos\theta \hat{e}_x + \sin\theta \hat{e}_y$$

Normal-azimuthal correlation $\left(R_{n\theta}\right)$:

$$\begin{aligned}
\hat{e}_s &= \frac{(\eta_2\cos\theta-\eta_1\cos\phi)\hat{e}_x+(\eta_2\sin\theta-\eta_1\sin\phi)\hat{e}_y+(z_2-z_1)\hat{e}_z}{\sqrt{\eta_1^2+\eta_2^2-2\eta_1\eta_2\cos(\theta-\phi)+(z_2-z_1)^2}}\\
\hat{e}_{fl} &= \hat{e}_z\\
\hat{e}_{n1} &= -\cos\gamma\left(\cos\phi\hat{e}_x+\sin\phi\hat{e}_y\right)+\sin\gamma\hat{e}_z\\
\hat{e}_{n2} &= \sin\theta\hat{e}_x-\cos\theta\hat{e}_y
\end{aligned} \tag{F.11}$$

Radial-azimuthal correlation $\left(R_{u\theta}\right)$:

$$\begin{aligned}
\hat{e}_s &= \frac{(\eta_2\cos\theta-\eta_1\cos\phi)\hat{e}_x+(\eta_2\sin\theta-\eta_1\sin\phi)\hat{e}_y+(z_2-z_1)\hat{e}_z}{\sqrt{\eta_1^2+\eta_2^2-2\eta_1\eta_2\cos(\theta-\phi)+(z_2-z_1)^2}}\\
\hat{e}_{fl} &= \hat{e}_z\\
\hat{e}_{n1} &= \cos\phi\hat{e}_x+\sin\phi\hat{e}_y\\
\hat{e}_{n2} &= \sin\theta\hat{e}_x-\cos\theta\hat{e}_y
\end{aligned} \tag{F.12}$$

Radial-radial correlation $\left(R_{uu}\right)$:

$$\begin{aligned}
\hat{e}_s &= \frac{(\eta_2\cos\theta-\eta_1\cos\phi)\hat{e}_x+(\eta_2\sin\theta-\eta_1\sin\phi)\hat{e}_y+(z_2-z_1)\hat{e}_z}{\sqrt{\eta_1^2+\eta_2^2-2\eta_1\eta_2\cos(\theta-\phi)+(z_2-z_1)^2}}\\
\hat{e}_{fl} &= \hat{e}_z\\
\hat{e}_{n1} &= \cos\phi\hat{e}_x+\sin\phi\hat{e}_y\\
\hat{e}_{n2} &= \cos\theta\hat{e}_x+\sin\theta\hat{e}_y
\end{aligned} \tag{F.13}$$

References

[1] S. Candel, "Combustion dynamics and control: Progress and challenges", Proceedings of the Combustion Institute 29 (1) (2002) 1-28.

[2] T. Lieuwen, "Modeling Premixed Combustion-Acoustic Wave Interactions: A Review", Journal of Propulsion and Power 19 (5) (2003) 765-781.

[3] T. C. Lieuwen and V. Yang, Combustion instabilities in gas turbine engines(operational experience, fundamental mechanisms and modeling), American Institute of Aeronautics and Astronautics, Reston, VA,

[4] Santosh, Preetham and T. C. Lieuwen, "Response of turbulent premixed flames to harmonic acoustic forcing", Proceedings of the Combustion Institute 31 (1) (2007) 1427-1434.

[5] N. Peters, Turbulent Combustion, Cambridge University Press, Cambridge, UK, 2000.

[6] T. Poinsot and D. Veynante, Theoretical and numerical combustion, RT Edwards, Inc., 2005.

[7] R. Borghi,"Structure and Morphology of Premixed Flames", in *Recent advances in the Aerospace Sciences*, Plenum Press, New York, 1985

[8] C. K. Law and C. J. Sung, "Structure, aerodynamics, and geometry of premixed flamelets", Progress in Energy and Combustion Science 26 (4-6) (2000) 459-505.

[9] M. Oberlack, H. Wenzel and N. Peters, "On symmetries and averaging of the G-equation for premixed combustion", Combustion Theory and Modeling 5 (3) (2001) 363-383.

[10] G. Damkohler, "The effect of turbulence on the flame velocity in gas mixtures", Zeitschrift Electrochem 46 (1940) 601-626.

[11] A. N. Lipatnikov and J. Chomiak, "Turbulent flame speed and thickness: phenomenology, evaluation, and application in multi-dimensional simulations", Progress in Energy and Combustion Science 28 (1) (2002) 1-74.

[12] J. F. Driscoll, "Turbulent premixed combustion: Flamelet structure and its effect on turbulent burning velocities", Progress in Energy and Combustion Science 34 (2008) 91-134.

[13] A. Trouve and T. Poinsot, "The evolution equation for the flame surface density in turbulent premixed combustion", Journal of Fluid Mechanics 278 (1994) 1–31.

[14] K. N. C. Bray and R. S. Cant, "Some Applications of Kolmogorov's Turbulence Research in the Field of Combustion", Proceedings of the Royal Society of London 434 (1991) 217-227.

[15] V. L. Zimont, "Gas premixed combustion at high turbulence. Turbulent flame closure combustion model", Experimental Thermal and Fluid Science 21 (1-3) (2000) 179-186.

[16] H. Pitsch and L. D. D. Lagneste, "Large Eddy Simulation of Premixed Turbulent Combustion using a level-set approach", Proceeding of the Combustion Institute 29 (2002) 2001-2008.

[17] H. Pitsch, "A consistent level set formulation for large-eddy simulation of premixed turbulent combustion", Combustion and Flame 143 (2005) 587-598.

[18] E. Knudsen and H. Pitsch, "A dynamic model for the turbulent burning velocity for large eddy simulation of premixed combustion", Combustion and Flame 154 (4) (2008) 740-760.

[19] I. G. Shepherd and R. K. Cheng, "The burning rate of premixed flames in moderate and intense turbulence", Combustion and Flame 127 (3) (2001) 2066-2075.

[20] C. J. Lawn and R. W. Schefer, "Scaling of premixed turbulent flames in the corrugated regime", Combustion and Flame 146 (2006) 180-199.

[21] L. Boyer and J. Quinard, "On the dynamics of anchored flames", Combustion and Flame 82 (1) (1990) 51-65.

[22] A. P. Dowling, "A kinematic model of a ducted flame", Journal of Fluid Mechanics 394 (1999) 51-72.

[23] K. R. Mcmanus, T. Poinsot and S. M. Candel, "A review of active control of combustion instabilities", Progress in Energy and Combustion Science 19 (1) (1993) 1-29.

[24] S. Ducruix, T. Schuller, D. Durox and S. Candel, "Combustion Dynamics and Instabilities: Elementary Coupling and Driving Mechanisms", Journal of Propulsion and Power 19 (5) (2003) 722-734.

[25] A. C. Mcintosh, "Pressure disturbances of different length scales interacting with conventional flames", Combustion Science and Technology 75 (4-6) (1991) 287-309.

[26] M. Fleifil, A. M. Annaswamy, Z. A. Ghoneim and A. F. Ghoniem, "Response of a laminar premixed flame to flow oscillations: A kinematic model and thermoacoustic instability results", Combustion and Flame 106 (4) (1996) 487-510.

[27] J. A. Sethian, "Curvature and the evolution of fronts", Communications in Mathematical Physics 101 (4) (1985) 487-499.

[28] S. Ducruix, D. Durox and S. Candel, "Theoretical and Experimental Determinations of the Transfer Function of a Laminar Premixed Flame", Proceeding of the Combustion Institute 28 (1) (2000) 765-774.

[29] T. Schuller, D. Durox and S. Candel, "A unified model for the prediction of laminar flame transfer functions comparisons between conical and V-flame dynamics", Combustion and Flame 134 (1-2) (2003) 21-34.

[30] Preetham, Santosh H. and T. C. Lieuwen, "Dynamics of Laminar Premixed Flames Forced by Harmonic Velocity Disturbances", Journal of Propulsion and Power 24 (6) (2008) 1390-1402.

[31] A. N. Lipatnikov and P. Sathiah, "Effects of turbulent flame development on thermoacoustic oscillations", Combustion and Flame 142 (1-2) (2005) 130-139.

[32] P. Sathiah and A. N. Lipatnikov, "Effects of Turbulent Flame Speed Development and axial convective waves on oscillations of a long ducted flame", Combustion Science and Technology 179 (7) (2007) 1433-1449.

[33] D. You, Y. Huang and V. Yang, "A Generalized Model of Acoustic Response of Turbulent Premixed Flame and Its Application to Gas-Turbine Combustion Instability Analysis", Combustion Science and Technology 177 (5-6) (2005) 1109-1150.

[34] G. H. Markstein, Nonsteady flame propagation, Pergamon, 1964.

[35] S. Ducruix, T. Schuller, D. Durox and S. Candel,"Combustion Instability Mechanisms in Premixed Combustors", in *Combustion Instabilities in Gas Turbine Engines: Operational Experience, Fundamental Mechanisms and Modeling*, AIAA, Reston, VA, 2005

[36] V. Bychkov, "Analytical scalings for flame interaction with sound waves", Physics of Fluids 11 (1999) 3168.

[37] M. Sussman, P. Smereka and S. Osher, "A level set approach for computing solutions to incompressible two-phase flow", Journal of Computational Physics 114 (1) (1994) 146-159.

[38] T. F. Dupont and Y. Liu, "Back and forth error compensation and correction methods for semi-Lagrangian schemes with application to level set interface computations", Mathematics of Computation 76 (258) (2007) 647.

[39] Giovanni Russo and P. Smereka, "A remark on computing distance functions", Journal of Computational Physics 163 (2000) 51-67.

[40] M. Sussman and E. Fatemi, "An efficient, interface-preserving level set redistancing algorithm and its application to interfacial incompressible fluid flow", SIAM Journal on Scientific Computing 20 (4) (1999) 1165-1191.

[41] D. Peng, B. Merriman, S. Osher, H. Zhao and M. Kang, "A PDE-based fast local level set method", Journal of Computational Physics 155 (2) (1999) 410-438.

[42] S. B. Pope, Turbulent flows, Cambridge university press, 2000.

[43] J. O. Hinze, " Turbulence; an introduction to its mechanism and theory", New York, McGraw-Hill, 1959. (1959)

[44] R. C. Aldredge and F. A. Williams, "Influence of wrinkled premixed-flame dynamics on large-scale, low-intensity turbulent flow", Journal of Fluid Mechanics 228 (1991) 487-511.

[45] P. Smereka, "The numerical approximation of a delta function with application to level set methods", Journal of Computational Physics 211 (1) (2006) 77-90.

[46] R. C. Aldredge, "The speed of isothermal-front propagation in isotropic, weakly turbulent flows", Combustion Science and Technology 178 (7-9) (2006) 1201-1216.

[47] I. S. Gradshteyn and I. M. Rhyzik, Table of hltegrals, Series, and Products, Academic Press, New York, 1965.

[48] S. Shanbhogue, D. H. Shin, S. Hemchandra, D. Plaks and T. Lieuwen, "Flame sheet dynamics of bluff-body stabilized flames during longitudinal acoustic forcing", Proceedings of the Combustion Institute 32 (2) (2009) 1787-1794.

[49] A. G. Prudnikov, "Flame Turbulence", Seventh Symposium (International) on Combustion (1959)

[50] H. Kobayashi, "Experimental study of high-pressure turbulent premixed flames", Experimental Thermal and Fluid Science 26 (2-4) (2002) 375-387.

[51] D. Bradley, "How fast can we burn", Proceedings of the Combustion Institute 24 (1992) 247-262.

[52] K. N. C. Bray, "Studies of the turbulent burning velocity", Proceedings of the Royal Society of London. Series A, Mathematical and Physical Sciences (1990) 315-335.

[53] Yung-Cheng Chen, Munki Kim, Jeongjae Han, Sangwook Yun and Y. Yoon, "Measurements of the heat release rate integral in turbulent premixed stagnation flames with particle image velocimetry", Combustion and Flame 154 (2008) 434-447.

[54] P. Clavin and F. A. Williams, "Theory of premixed-flame propagation in large-scale turbulence", Journal of Fluid Mechanics 90 (03) (1979) 589-604.

[55] F. E. Marble and J. E. Broadwell, "The coherent flame model of non-premixed turbulent combustion", Project Squid TRW-9-PU, Project Squid Headquarters, Chaffee Hall, Purdue University (1977)

[56] H. Wenzel and N. Peters, "Direct numerical simulation and modeling of kinematic restoration, dissipation and gas expansion effects of premixed flames in homogeneous turbulence", Combustion Science and Technology 158 (2000) 273-297.

[57] H. Wenzel and N. Peters, "Scaling of production, kinematic restoration, and dissipation of the mean flame surface area", Combustion Science and Technology 177 (5-6) (2005) 1095-1107.

[58] S. J. Shanbhogue, D. V. Plaks and T. Lieuwen, The KH Instability of Reacting, Acoustically Excited Bluff-Body Shear Layers, 43 rd AIAA/ASME/SAE/ASEE Joint Propulsion Conference, 2007, AIAA #2007-5680.

[59] D. Durox, T. Schuller and S. Candel, "Combustion dynamics of inverted conical flames", Proceedings of the Combustion Institute 30 (2) (2005) 1717-1724.

[60] W. Polifke and C. Lawn, "On the low-frequency limit of flame transfer functions", Combustion and Flame 151 (3) (2007) 437-451.

[61] G. J. Bloxsidge, A. P. Dowling and P. J. Langhorne, "Reheat buzz: an acoustically coupled combustion instability. Part 2. Theory", Journal of Fluid Mechanics 193 (1988) 445-473.